Universidad de Oviedo

Departamento de Física

PROCESOS DE IMANACIÓN EN ARREGLOS DE NANOHILOS BASADOS EN METALES DE TRANSICIÓN.

MAGNETIZATION PROCESSES IN TRANSITION METAL BASED NANOWIRE ARRAYS.

TESIS DOCTORAL

Javier García Fernández

Directores

Prof. Dr. Blanca Hernándo Grande

Dr. Víctor Manuel de la Prida Pidal

Programa de Doctorado de Física Fundamental y Aplicada

2014

A mis abuelos, Eloína y Kuki…

TABLE OF CONTENTS

Agradecimientos **7**

List of Abbreviations **9**

Summary **11**

Resumen **13**

1. Introduction **15**

1.1. Nanotechnology and nanostructures *15*

1.2. Magnetic nanowires in porous anodic alumina templates (PAAM) *16*

1.3. Magnetism and magnetic characterization based on hysteresis loops *17*

1.3.1. Magnetism and magnetic materials 17

1.3.2. Magnetic anisotropy 19

1.3.3. Magnetic characterization based on magnetic hysteresis loops 21

2. Técnicas de caracterización morfológica, estructural y magnética **25**

2.1. Microscopía electrónica de barrido (SEM) *25*

2.2. Microscopio electrónico de transmisión (TEM) *26*

2.3. Difracción de rayos-X (XRD) *28*

2.4. Magnetometría de Muestra Vibrante (VSM) *29*

3. Métodos de fabricación **31**

3.1. Anodización del aluminio *31*

3.2. Fabricación de las membranas de alúmina anódica nanoporosa *34*

3.3. Sistema experimental de anodización electroquímica *36*

3.4. Características geométricas de la capa porosa de alúmina *37*

3.5. Procesos de anodización dura *39*

3.6. Obtención de las membranas de alúmina nanoporosa *40*

3.7. Electrodeposición utilizando membranas nanoporosas de alúmina anódica como plantillas *42*

3.8. Técnicas de crecimiento por deposición de capas atómicas *47*

4. Analysis of Magnetization Processes in Nanomaterials by First Order Reversal Curves **49**

4.1 Preisach Model of Hysteresis *49*

4.2 First Order Reversal Curves *52*

4.3. FORC Simulation from a Statistical Approach *53*

4.3.1. Independent switching fields 53

4.3.2. Magnetostatic interactions among nanowires in the array 57

4.3.3. Reversible magnetization processes in FORC analysis 60

4.3.4. Non homogeneous ISFD 63

4.4 Exchange coupling between ferromagnetic phases *69*

4.5. Summary and Conclusions *76*

5. Multi-segmented Co_xNi_{1-x} Nanowire Arrays **79**

5.1. Experimental Procedure: Synthesis of Co-Ni multi-segmented nanowires *80*

5.2. Morphological and crystallographic characterization *82*

5.3. Magnetic characterization *87*

5.4. Summary and Conclusions *95*

6. Nanowires arrays of Co-Cu solid solutions **99**

6.1. Fabrication and morphological characterization of Co-Cu nanowire arrays *100*

6.2 Structural analysis of Co-Cu electrodeposited nanowires *102*

6.3 Effect of Cu content on the magnetic properties of Co-Cu nanowires arrays *106*

6.3.1. Room temperature DC magnetization & its angular dependence 106

6.3.2 Magnetic characterization based on FORC 111

6.3.3. Temperature influence on the magnetic anisotropy 113

6.4. Summary and Conclusions *116*

7. Magnetic nanowires embedded in cylindrical porous alumina templates. **119**

7.1. Fabrication of the CPAAM templates *120*

7.2. Magnetic nanowires electrodeposition *121*

7.3. Magnetic properties of CPAAM nanowire arrays: comparison with planar nanowire arrays. *123*

7.4. Summary and Conclusions *130*

8. General conclusions and further works **133**

9. Conclusiones y futuros trabajos **137**

References **141**

List of publications **147**

AGRADECIMIENTOS

En primer lugar me gustaría resaltar y agradecer la labor de mis directores de tesis Prof. Dr. Blanca Hernando Grande y Dr. Víctor Manuel de la Prida Pidal, habiéndome ayudado en todo lo que necesitase más allá de sus deberes u obligaciones. Así mismo, me gustaría agradecer a mis compañeros Dr. Victor Vega Martínez y Lorena González Legarreta por los buenos momentos en el laboratorio y las extensas discusiones científicas de las cuales han surgido buenas ideas como fruto del trabajo en equipo. Son muchas las personas con las que he coincidido en el grupo de la Universidad de Oviedo, desde mis comienzos con Tatiana Sánchez y el Dr. Pablo Álvarez hasta la más reciente Lucía Iglesias, pasando por los *postdocs* Dr. Wagner de Oliveira, Dr. David Serantes y Dr. Rafael Caballero, de los cuales no sólo he aprendido en el ámbito profesional sino que he tenido el placer de entablar una gran amistad.

Quiero expresar mi especial agradecimiento al Prof. Dr. Manuel Vázquez Villalabeitia por darme la oportunidad de realizar una estancia en su grupo de investigación Nanomagnetismo y Procesos de Magnetización. Guardo gratos recuerdos de todas las personas que forman dicho grupo, Dr. Agustina Asenjo, Dr Rafael Pérez, Dr. Laura González, Dr. Christina Bran, Dr Mariana Proença, Sonia Rodríguez, Oscar Iglesias, Alejandro Jiménez, David González y un largo etcétera. Reitero mi más profunda gratitud a todas las personas que componen este grupo ya que han hecho que recuerde dicha estancia como uno de los mejores momentos.

I would like to acknowledge Prof. Dr. Kornelius Nielsch for giving me the opportunity to visit his group "Multifunctional Nanostructures" at the University of Hamburg. I would like to mention Dr. Detlef Görlitz, Dr. Josep M. Montero Moreno, Dr. Robert Zierold, Svenja Bäßler, Tim Böhnert, Vincent Linseis, Ann-Kathrin Michel, Martin Waleczek, Lewis Akinsinde and the rest of people who form part of the group. I have learned from all of them and they made me to feel Hamburg like home.

También he de agradecer al programa de becas "Severo Ochoa" y la FICyT por la financiación y sobre todo por ofrecerme la posibilidad de realizar estancias de investigación en los centros mencionados anteriormente.

Finalmente, me gustaría agradecer la paciencia de mi mujer Enerina Pucci, la cual se ha vuelto una experta en nanohilos y análisis FORC y también agradecer a mis padres Francisco Javier y Blanca Esther así como a mi hermana Laura y el resto de mi familia por el apoyo que siempre me han dado.

LIST OF ABBREVIATIONS

AFD: Anisotropy Field Distribution

ALD: Atomic Layer Deposition

CGD: Cumulative Gaussian Distribution

CPAAM: Cylindrical Porous Anodic Alumina Membrane

D_P: Pore Diameter

D_{int}: Interpore Distance

EDX/EDS: Energy Dispersive X-ray Spectroscopy

FORC: First Order Reversal Curves

HAADF: High-Angle Annular Dark-Field

HA-PAAM: Hard Anodized-Porous Anodic Alumina Membranes

HL: Hysteresis Loop

ISFD: Intrinsic Switching Field Distribution

MFI: Mean Field Interaction

PAAM: Porous Anodic Alumina Membrane

SAED: Selected Area Electron Diffraction

SCTs: Servicios Científico Técnicos (Scientific Technical Services)

SEM: Scanning Electron Microscope

SFD: Switching Field Distribution

STEM: Scanning Transmission Electron Microscope

TEM: Transmission Electron Microscope

VSM: Vibrating Sample Magnetometer

XRD: X-Ray Diffraction

SUMMARY

This PhD thesis focuses on the study of magnetization reversal processes and different magnetic contributions that play a key role in the magnetic behavior of nanowire arrays fabricated by means of electrodeposition into porous anodic alumina membranes (PAAMs). This work covers the fabrication and morphological, structural and magnetic characterization of these nanostructures.

First of all, different electrochemical techniques employed to fabricate the PAAM templates as well as the subsequent electrodeposition of magnetic nanowires are explained in detail in order to provide a deep insight of the different characteristics for all fabricated nanomaterials.

This work is also focused on the First Order Reversal Curves (FORC) analysis. This method is an excellent tool to investigate the different magnetization processes that take place during the magnetization reversal in nanowire arrays. Such tool allows obtaining intrinsic magnetic behaviors of single nanowires, and magnetic interactions among them in the array provided by macroscopic measurements employing conventional magnetometry. In this work, the FORC analysis is explained in detail and new features and real meaning of the experimental results are investigated. Moreover, in order to corroborate the experimental measurements, a computational program based on a statistical approach has been performed.

The abovementioned studies on FORC have been employed in different experimental systems. First, bi-segmented nanowire arrays composed by a long segment of Ni followed by another Co segment have been fabricated and magnetically characterized. Interesting phenomena appear at the interface between both segments being exchange coupled in each nanowire.

The next step has been devoted to the study of multi-segmented Co-Ni nanowire arrays by controlling the different alloy composition in each segment. Then, the composition variation and thus each segment can be correlated with different crystalline structures that modify the magnetic properties of each segment. In order to elucidate the

magnetic contribution of each segment, several nanowire arrays with different stacks have been electroplated and characterized by scanning and transmission electron microscopies, X-ray diffraction and studied by performing FORC analysis.

Another material presenting different magnetic behavior and structural phases is the Co-Cu system, since these elements are poorly miscible. Co-Cu nanowire arrays with different compositions have been fabricated. For a low Cu content around 8at.% two different ferromagnetic behaviors have been simultaneously observed. In addition, the corresponding fractions related to such behaviors are deduced to be interacting between them from both FORC analysis and the temperature dependence of coercivity and remanence.

Finally, cylindrical porous anodic alumina membranes (CPAAM) have been employed to fabricate nanowire arrays, with different alloys based on metal transition elements, of cylindrical symmetry. The effect of the array cylindrical symmetry to the magnetic measurements have been discussed and compared with planar nanowire arrays fabricated under the same conditions. Furthermore, both experimental and simulated FORC analyses on these samples have been also performed.

RESUMEN

Esta tesis doctoral se centra en el estudio de los procesos de inversión de la magnetización y diferentes contribuciones magnéticas que juegan un papel clave en el comportamiento magnético de las matrices de nanohilos fabricados mediante electrodeposición en las membranas de alúmina anódica porosa (PAAMS). Este trabajo comprende tanto la fabricación como la caracterización morfológica, estructural y magnética de estas nanoestructuras.

En primer lugar, las diferentes técnicas electroquímicas empleadas para fabricar las plantillas PAAM así como la posterior electrodeposición de nanohilos magnéticos, son estudiados en detalle con el fin de proporcionar una comprensión profunda de las diferentes características de los nanomateriales fabricados .

Este trabajo también se centra en el análisis de las curvas de inversión de primer orden (*First Order Reversal Curves*, FORC). Este método es una excelente herramienta para investigar los diferentes procesos de imanación que tienen lugar durante la inversión de la imanación de os arreglos de nanohilos. Dicha herramienta permite discernir comportamientos magnéticos intrínsecos de nanohilos individuales y las interacciones entre los nanohilos en la matriz, a partir de medidas macroscópicas empleando magnetometría convencional. En este trabajo, se realiza una revisión detallada del análisis FORC y se investigan nuevos tipos de distribuciones FORC discutiendo el significado real de los mismos. Con el fin de corroborar las mediciones experimentales, se ha realizado un programa computacional basado en un enfoque estadístico.

Los estudios anteriormente mencionados sobre FORC se han empleado en diferentes sistemas experimentales. En primer lugar, matrices de nanohilos bi-segmentados compuestas por un segmento largo de Ni seguido de otro segmento largo de Co se han fabricado y caracterizado magnéticamente. Se han encontrado a su vez fenómenos interesantes en la interfaz entre los dos segmentos de cada nanohilo, donde dichos segmentos están acoplados por canje magnético.

El siguiente paso ha sido el estudio de matrices de nanohilos multi-segmentados de aleaciones de Co-Ni donde cada segmento corresponde a una composición diferente de dicha aleación. Cada composición y por lo tanto cada segmento se pueden correlacionar con distinta estructura cristalina, modificando así las propiedades magnéticas de cada uno de los segmentos. Con el fin de dilucidar la contribución magnética de cada segmento, distintas matrices de nanohilos, variando el tipo de apilamiento han sido fabricados y estudiados por microscopía electrónica de barrido y transmisión, difracción de rayos X y análisis FORC.

Otro material que puede presentar diferentes fases magnéticas es el sistema de Co-Cu, ya estos elementos son pobremente miscibles. En este trabajo, se han fabricado arreglos de nanohilos de Co-Cu con diferentes composiciones. Para pequeñas cantidades

de Cu, en torno al 8 at.%, se ha encontrado coexistencia de dos comportamientos ferromagnéticos distintos. Además, se ha deducido, a partir del análisis FORC y la dependencia con la temperatura de la coercitividad y remanencia, que las diferentes fracciones del material relacionadas con sendos comportamientos, se encuentran interactuando entre ellas.

Finalmente, membranas cilíndricas de alúmina anódica porosa (CPAAM) se han empleado para fabricar arreglos de nanohilos, de diferentes aleaciones basadas en elementos de transición, con geometría cilíndrica. El efecto de la simetría cilíndrica de la matriz en las medidas magnéticas ha sido estudiado y comparado con arreglos planos de nanohilos fabricados bajo las mismas condiciones. Por otra parte, análisis FORC tanto experimental como simulado ha sido realizado en estas muestras.

1. INTRODUCTION

1.1. NANOTECHNOLOGY AND NANOSTRUCTURES

Over the last years the nanotechnology has been attracted more and more interest within the scientific community. Special attention has been paid in the miniaturization of technological devices improving their capabilities and operation ranges. However, such a reduction of conventional devices and the development of new nanomaterials have required the intensively study of matter from the fundamental point of view when it is treated at the nanometric scale. Moreover, the reduction of the size at such low sizes becomes in the emergence of new physical phenomena that leads to the development of new functional materials and the better understanding of nature at nanometric scale. The applicability of nanotechnology has been widely exploited in fields as electronics, where the reduction of the size increases the number of elements that can form a circuit, and in biomedicine, since the nanometric scale allows the direct interaction with cells. The nanoscience has been accompanied by a revolution of fabrication and characterization techniques that have promoted the technological evolution and the interest in such part of the science.

There are several techniques of nanomaterials fabrication, however, those techniques can be enclosed in two main groups, "Top-Down" and "Bottom-Up". The first group corresponds with those techniques that are based in the reduction of the size of macroscopic materials by means of different processes as patterning, etching and deposition. The most representative example of this group is the electron or ion beam lithography, among others [Martín 2003].

"Bottom-Up" techniques are based on the self-assembly of atoms or molecules resulting in more complex nanometric structures. Although there is a limitation in the geometry of the nanomaterials fabricated by these methods, such techniques have been extensively studied due to their low-costs and their potential applicability in the industry. As an example of "Bottom-Up", sol-gel and electrochemistry techniques can be found. However, "Top-Down" and "Bottom-Up" techniques are not necessarily incompatibles. The complementation of both techniques allows producing more complex and functional materials [Sanz 2007].

1.2. MAGNETIC NANOWIRES IN POROUS ANODIC ALUMINA TEMPLATES (PAAM)

The anodization of aluminum to growth a porous Al_2O_3 layer has been extensively study due to its interesting properties for a vast number of applications [Eftekhari 2008, Lupu 2010, Nalwa 2011]. However, the investigation of Masuda and Fukuda [Masuda 1995], represented an inflection point since their discovery of the double step anodization process, which resulted in an ordered honeycomb nanoporous array. Further studies also reflected that depending on the electrochemical parameters, the geometrical characteristics of the PAAMs as pore diameter, distance between pores and pores length can be tuned [Knaack 2004, Wehrspohn 2000, Jeesensky 1998].

On one hand, the PAAM offer a wide range of applications by itself in biomedical devices as drugs delivery [Gong 2003, Kang 2007], sensors [Grimes 2000, Dickey 2002, Varghese 2003] and filtering devices [Romero 2012]. However, the application of the PAAM that has been used in this work is the fabrication of magnetic nanowires arrays by electrodeposition into the pores of the PAAMs [Nielsch 2000, Vázquez 2004]. Such nanowire arrays are interesting for high recording media applications and for the large scale and low cost nanowires fabrication by itself.

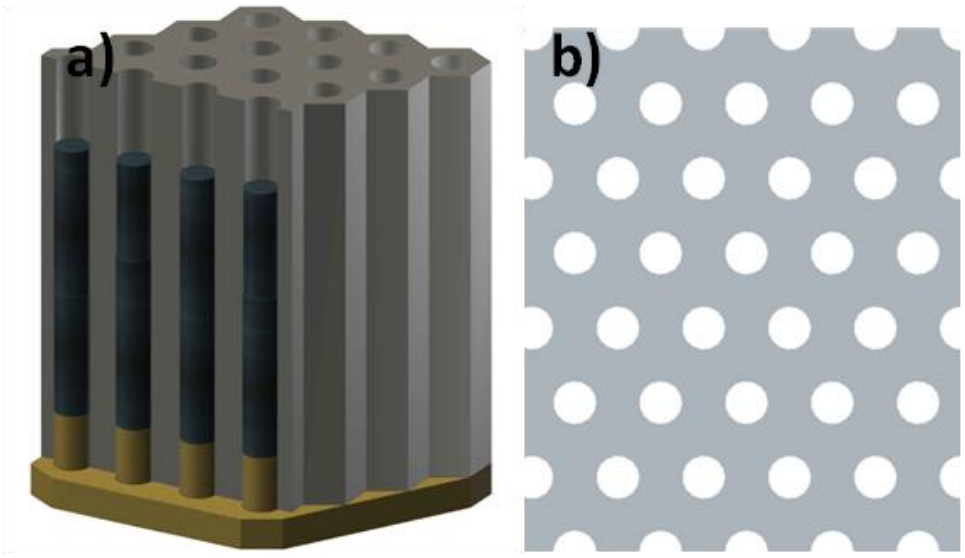

Figure 1.1*: a) Schematic draw of electrodeposited nanowires into the pores of a PAAM, at the bottom the nanocontacs of Au used as cathode are shown. b) Top view of the honeycomb arrangement of the pores in a PAAM.*

1.3. MAGNETISM AND MAGNETIC CHARACTERIZATION BASED ON HYSTERESIS LOOPS

In this section, a briefly introduction to those aspects in magnetism and magnetic materials related to this work, and in more detail, an introduction to the different ways to characterize them through their magnetization curves or hysteresis loops as a response to an applied magnetic field, will be performed.

1.3.1. MAGNETISM AND MAGNETIC MATERIALS

Previous to the description of any type of magnetic material, it is necessary to define what the magnetic moment (m) and thus the magnetization (M) mean. In principle, any physical characteristic of a material is coming from what constitutes it, i.e., atoms and interactions among them. In a classical point of view, each atom can be seen as an electrical circuit due to the motion of the electrons around the nucleus. Taking into account the Faraday-Lenz law, an electrical current generates a magnetic field so that each atom can be supposed as a small magnet, small enough to consider it as a magnetic dipole or magnetic moment (m). However, the physical phenomena in such low scales must be understood under the quantum mechanics. From this point of view, the magnetic moment can be associated with three atomic contributions, the spin of the electron (S), the orbital angular momentum (L) and the change in L due to an external applied magnetic field. The magnetization (M) of a magnetic material takes into account the contribution of all atomic magnetic moments. The different types of magnetic materials can be classified attending to their magnetization behavior as a function of an applied magnetic field (H). Magnetic susceptibility ($\chi = M/H$) relates the previous magnitudes directly as the change of the magnetization produced by a change of an applied magnetic field.

The first types of magnetic materials that are being introduced are those that present very weak magnetism. First of all, a diamagnetic material is constituted by atoms with no net magnetic moment. When a magnetic field is applied to the material, the orbital of the electrons are modified in such way to compensate the change of the magnetic flux following the Lenz's law, lying in a negative and small magnetic susceptibility. On the other hand, if the atoms present an inherent magnetic moment, the external magnetic field produces a torque in the magnetic moment tending to align it parallel with respect to the applied field. However, the thermal agitation prevents them

from completely alignment with the filed, reducing the effect of that field and showing magnetic susceptibility values slightly greater than 1.

Taking into account the Pauli's exclusion principle, two electrons cannot occupy the same quantum state at the same time, or in other words, it is impossible to have two electrons with the same four quantum numbers simultaneously. When atoms are close enough in a certain material, the electron wave functions of adjacent atoms may overlap producing an interaction between the orbitals of the electrons. When a given atom presents a certain direction of magnetization makes the energy of the second atom highly dependent on the direction of magnetization. Such influence among neighboring atoms is called exchange coupling. More precisely, when the exchange coupling is such that the parallel magnetization is the most stable configuration, the exchange is said to be ferromagnetic, whilst the anti-ferromagnetic exchange occurs when the magnetic moments tend to be coupled in an anti-parallel configuration. In ferromagnetic materials, the exchange energy is very large and causes adjacent moments to be aligned along the same direction which is traduced in large and positive magnetic susceptibility values. Even though with the exchange coupling and depending of the temperature of the material, the thermal energy can be larger than the exchange one provoking a magnetic phase transition from ferromagnetism to paramagnetism due to thermal agitation. The temperature at which the transition occurs is called Curie-Weiss temperature.

However, in the case of ferromagnetic materials, the exchange coupling would prohibit a demagnetized state, which contradicts what is observed in a macroscopic material. The demagnetized state is possible due to the formation of magnetic domains inside the material [Jiles 1998]. Such domains are regions where all the magnetic moments are aligned along the same direction. The demagnetized state is then accessible when magnetic moments of different domains lie along random directions in such a way that the overall macroscopic magnetization is suppressed. The transition between magnetic domains, where the magnetic moments have to gradually change their orientation, is called domain wall. When these magnetic materials are submitted to an external magnetic field, magnetic moments of different magnetic domains tend to align along the applied field direction through two different modes. First, those magnetic domains that are already aligned with the applied field increase their size through the propagation of domain walls. This is, in general, an irreversible process leading to the magnetic hysteresis phenomena. The domain wall motion is usually affected by the

existence of pinning centers, impurities or defects, slowing down the velocity of the domain wall motion and increasing the energy needed to produce the magnetization reversal.

1.3.2. MAGNETIC ANISOTROPY

Usually, the magnetic behavior of a given material depends on the applied magnetic field direction, or in other words, the material shows preferential orientations of magnetization [Cullity 1972, Chikazumi 1997]. There are several origins of magnetic anisotropies, being the magneto-crystalline and shape anisotropies the most relevant ones in this work.

Magneto-crystalline anisotropy

Depending on the spatial distribution of the atoms in a crystal, the spin-orbit interaction between them can be modified affecting the magnetic coupling. Magneto-crystalline anisotropy is then directly related with the symmetry of the crystal lattice. In cubic cells as fcc and bcc, as can be the case of Ni and Fe, respectively, the magnetic anisotropy energy can be expressed as:

$$E_{mc} = K_0 + K_1(cos^2\theta_1 cos^2\theta_2 + cos^2\theta_2 cos^2\theta_3 + cos^2\theta_3 cos^2\theta_1) + \cdots$$
$$\ldots + K_2(cos^2\theta_1 cos^2\theta_2 cos^2\theta_3) + \cdots \quad (1.1)$$

where K_0, K_1 and K_2 are the anisotropy constants and θ_1, θ_2 and θ_3 are the angles between the magnetization direction and the crystallographic axes. In contrast, for hexagonal close-packed (hcp) structures, one of the most stable crystalline structures of Co, the magneto-crystalline energy can be written in terms of the angle (θ) that forms the magnetization with the longitudinal axis (c-axis) of the crystalline cell:

$$E_{mc} = K_0 + K_1 sin^2\theta + K_3 sin^4\theta + \cdots \quad (1.2)$$

In both cases, K_0 can be neglected as not depends on the angle between the magnetization and the crystallographic axes. Depending on the values of the anisotropy constants and specially the sign, the magneto-crystalline energy is minimized for certain angles that implies that there are directions of preferential magnetization, called magnetization easy axes. The anisotropy constants for Fe, Co and Ni are collected in

Table 1.1, which result in the magnetization easy and hard axes shown in *Figure 1.2* for each crystalline structure.

Element	Crystalline structure	K_1 (10^5 erg·cm^{-3})	K_2 (10^5 erg·cm^{-3})
Fe	*Bcc*	4.8	±0.5
Co	*Hcp*	45	15
Ni	*Fcc*	-0.5	-0.2

***Table 1.1**: Anisotropy constants K1 and K2 at room temperature for Fe(bcc), Co(hcp) and Ni(fcc) [Cullity 1972].*

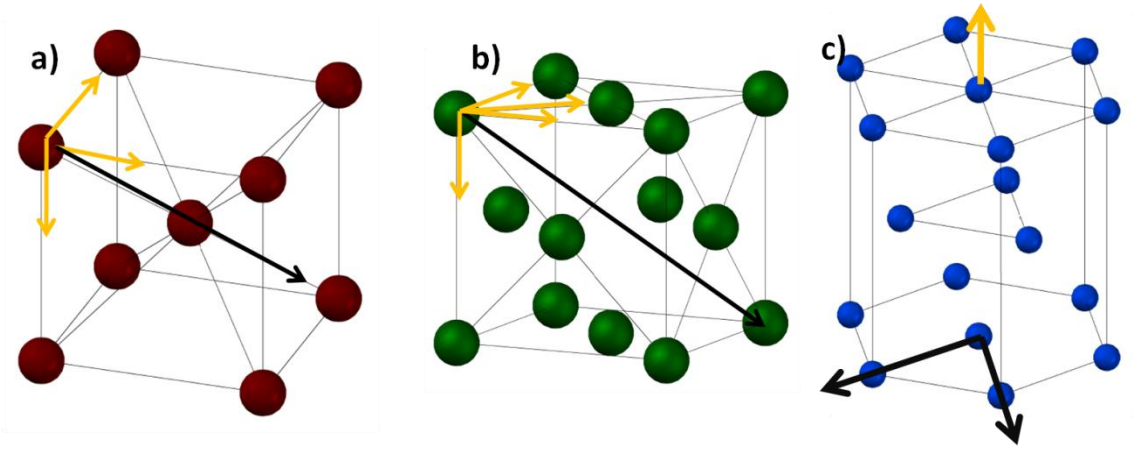

***Figure 1.2**: a) Body centered cubic (bcc), b) face centered cubic (fcc) and c) hexagonal close-packed (hcp) crystalline lattices. The magnetization easy (yellow) and hard (black) axes are shown for each case. (Adapted from [O'Handley 1999])*

Shape anisotropy

The external geometry and dimensions of the material play an important role in the effective magnetic anisotropy. When a material is uniformly magnetized, a superficial magnetic pole density arises in those surfaces that have a normal magnetization component. However, such quantity is slightly artificial due to it becomes as a consequence of the comparison between the dielectric theory formalism. Such magnetic poles distribution produces a magnetic field inside the material that has the opposite direction with respect to the applied magnetic field. The demagnetizing field is proportional to the magnetization through the tensor that depends on the geometry of the material. In the specific case of nanowires that concerns this work, the demagnetizing factor and thus the shape anisotropy energy can be calculated from the expression for a

prolate ellipsoid considering the semi-major axis infinite with respect to the semi-minor one [Encinas-Oropesa 2001, Dimitru 2005, Vega 2010]:

$$E_{sh} \cong \pi M_S^2 sin^2\theta \tag{1.3}$$

where θ is the angle formed by the magnetization and the semi-major axis. From equation (1.3) the preference magnetization direction lies along the semi-major axis of the nanowire since the shape anisotropy energy is minimize for $\theta = 0$.

1.3.3. MAGNETIC CHARACTERIZATION BASED ON MAGNETIC HYSTERESIS LOOPS

Magnetic hysteresis loop (HL) is the most distinctive figure of merit for many magnetic materials, where many physical phenomena are involved in its shape, giving valuable information related to the different magnetization processes that take place under the influence of an applied magnetic field. The magnetization curve depends strongly on the type of magnetic material that is being characterized. In a ferromagnetic material, which typically shows spontaneous magnetization due to the coupling among the magnetic moments, there are few quantities that can provide some preliminary information. Those parameters are remanent magnetization or remanence (Mr), coercive field (Hc) and hysteresis. Remanence is the value of magnetization when the applied magnetic field is set to zero after the enforcement of a non-zero magnetic field. The adimensional remanence normalized to the saturation magnetization has been employed in all the sections of this work. The coercive field (Hc) is the minimum magnetic field necessary to demagnetize de material after its magnetization saturation. However, when some part of the material reverses its magnetization through a domain wall propagation, the value of the magnetic field necessary to move such domain wall is called switching field (Hsw). Depending on the ferromagnetic material, the overall magnetization reversal process can be the result of the movement of several domain walls at different switching fields. Moreover, if the material reverses its magnetization through the propagation of a single domain wall, both switching and coercive fields coincide. Finally, the hysteresis that is the area enclosed in the HL gives an idea of the energy employed to perform the magnetization reversal and the irreversible processes that have taken place during the process as domain walls propagation. Different representations of some characteristics of

it are of special interest for making the complete information stored in such behavior more accessible to our knowledge. In the following section, several ways to present different behaviors concerning the shape of the HL will be discussed.

Switching Field Distribution (SFD) and hysteresis shape

An idea of different switching fields that can be present in the magnetization reversal process can be provided by the first derivative of the ascendant branch of the hysteresis loop. Furthermore, since the first derivation of HL represents the changes of the magnetization produced by the external magnetic field, it is also a measurement of the magnetic susceptibility of the different reversal magnetization processes. In fact, not only the real SFD but the reversible reversal magnetization processes, as well as magnetostatic interactions inside the material are also affecting the SFD plot.

SFD regions that can be correlated with magnetic hysteresis and reversible and irreversible components of the magnetization can be observed in the hysteresis shape plots of the HL. The procedure to extract such plots from the HL is schematized in *Figure 1.3* a) and b). Basically, it consists in the representation of the difference between the ascendant and descendant branch of the HL for each value of magnetization. This kind of figure can be of special interest in case of the presence of different ferromagnetic phases coexistence or process that may lie on small differences in the width of the hysteresis loop, as can be observed in *Figure 1.3* c) and d), where the case of two different ferromagnetic phases , magnetically softer and harder, is represented. Although the behavior of the hysteresis shape plots can be clearly distinguished in the HLs for the examples shown in *Figure 1.3*, in general, experimental HLs can show very smooth curves what difficult the observation of the hysteresis shape directly from the HL. This kind of representation will be extensively employed along this work.

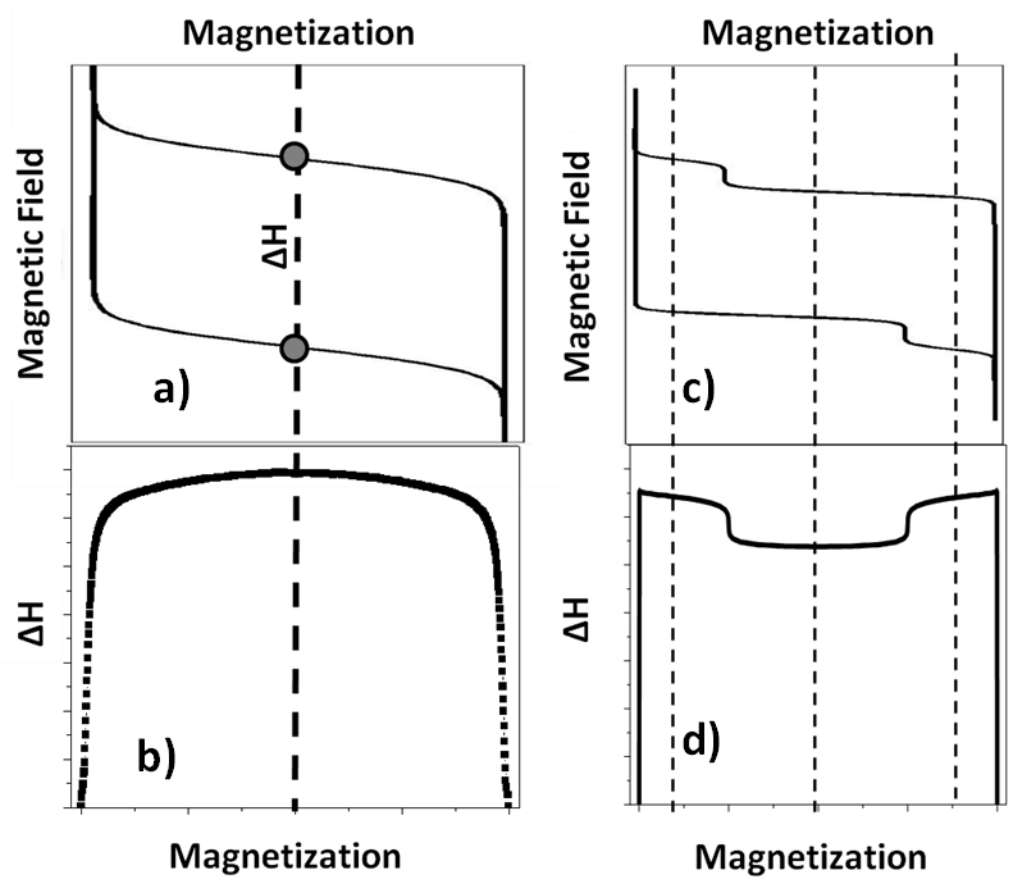

Figure 1.3*: a) Rotated hysteresis loop for the explanation of the hysteresis shape plot shown in b). c) and d) display the hysteresis loop and the hysteresis shape, respectively, for the case with two different ferromagnetic phases where the softer is the majority one.*

Anisotropy field distribution (AFD)

Another parameter of special interest is the effective anisotropy field or the field needed to saturate the magnetic material along the magnetization hard axis being related to the magnetic anisotropy. This field can be determined using ferromagnetic resonance (FMR) measurements [Encinas-Oropesa 2001], however the possibility to obtain the effective anisotropy field from the anisotropy field distribution (AFD) method has attracted much attention because it is based in standard magnetometry measurements [Barandiaran 1989, García-Arribas 1992, Bottoni 1997]. Such AFD is calculated from the second derivative on the descendant branch of the magnetic hysteresis loop along the magnetization hard axis as follows:

$$\sigma = -H\frac{d^2}{dH^2} < m(H) > \qquad (1.4)$$

An example of the AFD is shown in *Figure 1.4*. The most distinctive parameter is the mean anisotropy field $<H_A>$ that corresponds to the value at which the AFD takes its maximum. The relation of $<H_A>$ with the effective magnetic anisotropy will depend on the different origins of anisotropy as well as different factors as magnetostatic interactions, that can affect the magnetic properties of magnetic nanowire arrays studied in this work [De La Torre Medina 2009].

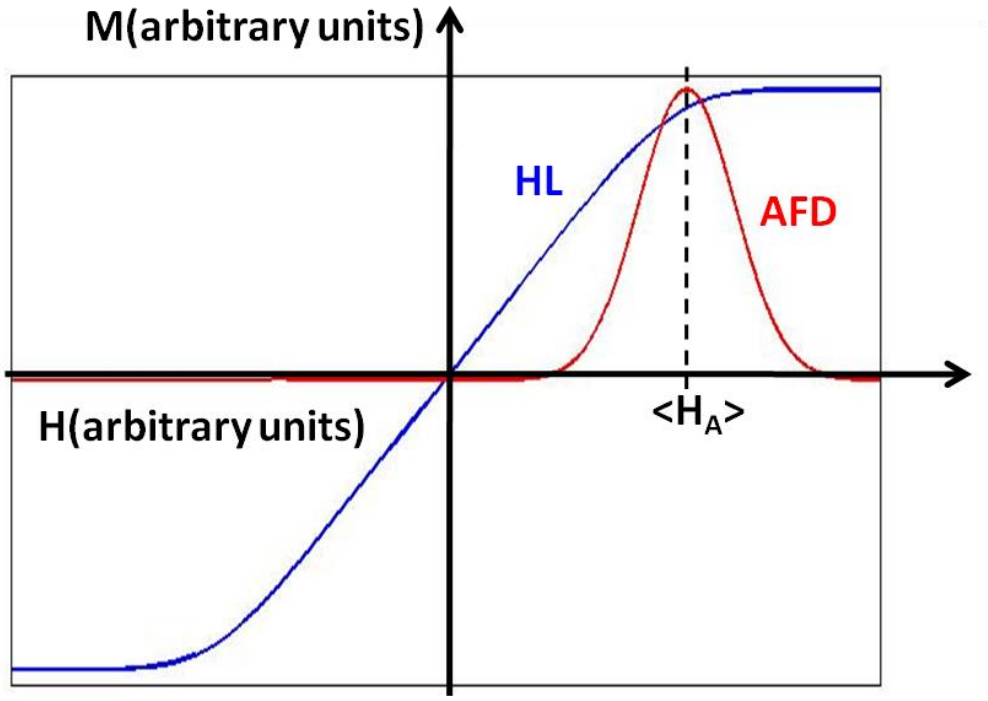

***Figure 1.4**: Anisotropy field distribution (red) as a result of HL (blue) data treatment through equation (1.4).*

2. TÉCNICAS DE CARACTERIZACIÓN MORFOLÓGICA, ESTRUCTURAL Y MAGNÉTICA

2.1. MICROSCOPÍA ELECTRÓNICA DE BARRIDO (*SEM)*

Este tipo de microscopía proporciona información morfológica y/o composicional a nivel de la superficie de un material. Para ello se utiliza un haz de electrones, dirigido y enfocado mediante condensadores y lentes electromagnéticas, que excita los átomos de, o cerca de, la superficie de dicho material. Existen tres excitaciones principales, que mediante el uso del detector apropiado proporcionan información complementaria. En primer lugar, la detección de los electrones secundarios (SE) producidos por interacción inelástica entre el haz de electrones incidente y los átomos del material, genera una imagen de gran resolución de la morfología del material. Por otro lado, en los átomos de la superficie también se producen interacciones elásticas entre estos y el haz de electrones incidentes. Los electrones detectados como consecuencia del choque elástico se denominan electrones retro-dispersados. Debido a la naturaleza de dicha interacción, la cantidad de electrones que son retro-dispersados depende fuertemente del número atómico Z, por lo que la detección de estos electrones proporciona una imagen morfológica con contraste composicional, aunque con menor resolución que el caso anterior. Por último, la mayoría de los sistemas o dispositivos de SEM actuales también están equipados con un detector de rayos-X, que acoplado a un sistema de microanálisis constituye una técnica espectroscópica (EDX) que proporciona información composicional de la muestra con una penetración de detección del orden de varias micras de profundidad. Debido a esto último, esta técnica sólo proporciona información cuantitativa en muestras suficientemente homogéneas.

El esquema básico de un SEM se muestra en la *Figura 2.1*. En primer lugar, el haz de electrones es emitido por un filamento incandescente, compuesto de Tungsteno en muchos de los casos, que constituye el cañón de electrones. A continuación el haz atraviesa un sistema de lentes electromagnéticas que lo confinan y enfocan para, por

último, atravesar un sistema de condensadores que son los que permiten realizar el barrido superficial de la muestra.

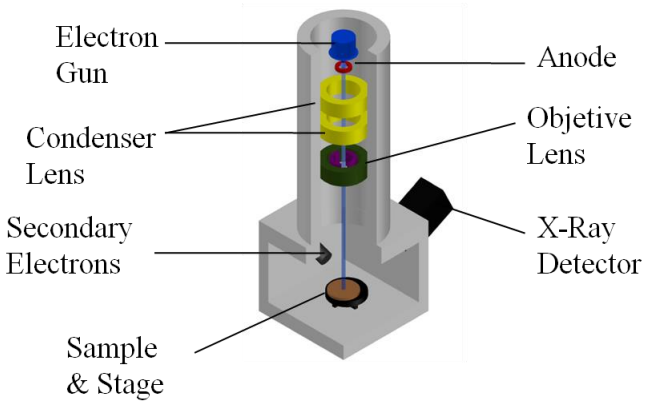

***Figura 2.1**: Esquema de un Microscopio Electrónico de Barrido.*

Teniendo en cuenta que la sonda es un haz de partículas cargadas, se necesita que la muestra sea conductora eléctrica para que no se produzcan efectos de carga que puedan desviar los electrones incidentes, distorsionando la imagen. En el caso de materiales aislantes eléctricos se recurre a una metalización previa de unos 15nm de espesor con un material de elevada conductividad eléctrica. Estos recubrimientos suelen realizarse empleando Au, Cr, Pd, Pt, etc., que además al poseer elevado número atómico Z, mejora la relación señal/ruido al aumentar el número de electrones secundarios emitidos.

Para la caracterización de las muestras estudiadas en este trabajo se han utilizado varios modelos comerciales de SEM, JEOL 6610LV (Servicios Científico-Técnicos de la Universidad de Oviedo, SCTs), Philips XL3O (Instituto de Ciencia de Materiales de Madrid, CSIC), ZEISS EVO 50 y ZEISS SIGMA (Instituto de Física Aplicada de la Universidad de Hamburgo). Algunos de ellos son una variante del SEM convencional llamado SEM de emisión de campo FE-SEM. La única diferencia entre el FE-SEM y el SEM es la forma de generar el haz de electrones ya que el FE-SEM genera haces de electrones de alta y baja energía muy focalizados, mejorando así la resolución y permite trabajar a potenciales reducidos del haz de electrones, lo que ayuda a minimizar el efecto de carga en especímenes no conductores.

2.2. MICROSCOPIO ELECTRÓNICO DE TRANSMISIÓN (*TEM*)

La principal diferencia entre los microscopios TEM y SEM, reside en que en el caso del TEM el haz de electrones atraviesa el material para luego ser colectado en una

pantalla fluorescente o placa fotográfica. El esquema básico de un TEM se muestra en la *Figura 2.2*. En primer lugar, el haz es generado por un cañón de electrones y es acelerado mediante la aplicación de un voltaje del orden de las centenas de kV. Al igual que el SEM, el haz es enfocado y colimado mediante lentes electromagnéticas. Por otra parte, mediante el empleo de difracción de electrones (SAED), el TEM permite la obtención de imágenes del espacio recíproco, lo cual proporciona información sobre la estructura cristalina o amorfa del material.

En cuanto a la preparación de las muestras, la técnica requiere que el espesor de las mismas sea suficientemente pequeño para permitir el paso de los electrones y que estos no sean completamente absorbidos durante el proceso de transmisión. El espesor máximo que permite realizar este tipo de estudios viene determinado principalmente por el número atómico del material y por la aceleración del haz de electrones, encontrándose típicamente en el rango de las decenas o centenas de nanómetros. En el caso de que el espesor de la muestra sea mayor, se suele recurrir al adelgazamiento previo de las mismas mediante la utilización de un cañón de iones.

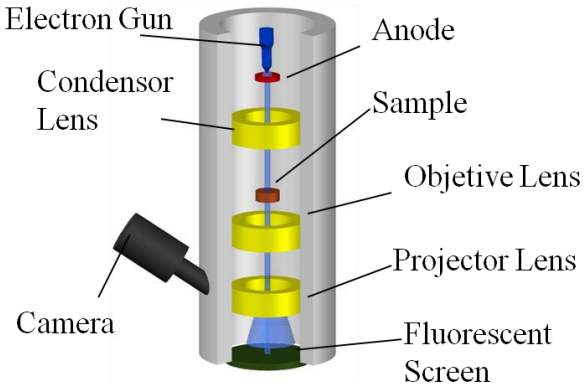

***Figura 2.2**: Esquema de un Microscopio Electrónico de Transmisión.*

Los estudios realizados con esta técnica en este trabajo de tesis, han sido llevados a cabo utilizando varios modelos de TEM (JEOL 2000 EXII, FEI TITAN y JEOL-JEM 2100F) emplazados en los SCTs de la Universidad de Oviedo y de la Universidad Autonómica de Nuevo León (UANL, México).

2.3. DIFRACCIÓN DE RAYOS-X (*XRD*)

Cuando un haz de rayos-X incide sobre un material cristalino, se produce un fenómeno de difracción en donde las interferencias constructivas vienen descritas por la ley de Bragg:

$$2dsen(\theta) = n\lambda \qquad (2.1)$$

donde n es un número entero, λ la longitud de onda de los rayos-X, d la distancia entre los planos de la red cristalina y θ el ángulo formado por los rayos incidentes y el plano de la muestra.

Existen varias configuraciones de difractómetros de rayos-X según el tipo de muestra que se pretende estudiar, no obstante en este trabajo se ha utilizado exclusivamente la configuración $\theta - 2\,\theta$, que se esquematiza en la *Figura 2.3*. Al moverse la muestra y el detector simultáneamente, la configuración $\theta - 2\,\theta$ se mantiene, con lo que sólo las difracciones producidas por los planos cristalinos paralelos a la superficie de la muestra se detectarán. Este tipo de geometría resulta especialmente útil cuando la muestra puede preparase en estado de polvo, ya que en este caso todos los planos tienen la misma probabilidad de estar orientados paralelamente al plano de la muestra, con lo que todas las direcciones cristalinas son detectadas con la misma probabilidad. En el caso de que la muestra no pueda ser preparada en estado de polvo, se debe tener en cuenta que puede existir una dirección preferencial de las direcciones cristalinas (textura cristalina), lo que implicaría la detección preferencial de la misma, complicando así el análisis cuantitativo de los diagramas de difracción.

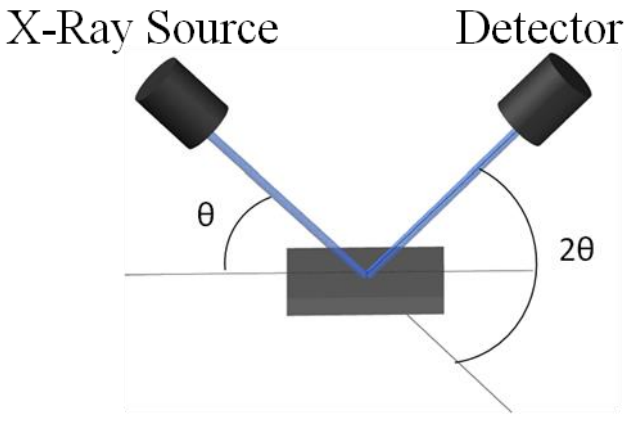

***Figura 2.3**: Esquema básico de la medida de un difractograma de rayos-X.*

Si bien mediante la ley de Bragg se puede asociar un patrón de difracción con una determinada fase cristalina, el procedimiento más común es comparar el resultado de la medida con difractogramas existentes en las bases de datos cristalográficas. Los difractómetros utilizados para este trabajo de investigación han sido un Panalytical X'Pert Pro y un Bruker D8 Discover ambos emplazados en los SCTs de la Universidad de Oviedo.

2.4. MAGNETOMETRÍA DE MUESTRA VIBRANTE (*VSM*)

El esquema del sistema experimental se ilustra en la *Figura 2.4*. En primer lugar, el dispositivo deVSM se encuentra conectado a un sistema de medida de propiedades físicas (PPMS) que controla las condiciones de medida tales como temperatura, campo magnético, etc.

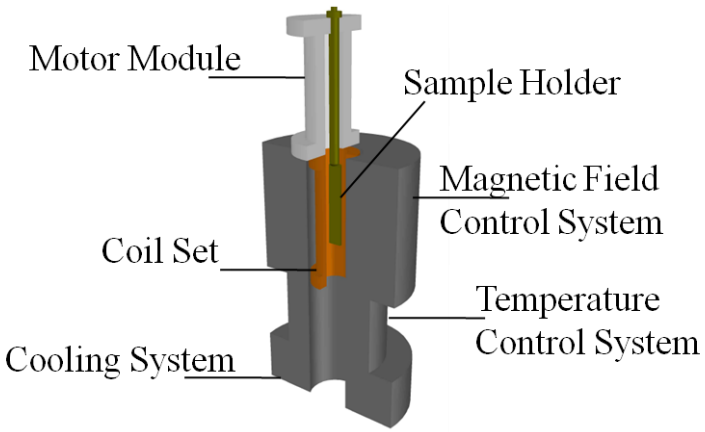

***Figura 2.4**: Componentes básicos de los que consta un sistema de magnetometría de muestra vibrante.*

El fundamento físico del VSM reside en la ley de inducción magnética de Faraday-Lenz, por lo que el cambio del flujo magnético que atraviesa una espira conductora induce una fuerza electromotriz (fem). Para este proyecto de tesis doctoral se ha utilizado un VersaLab Free de Quantum Design disponible tanto en el grupo MATMAGNANO de la Universidad de Oviedo como en el Instituto de Física Aplicada de la Universidad de Hamburgo así como un KLA-Tencor EV7 emplazado en el Instituto de Ciencia de Materiales de Madrid. En este sistema de medida, se varía el flujo magnético, que atraviesa una bobina de detección, mediante una oscilación mecánica a lo largo del eje de dicha bobina. La señal recogida, en forma de fem inducida, es proporcional a la imanación según la ecuación:

$$V_{coil} = 2\pi f C m A sin(2\pi f t) \qquad (2.2)$$

donde C es una constante de acoplamiento, m es el momento magnético de la muestra; A y f son la amplitud y frecuencia de oscilación (2mm y 40 Hz respectivamente). Para el caso particular de este modelo, los rangos de temperatura y campo magnético accesibles son 50-400 K y ±3T, respectivamente.

3. MÉTODOS DE FABRICACIÓN

En este capítulo se explican en detalle las técnicas empleadas en la fabricación de muestras para dar una visión precisa de las mismas, lo cual es de gran importancia a la hora de interpretar las propiedades físicas de los nanomateriales. La mayor parte de la fabricación se ha desarrollado mediante el uso de métodos electroquímicos, tanto para la preparación de los propios nanomateriales magnéticos como para la de las plantillas patronizadas utilizadas en el proceso de fabricación de los mismos.

3.1. ANODIZACIÓN DEL ALUMINIO

Un proceso de anodización consiste en la pasivación o formación de una capa de óxido en la superficie de ciertos metales, mediante el empleo de métodos electroquímicos, bajo condiciones controladas de temperatura, voltaje aplicado, composición y pH del electrolito utilizado, etc. Las propiedades de estos óxidos dependen fuertemente de las condiciones experimentales así como del tipo de metal utilizado como material de partida. Este tipo de proceso puede ser aplicado a diversos tipos de metales -Aluminio, Titanio, Niobio, Tántalo, Tungsteno, Zirconio,…-[Schmuki 2009], no obstante la anodización del Aluminio presenta ciertas peculiaridades con respecto a todos los demás metales considerados. Empleando determinados electrolitos ácidos, es posible crecer mediante el proceso de anodización una capa gruesa de oxido, principalmente alúmina (Al_2O_3), que presenta una alta densidad de poros con diámetro nanométrico. Más aún, bajo unas condiciones de anodización más específicas surge un fenómeno de auto-ordenamiento de los poros que da lugar a una distribución espacial hexagonal de los mismos.

El esquema básico de una celda electroquímica donde tienen lugar los procesos de anodización, se muestra en la *Figura 3.1*. Dicha celda consiste básicamente en la inmersión de dos electrodos en el medio electrolítico contenido en la propia celda. Uno de estos electrodos, el ánodo, será el metal de partida que se quiere anodizar, mientras que para el cátodo se usa un metal químicamente resistente, que habitualmente está compuesto de Platino. Ambos electrodos se conectan mediante una fuente de alimentación que proporciona bien una diferencia de potencial constante, o bien una corriente eléctrica constante, según requiera el proceso electroquímico. Los medios electrolíticos ácidos, para los casos que conciernen este proyecto de tesis doctoral, están

constituidos por disoluciones acuosas con concentraciones menores que 1M de ácido oxálico, sulfúrico o fosfórico. La elección de un ácido u otro repercutirá en las propiedades geométricas de la porosidad de la capa de alúmina crecida [Diggle 1969].

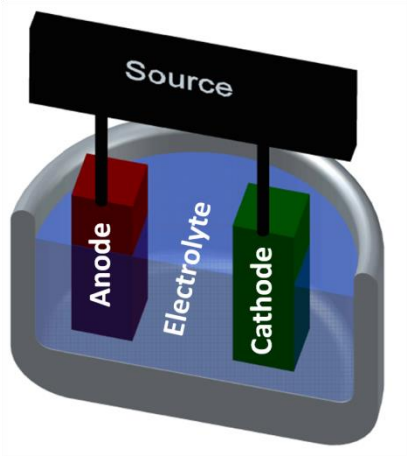

***Figura 3.1**: Imagen esquemática de una celda electroquímica.*

El proceso de anodización del aluminio se compone principalmente de dos procesos químicos que compiten entre sí, oxidación del aluminio y disolución de la capa de óxido. Obviamente, el electrolito escogido ha de ser tal que la tasa de disolución del óxido en éste sea considerablemente menor que la propia tasa de oxidación del metal. En el caso de que las condiciones experimentales se elijan de forma que se evite por completo la disolución de la capa de óxido, el resultado de la anodización es una capa densa de alúmina no porosa denominada capa barrera, cuyo espesor es proporcional a la diferencia de potencial aplicado. Únicamente para ciertos rangos de la tasas de oxidación y disolución, se dan las condiciones propicias para crecer una capa de Al_2O_3 porosa. La reacción química a través de la cual se forma la capa de Alúmina viene dada por [Alwitt 2002]:

$$2Al + 3H_2O \rightarrow Al_2O_3 + 3H_2 \qquad (3.1)$$

No obstante esta reacción está compuesta a su vez por varias reacciones tanto químicas como electroquímicas (*Figura 3. 2*) que tienen lugar en las interfases entre el metal y la capa de óxido (m/o), el óxido y el electrolito (o/e) y entre el electrolito y el cátodo (e/c) [Patermarakis 2009, Patermarakis 2011]. En primer lugar, se produce una oxidación del Aluminio metálico formándose cationes Al^{3+}, una parte de ellos reaccionan con los aniones O^{2-} producidos por la ruptura de las moléculas de H_2O en el electrolito y capaces de migrar a través de la capa de óxido debido al campo eléctrico presente en la

celda electroquímica. El resto de cationes Al^{3+} que no reaccionan para formar Al_2O_3, migran hasta el electrolito para disolverse en él y reaccionar con los aniones electrolíticos para formar sulfatos, oxalatos, fosfatos etc, dependiendo del electrolito utilizado en el proceso. Por otra parte los mismos cationes pueden reaccionar con los iones OH^- para formar hidróxidos, que junto con los complejos anteriores pueden incorporarse a la capa de alúmina.

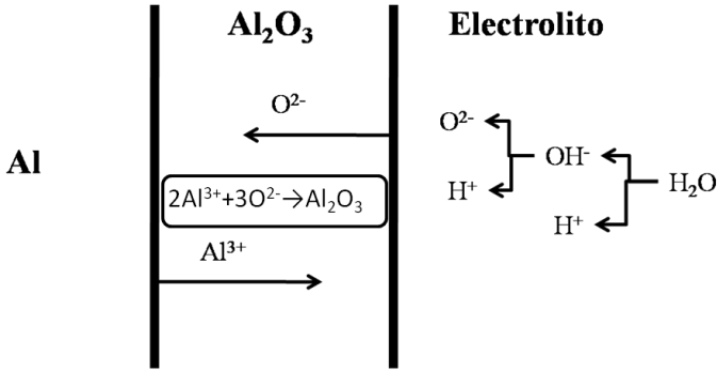

Figura 3. 2*: Reacciones de oxidación y reducción en la celda electroquímica durante el proceso de anodización del aluminio.*

En lo que concierne a las reacciones de disolución de la capa de óxido, los protones, H^+, reaccionan con la alúmina disociándola en cationes de Aluminio solubles en el medio electrolítico según la ecuación [Oh 2011]:

$$Al_2O_3 + 6H^+ \rightarrow 2Al^{3+} + 3H_2O \qquad (3.2)$$

La ecuación anterior se ve alterada por el campo eléctrico aplicado cambiando el estado de polarización de las moléculas de alúmina, lo cual sugiere que las líneas de campo eléctrico puedan tener alguna influencia en la formación de los poros. No obstante este último punto sigue siendo fuente de diversas controversias, habiéndose propuesto dos principales modelos en la formación de los poros. El primero de ellos se basa en el fenómeno anterior de disolución asistida por campo eléctrico (FAD). En los primeros instantes de la anodización al formarse la capa barrera de alúmina, las pequeñas inhomogeneidades presentadas por la superficie del Aluminio producen a su vez una inhomogeneidad en la distribución de las líneas de campo eléctrico, modificando las tasas de los procesos de oxidación y disolución a lo largo de la superficie del metal. En los puntos en los cuales la capa barrera presente menor espesor, el gradiente de campo eléctrico a través de la capa de óxido será mayor, por lo que tanto la tasa de formación de

la alúmina así como la tasa de disolución de ésta serán mayores que en los puntos donde la capa barrera tiene un mayor espesor [Jeesenky 1998, Hennesthal 2003, Prida 2007]. Lo mencionado anteriormente explicaría el proceso de formación de los poros, no obstante, no existen evidencias experimentales que corroboren dicho planteamiento.

Por otro lado, existen ciertos modelos y trabajos experimentales que contradicen el modelo FAD [García-Vergara 2006, García-Vergara 2007]. Estos trabajos utilizan bandas de Tungsteno como marcadores implantados en las láminas de aluminio para observar la evolución de los mismos durante el proceso de anodización mediante técnicas de SEM. Como resultado de estos estudios, se ha observado que dichos marcadores, durante el proceso de anodización, se desplazan desde la capa barrera en el fondo de los poros hacia el electrolito a través de las paredes de los poros. Este efecto puede ser explicado mediante el modelo del flujo plástico de la alúmina (PF). En un momento durante los primeros instantes de la anodización, mientras se crece la capa no porosa de óxido, se llega a un valor crítico del espesor de la misma que origina perturbaciones de la interfase m/o a lo largo de la superficie. A partir de este momento, las tensiones existentes generadas durante el proceso de anodización favorecen que la alúmina que crece en la base de la capa barrera difunda hacia la pared de los poros.

3.2. FABRICACIÓN DE LAS MEMBRANAS DE ALÚMINA ANÓDICA NANOPOROSA

El procedimiento para la fabricación de las membranas de alúmina nanoporosa consiste en un proceso de doble anodización electroquímica [Masuda 1995, Nielsch 2002, Prida 2007]. Dicho proceso se describe en la *Figura 3.3*, y consta de cuatro pasos básicos. En primer lugar, las láminas de aluminio de elevada pureza (99.999%) han de someterse a un proceso de limpieza y pulido de su superficie. Para el primer paso se sumergen las láminas en isopropanol durante cinco minutos en un baño de ultrasonidos. A continuación se intercambia el isopropanol por etanol y se repite el proceso anterior. Una vez aclaradas las láminas en agua ultrapura se las somete a un proceso de pulido electrolítico para reducir la rugosidad superficial de las mismas. Para este paso se sumergen las láminas de aluminio en un electrolito formado por ácido perclórico y etanol en una proporción de 1|3 en volumen. Después de aplicar una diferencia de potencial de 20 voltios durante un

periodo de unos 8 minutos, donde el aluminio actúa como ánodo y un electrodo de platino como cátodo, las láminas de Al presentan una superficie especular.

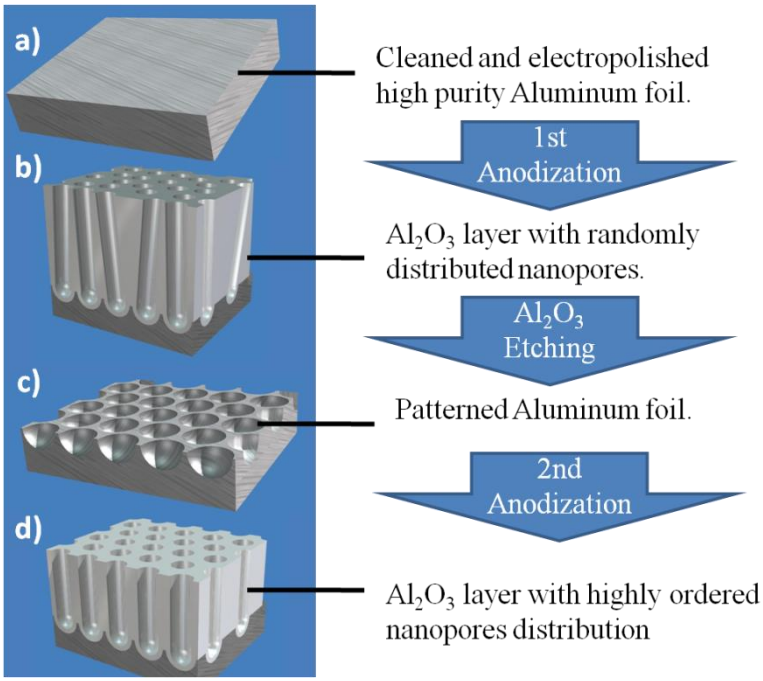

***Figura 3.3**: Proceso de doble anodización del Aluminio para la fabricación de alúmina nanoporosa altamente ordenada.*

El siguiente paso consiste en la primera anodización de las láminas de aluminio. A tal efecto se disponen las láminas en la celda electroquímica esquematizada en la *Figura 3.1*. Dependiendo tanto del electrolito utilizado como de la diferencia de potencial aplicada, las características geométricas de las membranas porosas pueden modificarse convenientemente. No obstante, las condiciones experimentales expuestas para cada uno de los casos aquí estudiados serán tratadas en su sección respectiva. Durante la primera etapa de anodización los poros crecen de forma aleatoria sin ser paralelos entre sí. No obstante a medida que aumenta la longitud de los mismos, surge un fenómeno de auto-ordenamiento, debido al cual los poros comienzan a crecer de forma paralela tendiendo a una distribución espacial hexagonal altamente ordenada. El mínimo tiempo que se ha estimado como óptimo para obtener un alto ordenamiento de los poros es de unas 24 horas de primera anodización.

Teniendo en cuenta que los poros de la capa de óxido crecida en el proceso anterior no presentan ordenamiento a lo largo de todo el espesor de la misma, se somete la muestra a un ataque químico selectivo de la capa de alúmina. Para tal propósito se sumerge la muestra en una disolución acuosa cuya composición es $0.18M\ CrO_3 +$

$0.61M\ H_3PO_4$, a una temperatura de unos 40-45 ºC durante un periodo de tiempo suficiente para eliminar por completo la capa de alúmina (típicamente 6-12 horas). Una vez eliminado todo el óxido, la superficie de la lámina de aluminio muestra el patrón, altamente ordenado, transferido por los poros de la capa de alúmina producida durante la primera anodización.

Una vez efectuado el proceso anterior se vuelve a anodizar la lámina patronizada de aluminio bajo las mismas condiciones electroquímicas de la primera anodización. Entonces los poros comienzan a crecer siguiendo el patrón ordenado de la superficie y manteniendo dicho orden a lo largo del espesor de la capa de alúmina (*Figura 3.3*, d). El espesor final de la capa de alúmina vendrá determinado por la tasa de crecimiento de la misma que depende del tipo de electrolito y condiciones utilizadas, y del tiempo durante el cual se mantenga la segunda anodización.

3.3. SISTEMA EXPERIMENTAL DE ANODIZACIÓN ELECTROQUÍMICA

Un esquema del dispositivo experimental de anodización se muestra en la Figura 3.4. En primer lugar, la celda electroquímica, fabricada fundamentalmente de un material químicamente resistente como el teflón, consta además de una placa de Cu en contacto con la lámina de Al, cuya función es proporcionar buen contacto tanto térmico como eléctrico. Las láminas de aluminio empleadas en el desarrollo de este trabajo y suministradas por la empresa Goodfellow tienen típicamente un espesor de medio milímetro y una pureza del orden de 99.999%. Por otro lado, confrontado a la lámina a anodizar se dispone una red de hilo de Pt que actúa como cátodo en el proceso de anodización, (ver recuadro en *Figura 3.4*). Dicha celda electroquímica se sitúa sobre un plato frío, que consiste en una pieza de cobre por cuyo interior se hace circular un flujo de líquido refrigerante. La temperatura de este baño se controla por medio de un recirculador (modelo "Thermo Haake Phoenix II") que permite seleccionarla y mantenerla constante a lo largo del proceso de anodización. La diferencia de potencial aplicada a la celda electroquímica es suministrada por una fuente de alimentación (modelos "Keithley 2400 SourceMeter" o "Xantrex 300-9"), que se controla mediante ordenador a través de un puerto GPIB. El software empleado para monitorizar el proceso de anodización, a través de un multímetro ("Fluke 45 Dual Display Multimeter"), fue desarrollado y optimizado en el propio laboratorio [Vega 2006, Vega 2008].

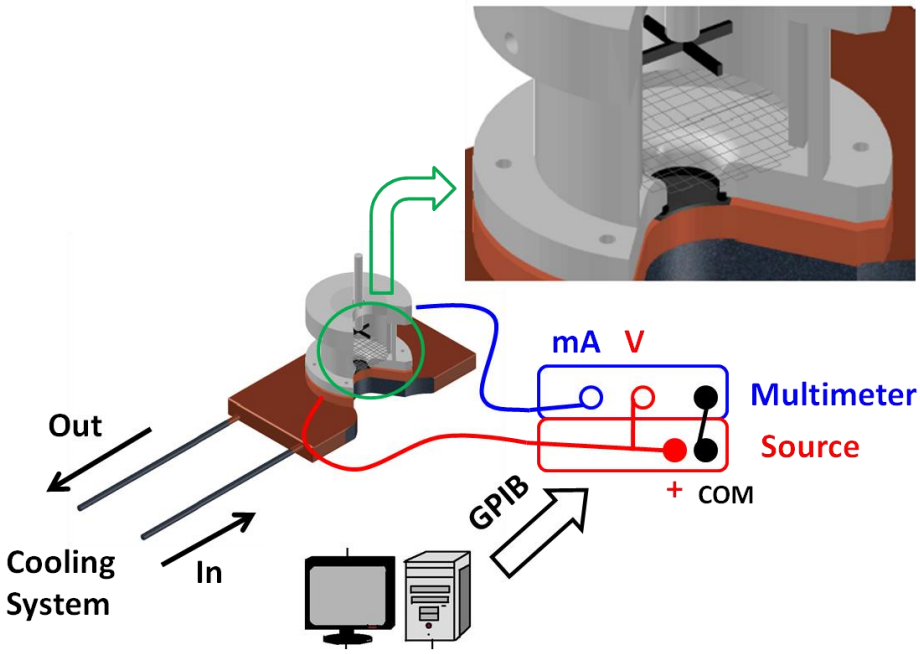

Figura 3.4: *Ilustración del sistema experimental utilizado para la fabricación de las membranas de alúmina nanoporosa.*

3.4. CARACTERÍSTICAS GEOMÉTRICAS DE LA CAPA POROSA DE ALÚMINA

Si bien el proceso de doble anodización es independiente del tipo de electrolito empleado en la misma, las condiciones experimentales para las cuales se obtiene un ordenamiento elevado de los poros son distintas en cada caso.

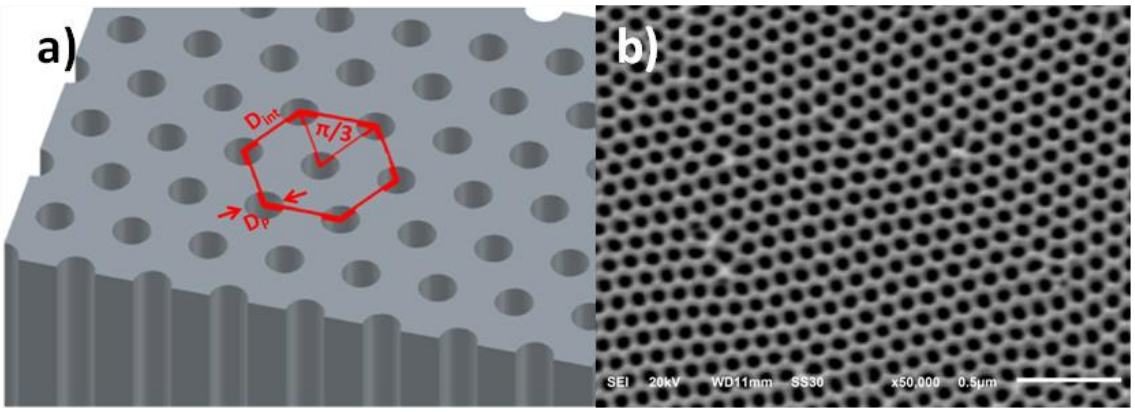

Figura 3.5: *Detalle del arreglo ordenado de los nanoporos de una membrana de alúmina anódica nanoporosa; a) Representación de la celda unidad, b) Imagen de SEM de la superficie de la capa nanoporosa de Al_2O_3.*

En la *Figura 3.5* se presentan todos los parámetros utilizados para definir las distintas propiedades geométricas de una capa de alúmina nanoporosa, tales como el diámetro de poro (D_p), distancia entre poros (D_{int}) y la porosidad P. Ésta última mide la

proporción superficial de los poros con respecto al área total de la capa de alúmina [Nielsch 2002]. Teniendo en cuenta la simetría de la celda unidad hexagonal centrada en la cual se distribuyen los poros, el área de dicha celda podrá expresarse de la forma:

$$A_{C.U} = 6\frac{D_{int}}{2}\left(D_{int}\cdot\cos\left(\frac{\pi}{6}\right)\right) = \frac{3\sqrt{3}}{2}D_{int}^2 \qquad (3.3)$$

El área de los poros situados en los vértices de la celda hexagonal es compartida por tres celdas, por lo que el área total de los poros que se encuentra dentro de la ceda unidad se expresaría:

$$A_p = \left(\frac{6}{3}+1\right)\pi\left(\frac{D_p}{2}\right)^2 = \frac{3}{4}\pi D_p^2 \qquad (3.4)$$

con lo que finalmente la porosidad puede definirse de la siguiente forma.

$$P(\%) = 100\cdot\frac{A_p}{A_{C.U.}} = 100\frac{\pi}{2\sqrt{3}}\left(\frac{D_p}{D_{int}}\right)^2 \qquad (3.5)$$

En este trabajo se han utilizado principalmente membranas de alúmina nanoporosa crecidas mediante la utilización de ácido oxálico $(COOH)_2$, lo cual proporciona una geometría y distribución de los poros determinada. Las condiciones experimentales de fabricación, así como los parámetros de red típicos a los que dan lugar, se encuentran resumidas en la *Tabla 3.1*.

Concentración Electrolito	**Temperatura(ºC)**	$\boldsymbol{V_{an}(V)}$	$\boldsymbol{D_p(nm)}$	$\boldsymbol{D_{int}(nm)}$	**P(%)**	**Tasa de crecimiento** $\boldsymbol{(\mu m/h)}$
0.3M	1-3	40	35	105	10	2.5

Tabla 3.1*: Condiciones experimentales de anodización y parámetros geométricos de la distribución de poros de las láminas de Al_2O_3. (Van=Voltaje de anodización aplicado entre el contraelectrodo de Pt y el sustrato de Al; Dp= diámetro de poro; Dint= Distancia entre poros; P= Porosidad de la capa nanoporosa de alúmina)*

Las condiciones anteriores se han optimizado para obtener un elevado ordenamiento hexagonal de los poros. Aunque aquellas fijan la geometría mostrada por la capa de alúmina, la variación de alguna de dichas condiciones (voltaje de anodización aplicado entre el contraelectrodo de pt y la lámina de Al (V_{an}), concentración del electrolito,…) puede alterar las propiedades geométricas de la capa de óxido,

modificándose así el valor de la porosidad de la misma [Nielsch 2002]. No obstante, mediante procesos de ataque químico efectuados una vez la capa de alúmina se ha formado, se puede variar la porosidad a través del ensanchamiento de los poros como se discutirá más adelante.

3.5. PROCESOS DE ANODIZACIÓN DURA

Recientemente, un nuevo tipo de proceso de anodización electroquímica de láminas de aluminio ha adquirido enorme interés debido a sus potenciales aplicaciones. Este tipo de anodización, denominada anodización dura frente a la anodización convencional o proceso de anodización "suave", presenta un alto grado de ordenamiento de los poros en un gran rango de condiciones experimentales [Chu 2005, Lee 2006], mediante un único proceso de anodización con una tasa de crecimiento mucho mayor que en los casos estudiados anteriormente [Ha 2010, Santos 2011]. En lo que concierne a esta tesis doctoral, las membranas crecidas mediante este método han sido fabricadas en un medio ácido compuesto por 0.3M $(COOH)_2$ en una disolución de H_2O y etanol en una proporción de 19 a 1 [Vega 2012b]. El esquema de una capa nanoporosa de alúmina crecida tras seguir un proceso de anodización dura puede verse en la *Figura 3.6*.

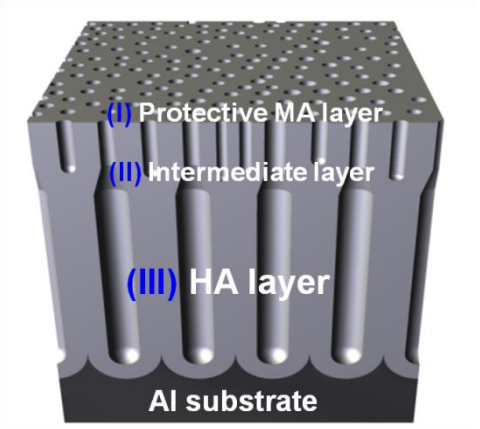

***Figura 3.6**: Esquema de una lamina de Al_2O_3 crecida mediante anodización dura.*

El proceso de anodización dura consta de tres etapas. En primer lugar se crece una capa de oxido bajo un régimen de anodización suave (80V,1-3ºC) durante unos 10 min. El propósito de esta capa inicial de oxido es proteger la lámina de aluminio durante los primeros instantes del proceso de anodización dura, limitando la corriente y por tanto evitando la ruptura dieléctrica que puede provocar daños irreversibles en la lámina debido al calentamiento de la celda. A continuación, se reduce la temperatura de la celda

electrolítica hasta -1→0ºC para aumentar a continuación el potencial aplicado a la celda electroquímica mediante una rampa de 0.08V/s hasta alcanzar un valor de 140 V. Durante este proceso se alcanza el régimen de anodización dura caracterizado por estar limitado por difusión iónica debido a la rapidez de crecimiento de la capa de óxido y al elevado valor del potencial aplicado. Una vez alcanzado el régimen de anodización dura, en torno a 105V, se produce el auto-ordenamiento de los poros siguiendo una estructura hexagonal, ya que una vez finalizada la rampa de voltaje, el proceso ha tenido suficiente tiempo para generar un alto grado de orden en el crecimiento de los poros. A partir de este momento se mantiene la anodización a potencial constante, por un periodo de tiempo determinado dependiendo del espesor deseado. En la *Tabla 3.2*, se muestran los parámetros geométricos de las membranas crecidas por este método de anodización.

Preanodización	**Rampa**	$\boldsymbol{V_{an}(V)}$	$\boldsymbol{D_p(nm)}$	$\boldsymbol{D_{int}(nm)}$	**P(%)**
80 V	0.08 V/s	140	~70	300	~5

Tabla 3.2*: Condiciones experimentales y parámetros geométricos de la distribución de poros de las láminas de Al_2O_3 crecidas por anodización dura. (Van=Voltaje de anodización aplicado entre el contraelectrodo de Pt y el sustrato de Al; Dp= diámetro de poro; Dint= Distancia entre poros; P= Porosidad de la capa nanoporosa de alúmina)*

3.6. OBTENCIÓN DE LAS MEMBRANAS DE ALÚMINA NANOPOROSA

En la *Figura 3.7* se muestran los diferentes pasos necesarios para transformar la capa de alúmina nanoporosa en la membrana que se utilizará como plantilla. En primer lugar es necesario eliminar la lámina de aluminio no anodizado restante. Para ello se recurre a un ataque químico selectivo del aluminio, mediante la utilización de una disolución acuosa compuesta por 36 g/l de $CuCl_2 \cdot 2H_2O$ añadiendo 500ml/l de HCl al 37% [Navas 2007]. Para llevar a cabo este proceso se emplea la misma celda electroquímica, invirtiendo la lámina anodizada para exponer el Aluminio al ataque del medio ácido. Este ataque también afecta a la alúmina, pero a un ritmo mucho menor, por lo que seleccionando apropiadamente el tiempo de ataque óptimo se puede eliminar la capa de aluminio permaneciendo la alúmina intacta.

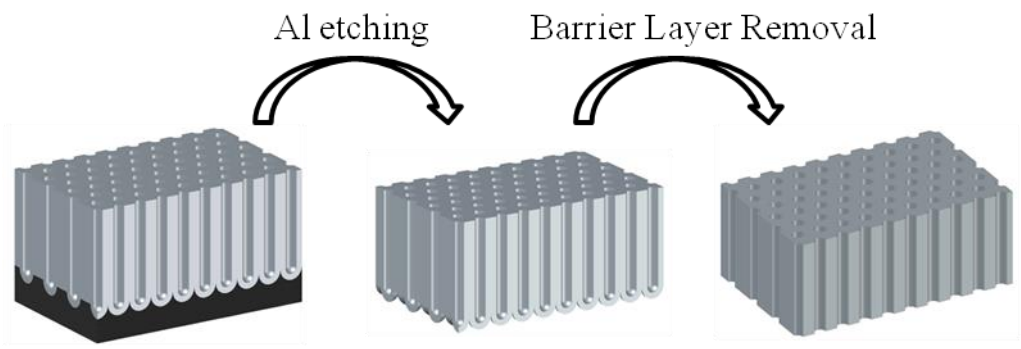

***Figura 3.7**: Esquema de los distintos pasos de ataques químicos necesarios para fabricar las membranas de alúmina nanoporosa abiertas por ambos extremos.*

El proceso anterior tiene como resultado una membrana de Al_2O_3 libre de Aluminio, no obstante una de sus superficies aún está cerrada debido a la presencia de la capa barrera. Para los procesos que luego tendrán lugar en la fabricación de los nanohilos magnéticos, se necesita que ambas superficies de la membrana de alúmina tengan los poros abiertos. La eliminación de la capa barrera se realiza, en general, también por métodos químicos, aunque también se pueden emplear otros métodos basados en bombardeo iónico como el Reactive Ion Etching (RIE) . Manteniendo la membrana en la celda electroquímica, se expone la superficie de la capa barrera al ataque de una disolución acuosa de ácido ortofosfórico diluido un 5% en peso. La velocidad, así como la homogeneidad del ataque de la capa barrera de alúmina por el medio ácido, depende fuertemente de la temperatura del proceso. Con una temperatura del baño ácido de 30ºC se consigue una apertura de la capa barrera apreciablemente homogénea, prolongando la duración del mismo hasta observar que el ácido atraviesa la membrana y empapa un papel absorbente colocado sobre la superficie libre de la membrana.

Una vez obtenida la membrana de alúmina con los poros abiertos por ambos extremos, es posible modificar el tamaño del poro como se ha comentado anteriormente. Sumergiendo la membrana en el mismo medio ácido que en el proceso anterior y a la misma temperatura, es posible aumentar el diámetro de los poros mediante ataque químico. La tasa de ensanchamiento del diámetro de los poros a 30ºC se sitúa en torno a 1 nm/min aumentandose la porosidad de la membrana ya que durante este proceso la distancia entre los poros no se ve alterada.

Para realizar el proceso de deposición electroquímica de los nanohilos metálicos utilizando las membranas de alúmina como plantillas, resulta necesario crecer un contacto eléctrico en uno de los extremos de la membrana para que actúe como cátodo durante el

proceso. Para ello, se metaliza con Au una de las caras de la membrana mediante un sputtering comercial (SC7620 Sputter Coater, Polaron). No obstante, este proceso no es suficiente para obtener un recubrimiento uniforme debido a la naturaleza porosa de la superficie (ver *Figura 3.8*, a)). Para cubrir por completo la superficie de la membrana y crecer nanocontactos de Au en el interior de los poros, se utiliza la capa de Au crecida por sputtering como cátodo inmersa en un electrolito comercial (OROSENE 999 R.T.U.). Aplicando una diferencia de 2.4V entre la membrana (cátodo) y un ánodo de Pt, se logra crecer una capa gruesa y homogénea de Au empleando un periodo de electrodeposición entorno a 15-20 min (ver *Figura 3.8*, b)).

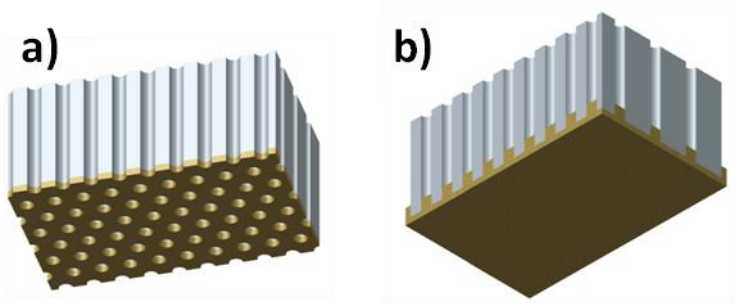

***Figura 3.8**: Membrana de alúmina con una de las superficies metalizada con Au por sputtering a); Después de electrodepositar una capa de Au sobre la misma b).*

3.7. ELECTRODEPOSICIÓN UTILIZANDO MEMBRANAS NANOPOROSAS DE ALÚMINA ANÓDICA COMO PLANTILLAS

En los procesos de electrodeposición, los iones de metales disueltos en un medio electrolítico M^{n+} son dirigidos hacia un sustrato conductor (cátodo) mediante un campo eléctrico aplicado. En la superficie del sustrato que se quiere recubrir con dicho metal, se producen reacciones de transferencia electrónica del tipo $M^{n+} + ne^{-} \leftrightarrow M$, por las cuales el metal reducido se deposita en la superficie del cátodo [Paunovic 1998]. En el estado de equilibrio de la reacción reversible anterior, durante el cual se establece un balance entre las reacciones de oxidación y reducción de la especie metálica, se genera una diferencia de potencial debida a estos procesos que se denomina potencial de equilibrio (E^{eq}). Dicho potencial depende de las actividades de las especies tanto oxidadas ($a_{M^{n+}}$) como reducidas (a_M), y de la temperatura absoluta T a través de la ecuación de Nerst:

$$E^{eq} = E^{0} + \frac{RT}{nF} ln\left(\frac{a_{M^{n+}}}{a_M}\right) \qquad (3.6)$$

donde R es la constante de los gases ideales (R=8.314 $J \cdot K^{-1} \cdot mol^{-1}$), F la constante de Faraday (F=96485.339 $C \cdot mol^{-1}$) y T está medida en Kelvin. Debido a que E^{eq} no puede calcularse de forma directa, se escoge el electrodo de hidrógeno como referencia que por convenio se considera como cero. De esta forma se define E^0 como el potencial normal de electrodo, midiendo el potencial de electrodo de un cierto elemento con respecto al electrodo de hidrógeno en condiciones estándar de concentración y temperatura. No obstante, es necesario desplazar la reacción fuera del equilibrio para conseguir una deposición neta de material metálico en la superficie del cátodo. Mediante un potencial externo aplicado, llamado sobrepotencial (η), se consigue desplazar la ecuación fuera del estado de equilibrio de tal forma que $E^{dep} = E^{eq} + \eta$ proporciona una deposición efectiva de material a una tasa de crecimiento determinada.

Los procesos de electrodeposición, al ser procesos electroquímicos, se realizan por regla general siguiendo el esquema de celda electroquímica de la *Figura 3.1*. Si bien en un sistema de dos electrodos la caída de potencial, entre el electrodo de trabajo y el contraelectrodo, vendrá determinada por las reacciones redox en las superficies de ambos y la caída de potencial en el electrolito, que será proporcional a la resistencia eléctrica ofrecida por éste y en consecuencia, dependerá de la concentración de los iones metálicos disueltos en el mismo. Más concretamente, esta última contribución no depende sólo del tipo de electrolito, sino que también no permanece constante durante el proceso ya que la concentración del electrolito varía al empobrecerse la concentración de los iones disueltos durante su electrodeposición sobre el electrodo de trabajo. La utilización de un electrodo de referencia en la medida de la diferencia de potencial en la celda electroquímica (ver Figura 3.9), sustituye el potencial debido al contraelectrodo por el potencial de equilibrio del electrodo de referencia, el cual es conocido y estable. A su vez, entre el electrodo de referencia y el de trabajo la corriente es generalmente muy pequeña, por lo que el valor medido de la caída de potencial ohmica en el electrolito es despreciable. De este modo el electrodo de referencia proporciona un valor de la diferencia de potencial de la celda electrolítica que involucra, además de su potencial de equilibrio, el potencial debido a las reacciones que tienen lugar en el electrodo de trabajo y que son responsables de la deposición del material [Oldham 1994].

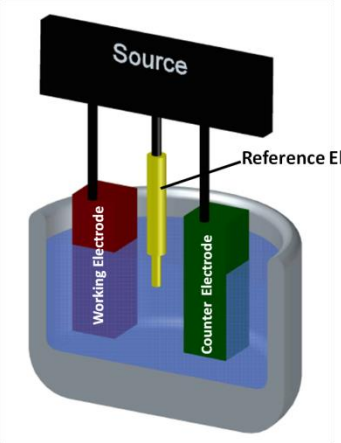

***Figura 3.9**: Imagen esquemática de una celda electroquímica de tres electrodos utilizada en procesos de electrodeposición.*

Para la electrodeposición de nanohilos metálicos, en general se utiliza el esquema de la Figura 3.9. En este caso las membranas de alúmina fabricadas con los nanocontactos de Au actúan como electrodo de trabajo y un electrodo de Pt como contraelectrodo, mientras que el electrodo de referencia utilizado en el desarrollo de esta tesis doctoral ha sido un electrodo de Ag/AgCl.

Debido a que el proceso de deposición del metal es puramente electroquímico, los iones disueltos en el electrolito sólo se depositan en el material conductor del electrodo de trabajo. Esto implica que al usar las membranas de alúmina como plantillas, se rellenen los poros de aquellas desde la base donde inicialmente sólo se encuentran los nanocontactos de Au hasta una altura determinada que dependerá principalmente de la tasa de crecimiento del depósito y del tiempo de electrodeposición. El resultado obtenido tras un proceso de electrodeposición como el descrito, empleando membranas nanoporosas de alúmina como plantillas, consiste en nanohilos metálicos embebidos en la matriz porosa de alúmina como se puede apreciar en la *Figura 3.10* [Nielsch 2000, Vázquez 2005, Prida 2007].

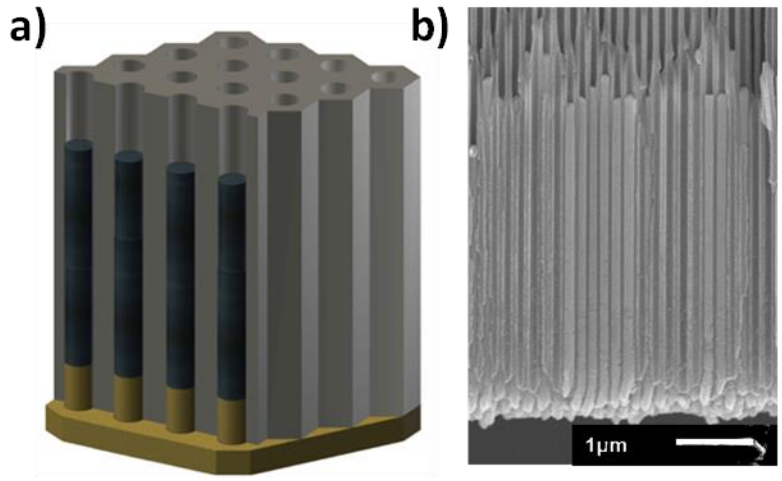

***Figura 3.10**: Arreglo de nanohilos crecidos por electrodeposición utilizando la membrana nanoporosa de alúmina como plantilla; a) Esquematización, b) Imagen SEM.*

Una de las principales limitaciones del método de electrodeposición potenciostático reside en la necesidad de la utilización de un electrodo de referencia para llevar a cabo dicho proceso. Cuando ciertos procesos se pretenden escalar a la industria, la utilización de dichos electrodos de referencia no es viable debido a la mayor complejidad de la celda electroquímica de tres electrodos y el mantenimiento que estos electrodos llevan consigo, lo que incrementaría en gran medida los costes de fabricación. En este punto los procesos de electrodeposición galvanostática ofrecen una mayor simplicidad del sistema experimental de fabricación ya que no requieren electrodo de referencia, pudiéndose emplear celdas electroquímicas de dos electrodos. Estos métodos de electrodeposición galvanostática consisten en suministrar una corriente catódica a la celda electroquímica. Ya que la corriente y el voltaje están directamente relacionados, pueden controlarse y establecerse los parámetros electroquímicos necesarios para la fabricación de materiales metálicos. Por otro lado, la cantidad de corriente catódica en la celda unidad, a una diferencia de potencial determinada, depende fuertemente de las dimensiones de los electrodos. Si bien la superficie del contraelectrodo de platino es constante, es especialmente útil conocer la superficie del sustrato o electrodo de trabajo para poder expresar la corriente en términos de la densidad de corriente, lo cual permite una mayor reproducibilidad del proceso y una independencia del tamaño o geometría del sustrato empleado en la electrodeposición. No obstante, en el caso específico de la electrodeposición en membranas de alúmina nanoporosa, es difícil conocer la superficie efectiva del sustrato que viene determinada por la porosidad de dicha membrana.

Por último, la electrodeposición pulsada es otro tipo de proceso electroquímico de deposición empleado en este trabajo. Este tipo de electrodeposición consiste en la sucesión de procesos potenciostáticos y/o galvanostáticos en la celda electroquímica, aplicados de forma periódica durante el proceso de electrodeposición [Nielsch 2000, Prida 2007]. Una de las principales aplicaciones de este método en la fabricación de nanohilos metálicos, utilizando membranas de alúmina anódica nanoporosa como plantillas, reside en la aplicación de un pulso de deposición seguido por otro pulso de descanso donde se favorece la homogeneidad composicional y pH del electrolito en el fondo de los poros. El hecho de homogeneizar el electrolito durante el periodo de descanso, repercute a su vez muy notablemente en la homogeneidad de los depósitos crecidos por esta técnica. Por otro lado, un caso específico de la preparación de las plantillas mediante reducción de capa barrera, que se explicará de forma más detallada en el capítulo 7, presentan una capa muy delgada de material eléctricamente aislante que separa el electrolito del Al conductor del sustrato. Esto puede ser visto como un condensador cuya polarización hace que en periodos suficientemente largos de deposición contrarreste la diferencia de potencial aplicada parando el proceso de electrodeposición. Para provocar la descarga de dichas acumulaciones de carga, se aplica un pulso de potencial anódico previo al pulso de deposición. Un ejemplo de esquemático de la electrodeposición pulsada puede encontrarse en la *Figura 3.11*.

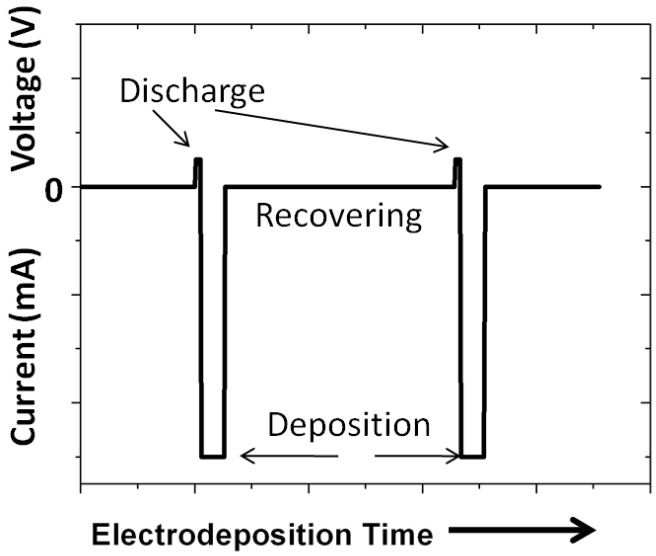

***Figura 3.11**: Esquema de los distintos pasos que constituyen un proceso de electrodeposición pulsada en membranas de alúmina nanoporosa con reducción de capa barrera.*

En el caso de muchos electrolitos que contienen distintos tipos de iones metálicos en la disolución, la aleación resultante en el proceso de electrodeposición depende fuertemente del potencial o corriente aplicados a la celda electroquímica. Esto permite que mediante la combinación de distintos procesos potenciostáticos y/o galvanostáticos, con distintas condiciones eléctricas, en un mismo proceso de electrodeposición, se puedan realizar estructuras heterogéneas las cuales presenten una modulación de la composición que estará directamente relacionada con los distintos pulsos implicados en el proceso. Este último caso será empleado en la fabricación de nanohilos multisegmentados de aleaciones de Co-Ni, y que será estudiado en el capítulo 5 del presente trabajo.

3.8. TÉCNICAS DE CRECIMIENTO POR DEPOSICIÓN DE CAPAS ATÓMICAS

La deposición de capas atómicas o ALD, de sus siglas en inglés *Atomic Layer Deposition*, es una técnica de fabricación basada en los métodos de deposición química en fase vapor o CVD. A diferencia de las técnicas PVD (*Physical Vapor Deposition*), altamente anisotrópicas, las técnicas de CVD son idóneas para la fabricación de recubrimientos, generalmente óxidos, sobre sustratos cuya superficie muestra una morfología compleja. Los procesos o reacciones químicas que tienen lugar durante la fabricación de un recubrimiento por ALD se esquematizan en la Figura 3.122. En primer lugar, el proceso de deposición por ALD es un proceso cíclico que consta de dos o más precursores en estado gaseoso, por ejemplo A y B. El sustrato a recubrir se expone a dichos precursores secuencialmente, de tal forma que en el primer paso las moléculas del precursor A funcionalizan la superficie del sustrato preparándola así para la posterior exposición de las moléculas del precursor B, que contienen el material a depositar. El precursor B reacciona entonces con los grupos funcionales de la superficie del sustrato quedando adherido a éstos mediante enlaces covalentes. A continuación se purga el gas restante del precursor mediante una bomba de vacío y un flujo de gas inerte, típicamente Ar o N. Para eliminar los grupos funcionales de los que constan las moléculas del precursor B, en el tercer paso se vuelve a exponer el sustrato al precursor A, el cual reacciona con éstos, replicando el estado inicial de la superficie haciendo posible que se pueda repetir el proceso cíclicamente. No obstante, antes de repetir el proceso se añade otro paso de purga para eliminar el gas restante del precursor A. El espesor de la capa depositada será proporcional al número de ciclos ALD efectuados, entendiendo ciclo como el compuesto por los dos pasos de exposición a precursores y los dos de purga. Si

durante los pulsos de exposición toda la superficie del sustrato es funcionalizada por las moléculas del precursor, y los pulsos de purga son suficientemente largos, se dice que el proceso ALD está limitado por la superficie. Este régimen de deposición se caracteriza porque aunque aumente la duración de los pulsos de exposición, la tasa de crecimiento permanece constante, siendo así un proceso puramente de ALD.

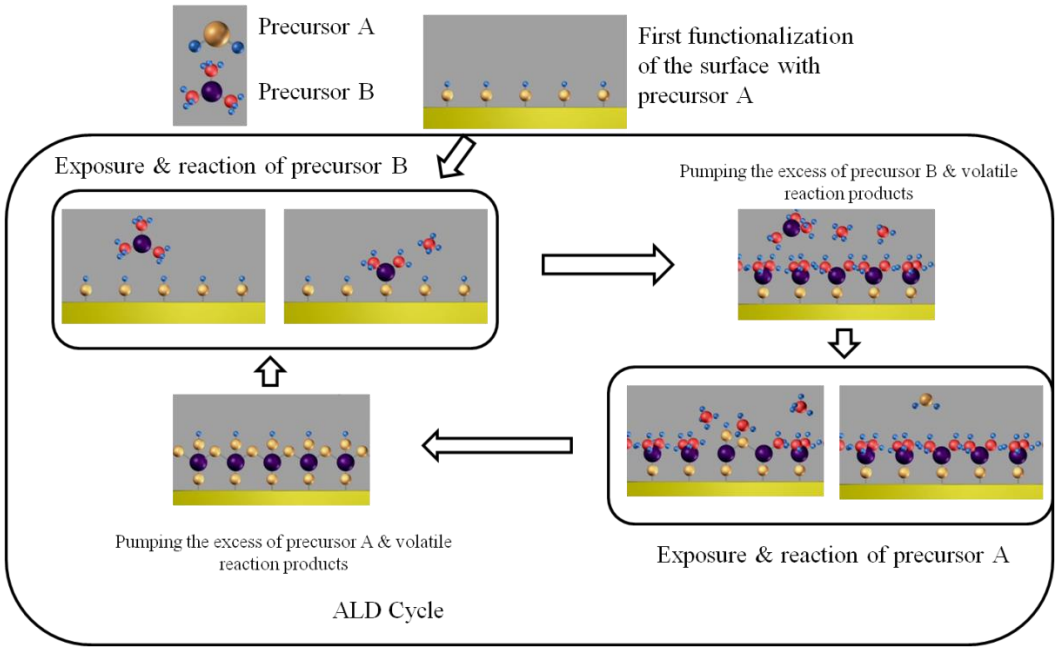

***Figura 3.12**: Esquematización de un proceso de ALD en el que están involucrados los precursores A y B. Imagen tomada de Ultratech/CambridgeNanoTech ™.*

La principal aplicación de la técnica de ALD para el desarrollo de la tesis doctoral ha consistido básicamente en la deposición de Al_2O_3 o SiO_2 en las membranas de alúmina. En el primero de los casos, una vez obtenidas las membranas de alúmina, se realiza una de posición de Al_2O_3 mediante ALD para reducir el tamaño de los poros y así reducir la porosidad de la membrana. Por otro lado, la deposición de SiO_2 sobre las membranas de alúmina resulta de especial interés para la formación de estructuras tipo núcleo-corteza o *"core-shell"*. En este caso, la deposición de SiO_2 previa a la electrodeposición funcionaliza la superficie de la membrana de tal forma que una vez crecidos los nanohilos metálicos, la superficie de éstos también estarán protegidos por la capa de SiO_2, más resistente químicamente que la alúmina anodizada [Bachman 2008]. Esta deposición de SiO_2 evitará la oxidación de los nanohilos cuando se pretenda liberarlos de la plantilla de alúmina mediante ataque químico para un posterior estudio de nanohilos individuales.

4. Analysis of Magnetization Processes in Nanomaterials by First Order Reversal Curves

In this chapter, the analysis of first order reversal curves (FORCs), used to extract valuable information of different magnetic systems will be discussed. First of all, a general view of the fundamental theory behind this method, based on the Preisach model of hysteresis, will be shown. Furthermore, the measurement procedure of dc magnetization curves as well as the interpretation of the measurement for different magnetic systems will concern an important part of the chapter. Finally, the interpretation of such FORC diagrams will be also supported by a self made program in Matlab®, which treats the FORC analysis from the statistical point of view.

4.1 Preisach Model of Hysteresis

The evaluation of all the physical phenomena that are involved in the hysteretic processes that take place in many materials is still an object of intensively study. The starting point to explain a global hysteretic behavior is to define an elemental hysteretic process that, in principle, is determined by the intrinsic nature of the material. Hereinafter, this study will be focused in the magnetization response of a magnetic material with an external applied field, i.e. the hysteresis loops. In this context, the elemental magnetization event is defined as a hysteron, which is characterized by the field parameters defined and shown in *Figure 4.1*. If we consider that in at initial state the fraction of the material related to this hysteron is negatively saturated, the magnetization reversal process requires of an applied field $H > H_b$ to take place. Furthermore, to recover the initial magnetization state, H has to pass through H_r fulfilling the condition $H < H_r$. What depends on the specific magnetic process whereby the inversion of the magnetization takes place is given by the hysteresis of the hysteron $(H_b - H_r)$. If we consider an isolated hysteron, it should be centered along the magnetization axis. However other events that can also be present, shifts the hysteron with respect that axis through interactions of different natures as will be discussed later on.

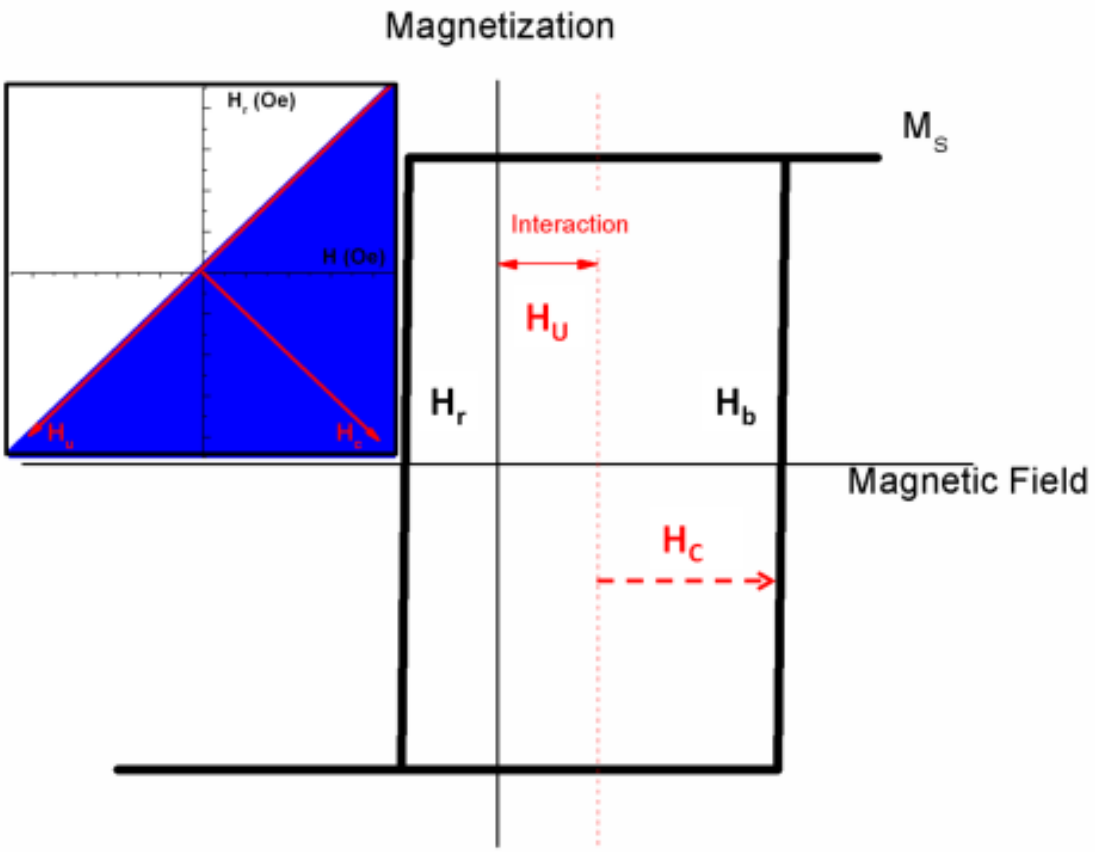

Figure 4.1: *Typical hysteron defined by the field parameters of switching (H_r,H_b). Other field parameters that are useful defining the hysteron properties are (H_C,H_U) which are related to the switching and the interaction respectively. The inset shows the Preisach plane(in blue).*

In general, the magnetization reversal process of a given material is composed by a distribution of intrinsic elementary magnetization processes. Moreover, the global behavior is not only determined by that distribution, but rather by a distribution of unitary magnetization events including interactions, from different origins, among them. In this sense, it is possible to define a uniform distribution of hysterons, characterized by their own values of H_b and H_r known as the classical Preisach distribution ($\rho(H_b, H_r)$) [Preisach 1935, Della Torre 1999]. Taking into account that necessarily $H_b > H_r$, the Preisach distribution for a given maximum value of both is only defined in a triangular region of the Preisach plane (H_b, H_r), which is illustrated in the inset of *Figure 4.1*. The aim of the Preisach model is to explain not only the major hysteresis loops but rather the minor hysteresis loops of a magnetic material through a uniform distribution of hysterons $\rho(H_b, H_r)$. In order to differentiate mathematically all the parameters involved in a magnetization process, it becomes necessary to define a function or distribution that takes into account the magnetic state of each hysteron. This function is defined as Preisach state function, $Q(Hr, Hb)$, which takes the value 1 when the hysteron with the

same values of H_b and H_r is positively saturated and -1 otherwise. Then, the normalized magnetization is given by the equation:

$$m = \iint_{H_b > H_r} Q(Hr, Hb) \cdot \rho(H_b, H_r) dH_b dH_r \qquad (4.1)$$

In the previous equation, ρ has the information of each "hysteron shape" and Q is a function that determines the magnetic state of each hysteron given by Hr and Hb. In order to work with normalized magnitudes, the Preisach distribution is chosen so that the value of the integral is equal to 1, when all the hysterons are magnetized along the same direction. Furthermore, when a hysteron switches its magnetic state, it changes from -1 to 1, which means that each time one hysteron switches contributes to the change of the magnetization by a factor of 2, allowing rewriting the equation (4.1) as follows:

$$m = -1 + 2 \iint_{H_b > H_r} \rho(H_b, H_r)\, dH_b dH_r \qquad (4.2)$$

The classical Preisach model of hysteresis has two main limitations [Mayergoyz 1986, Mayergoyz 1991]. Those limitations fix when a certain hysteresis process can be explained by the classical Preisach distribution $\rho(H_b, H_r)$. The first condition that the magnetic material must satisfy is the congruency property. In this case, every minor loop performed between the same pair of H_b and H_r values should show the same magnetization variation, what means that all of these minor loops should be geometrically congruent. On the other hand, the wiping-out or deletion property imposes a local memory of the magnetic behavior which implies that each minor loop depends on its starting point. In other words, each minor loop measured between a given H_b and H_r values has to be a closed cycle. In the case of real magnetic materials, both properties are not necessarily accomplished. The fact of a non homogeneous distribution of hysterons as well as the presence of high interactions between them promotes, among others, a dependence of the magnetic susceptibility not only on the magnetic field but rather on the magnetization. The previous statement is a clear example of the congruency property violation. Moreover, the deletion property does not take into account the magnetization dependence on time nor on the rate of the external applied magnetic field. At this point, the non accomplishment of one or both properties does not mean that the model itself is not valid, or it is not applicable, for real magnetic materials. What it really means is that the magnetic behaviour of real materials cannot be reproduced supposing a classical Preisach distribution. In fact, $\rho(H_b, H_r)$ can be modified in order to include the physical

phenomena, with a reasonable mathematical expression responsible of the deviation from the classical model.

4.2 First Order Reversal Curves

The Preisach model, as defined in equation (4.2), is written in the sense that with a given or known hysteron distribution, one is able to predict the magnetization behaviour of a magnetic system. However, in many cases the interest lies in the opposite direction that means to obtain the hysteron distribution from the magnetic response measurement of a magnetic material [Béron 2010]. Within this context, the model can be written in its differential form as follows:

$$\rho(H_b, H_r) = -\frac{\partial}{\partial H_b \partial H_r}\left(\frac{m-1}{2}\right) = -\frac{1}{2}\frac{\partial m}{\partial H_b \partial H_r} \tag{4.3}$$

The negative sign in the equation (4.3) comes from the fact that the different values of H_r traverse in the opposite direction to the H_b ones. In order to see that more precisely, it is necessary to explain the measurement procedure of the so called FORC curves. An example of a typical measurement is shown in *Figure 4.2*. Basically the descendent branch of the major hysteresis loop is traversed stopping at different values of the applied magnetic field (H_r). These field values correspond with the starting point of the first order reversal curves that are recorded increasing the magnetic field (H_b) up to the magnetic saturation, repeating the process for each value of H_r. The measurement procedure points out the interest and the information given by the FORC analysis in a magnetic material. As it was mentioned above, each change in H_r is preceded by the magnetic saturation what means that the magnetic state is restored to a well defined one for each value of H_r.Taking the last lines into account, the lower the H_r the larger the amount of hysterons that are reversed pointing along the negative magnetization axis. Furthermore, the FORC curves show how the different fractions of the hysterons, switched by H_r, go back to positive saturation under different magnetic environments, generated by the hysterons that remain unchanged.

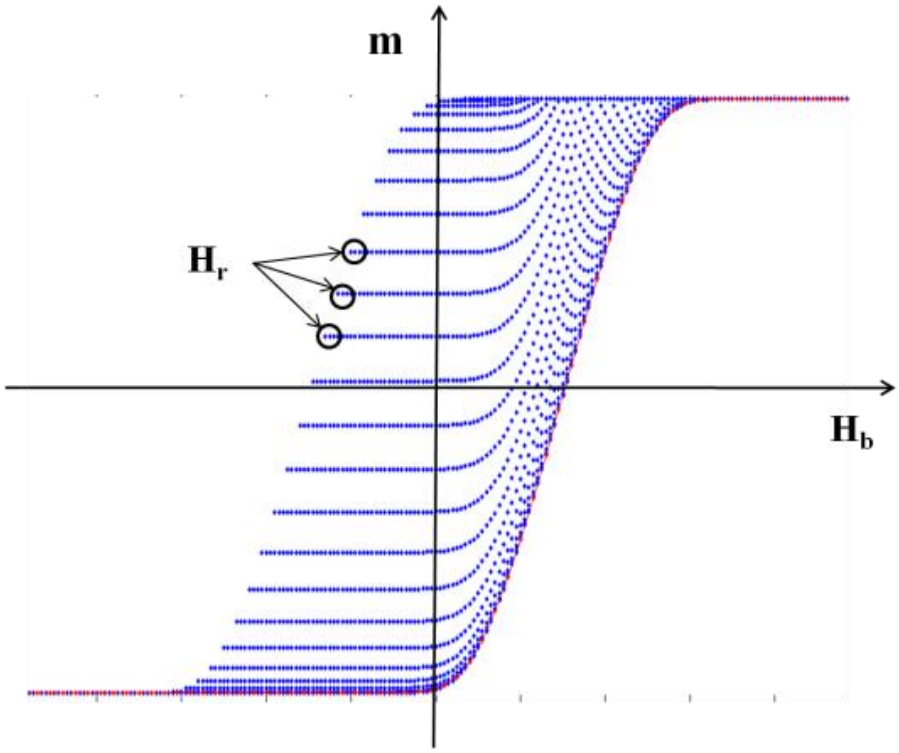

***Figure 4.2**: Typical FORC measurement in blue and the ascendant branch of the major hysteresis loop in red.*

Once the data of FORC measurement is treated through equation (4.3), it is convenient to perform the coordinates change $H_c = (H_b - H_r)/2$ and $H_u = (H_b + H_r)/2$ giving intuitive information about the hysteresis of the hysteron and its asymmetry with respect to the zero magnetic field.

4.3. FORC Simulation from a Statistical Approach

4.3.1. Independent switching fields

In this work, a computational program has been performed in order to generate FORC diagrams from a given distribution of hysteretic processes with the aim to compare them with FORC diagrams measured in real samples. The algorithm has been developed in the computing language of Matlab®. This section will be focused on how the program works and the interpretation of the obtained results will be correlated with a system of magnetic nanowire arrays.

First of all, in many cases an individual nanowire exhibits a bistable hysteresis loop, thus a hysteron can be associated with the magnetization reversal of a single nanowire. Considering a scenario where all nanowires are independent with each other, the reversal of one nanowire can be described by its switching field and saturation magnetization. At the beginning, all nanowires will be considered with the same saturation magnetization, chosen such to be 1 when all nanowires are magnetized along the same direction and sense. Nevertheless, it is possible to define a switching field distribution (SFD), produced by inhomogeities from one nanowire to another as, for instance, small differences in the geometry or composition. What is clear is the fact that these differences in the switching fields are intrinsic to the nanowire and depend exclusively on the physical-chemical properties of it. In order to explain the simulation program, a Gaussian distribution has been chosen to generate the SFD, although this distribution can be replaced by other type of statistical function like the Log-Normal or Lorentzian ones. The expression for a Gaussian or Normal SFD can be written as follows:

$$G(H, H_{SW}) = \frac{1}{\sigma\sqrt{2\pi}} e^{-\frac{(H-H_{SW})^2}{2\sigma^2}} \tag{4.4}$$

where H_{SW} is the mean switching field, σ is the standard deviation and G(H,HSW) accomplishes the normalization condition $\int_{-\infty}^{+\infty} G(H, H_{SW})dH = 1$.

The upper branch of the major hysteresis loop can be calculated, for each value of the applied magnetic field employing the Cumulative Gaussian Distribution (CGD) as the integral of the equation (4.4). Moreover, the switching of a nanowire changes the magnetization in a factor of 2 and the starting magnetization state for the ascendant branch is -1:

$$m_{up}(H) = -1 + 2\int_{-\infty}^{H} G(H, H_{SW})dH = -1 + 2\left[\frac{1}{2}\left(1 + erf\left(\frac{H-H_{SW}}{\sqrt{2\sigma^2}}\right)\right)\right] = erf\left(\frac{H-H_{SW}}{\sqrt{2\sigma^2}}\right) \tag{4.5}$$

Consequently, the descendant branch of the major hysteresis loop can be defined in the same terms:

$$m_{down}(H) = 1 - 2\int_{H}^{+\infty} G(-H, H_{SW})dH = -erf\left(\frac{-H-H_{SW}}{\sqrt{2\sigma^2}}\right) \tag{4.6}$$

Last equations suggest that two different distributions have to be considered depending on the sense of magnetization. Those distributions and therefore the switching

events are symmetric with respect the zero magnetic field in case of non interacting bistable nanowires as can be seen in *Figure 4.3*.

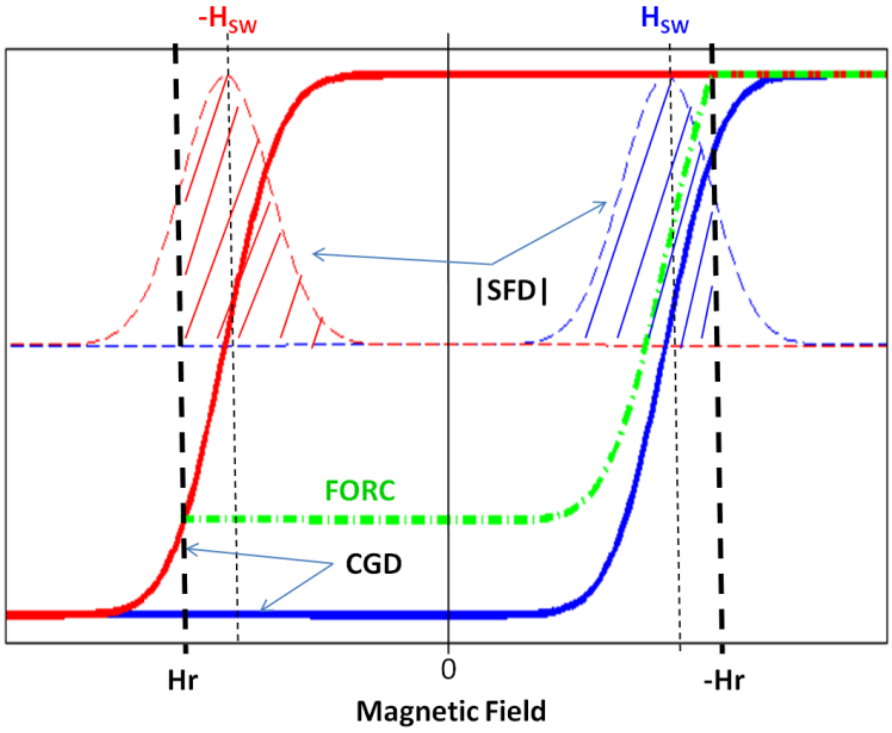

***Figure 4.3**: Major hysteresis loop associated with a switching field distribution. Ascendant branch in blue and descendant one in red. In green an example of FORC is showed starting from a reversal field Hr. The filled regions of SFD denote the amount of magnetic switchings that have been produced by Hr (red), and the part of the distribution that have to be reversed again along the FORC (blue).*

Now the question is how to reproduce the FORCs behavior. First of all, if after saturating the nanowire array, the applied magnetic field is set to H_r, the amount of nanowires that remains unchanged and therefore the reduced magnetization at $H_r \rightarrow m_{Hr}$ is given by equation (4.5). When the magnetic field (H_b) is then increased from this point, the switching events produced by those nanowires that were reversed by H_r have to be added to the ground magnetization (m_{Hr}). Finally, a FORC starting on H_r can be expressed as follows:

$$m(H_b, H_r) = \begin{cases} m_{Hr} + 2\int_{-\infty}^{H_b} G(H, H_{SW})dH & H_b \leq -H_r \\ 1 & H_b \geq H_r \end{cases} \quad (4.7)$$

The first equation is valid for $H_b \leq -H_r$ because of when H_b is equal to $-H_r$, all the nanowires that where switched by H_r are switched back again to positive values and the first equation takes the value of saturation magnetization (m=1). However, the expression (4.7) is not optimized from the computational point of view, thus this equation has to be rewritten using the CGD and the Heaviside function $\theta(x)$ that takes the value 1 when the argument is positive and 0 otherwise:

$$m(H_b, H_r) = \left[m_{Hr} + 1 + \mathrm{erf}\left(\frac{\mathrm{H_b - H_{SW}}}{\sqrt{2\sigma^2}}\right)\right] \cdot \theta(-\mathrm{H_r} - \mathrm{H_b}) + \theta(H_b + H_r) \qquad (4.8)$$

With the previous equation a series of FORCs can be modeled for different values of H_r emulating a real measurement. At this point, it would be possible to evaluate the FORC analysis by applying the equation (4.3) with the magnetization given by (4.8). The result can be seen in *Figure 4.4*. The FORC diagram in *Figure 4.4* a), shows the SFD introduced in equation (4.8), as can also be seen with the profile taken at $H_u = 0$ in *Figure 4.4* c).

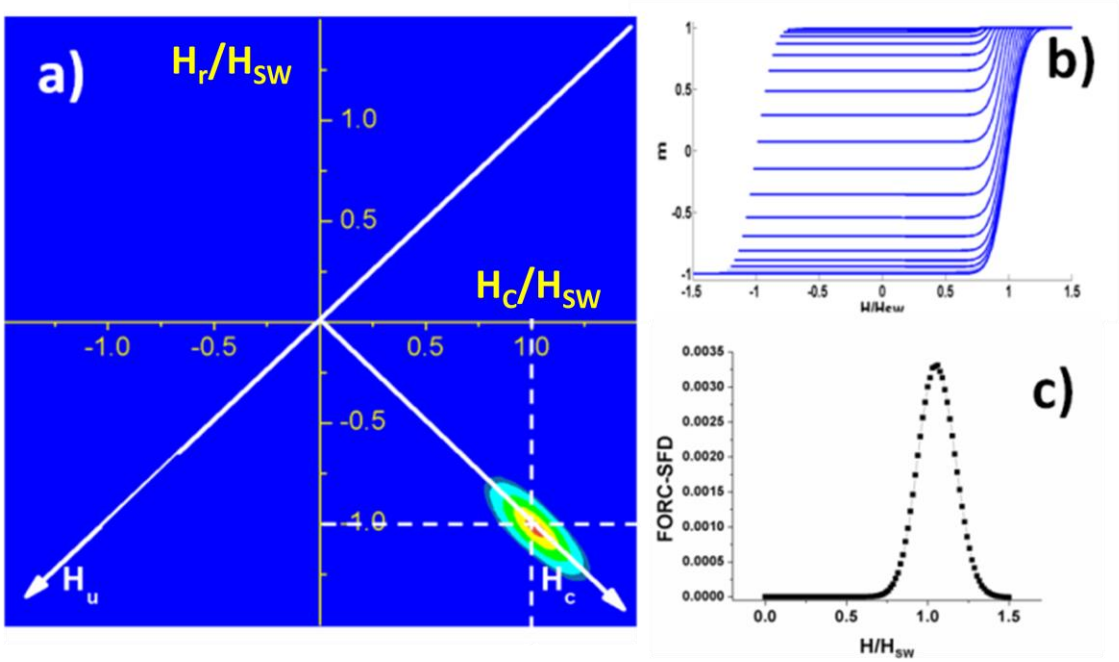

***Figure 4.4**: a) FORC diagram corresponding to the case of not interacting Gaussian distribution of hysterons, extracted from the simulated FORCs in b). The FORC diagram profile at Hu=0 is showed in c) which fits with the simulated distribution.*

4.3.2. MAGNETOSTATIC INTERACTIONS AMONG NANOWIRES IN THE ARRAY

The first deviation from the ideal case when the magnetic nanowires are disposed in an array is that the switching process is not completely independent for each nanowire. In fact, the proximity among nanowires makes that the switching process of one of them is able to modify the overall magnetic field felt by its neighbors. If the switching process is supposed to be homogeneous enough along the array, its effect will be to produce an apparent magnetic field, called mean field interaction (MFI), pointing along the opposite direction with respect to the direction of the magnetization [Wohlfarth 1958, Henkel 1964, Kelly 1989]. In other words, the magnetic field that is felt by the nanowires in the array, which still remains magnetized anti-parallel with respect to the applied magnetic field, is reduced by a factor that depends, among others, on the distance between nanowires and their saturation magnetization [Martínez-Huerta 2012]. Last sentences suggest that this contribution can be added into the above equations through a renormalization of the magnetic field, distinguishing between the applied and the effective magnetic field H_{app} and H_{eff}, respectively, [Richter 2007, Bertotti 1998, Geshev 1997] as:

$$H_{eff} = H_{app} + \alpha m \tag{4.9}$$

It is comprehensible, as a first approximation, to use an expression for the mean field interaction proportional to the reduced magnetization. As it was mentioned above, this field is proportional to the number of nanowires that are pointing along the direction of the magnetization that at the same time is proportional to the reduced magnetization. Since m is the reduced magnetization, the strength of the interaction field is given by α, which takes into account the physical properties of the material. Two different cases can be distinguished in terms of the sign of α. If α is positive, it means that the material presents a positive exchange interaction. On the other hand, being the interesting case the nanowires arrays, the negative interaction of magnetostatic origin among nanowires can be represented by $\alpha < 0$. The interaction field, as can be seen in equation (4.9), has its maximum effect at saturation ($m = 1$) and is zero when the applied magnetic field reaches the coercive field where, in principle, the sample becomes demagnetized and $m = 0$.

The abovementioned is being a point of considerably controversy because, since the approximation to the interaction field depends on the magnetization, the property of congruency is violated. Therefore, on this basis could be the FORC analysis still valid? It is important to take into account that the FORC is always a complementary measurement to the hysteresis loop ones. The problem lies on the fact that what it is not always valid is the interpretation of the FORC analysis as an ideal classical Preisach model. The distribution shown by the FORC would be as classical Preisach distribution modified or distorted by physical phenomena as magnetic interactions, magnetic viscosity, etc. Furthermore, in the FORC analysis the contribution of these phenomena appears, providing more information about the magnetic behavior of the material instead of being a problem. It is then clear that the critical point lies in determining how the Preisach distribution is modified by the different physical phenomena. In principle, the SFD studied in section 4.3.1 would depend exclusively on the intrinsic properties of the nanowire, and not on how they are arranged, what allows to consider it as an intrinsic switching field distribution (ISFD).

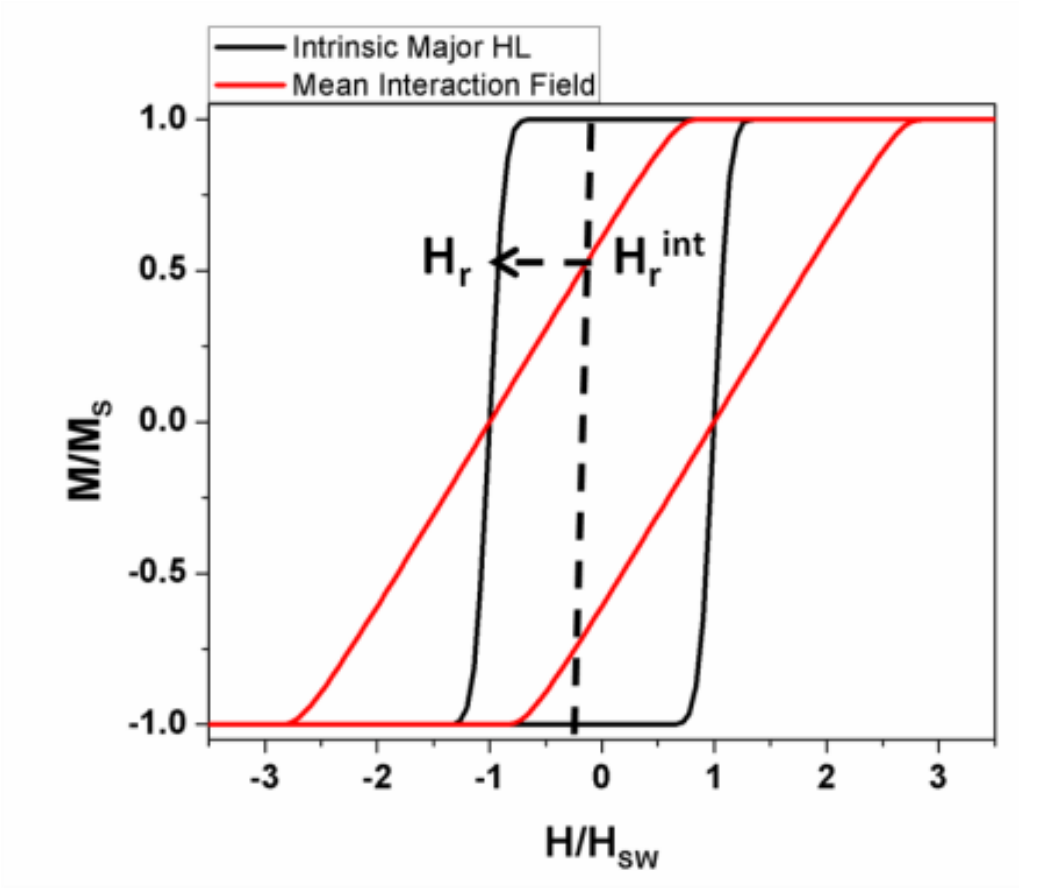

***Figure 4.5**: Simulated intrinsic and interacting major hysteresis loops with* $\boldsymbol{\sigma = H_{SW}/10}$ *and* $\boldsymbol{\alpha = -1.5H_{SW}}$.

The way how the negative mean interaction field modifies the ISFD and, accordingly, the major hysteresis loop is shown in *Figure 4.5*. In principle, the effect of the interaction is just shifting the switching events along the applied magnetic field axis [Béron 2008]. However, the hysteresis itself is not modified because the hysteron is only shifted but its shape remains unchanged. With the previous assumption, neither the hysteresis shape, i.e. the width of the major hysteresis loop, should change under the effect of the mean interaction field.

The procedure to generate the different FORC under a mean interaction field has been chosen as follows. First of all, the intrinsic major hysteresis loop can be calculated from the ISFD. Then, it is possible to obtain the interacting major hysteresis loop through the normalization of the magnetic field using equation (4.9). If the descendant branch of the interacting major hysteresis loop is traversed down to H_r^{int}, then the amount of hysterons that have been switched corresponds to a value of $H_r = H_r^{int} + \alpha m$ in case of non interacting nanowires. Knowing then the intrinsic switching events that take place at H_r^{int}, it is possible to generate the intrinsic FORC and the interacting FORC by means of normalizing the first ones through equation (4.9) for each value of H_r^{int}.

The FORC diagrams calculated for different values of alpha are plotted in *Figure 4.6*. It can be clearly seen that depending on the strength of the MFI with respect ISFD, the FORC diagram is distorted. The cases I) and II) in *Figure 4.6*, can be associated with none- and strong-interacting system respectively, and the interpretation of the FORC diagram is also clear. The case (I) was already explained in section 4.3.1 and case (III) shows a distribution along H_u, which its half width at half maximum is $|\alpha|$. However, in case (II) with comparable ISFD and MFI the FORC diagram shows the so called "wishbone" shape [Pike 2005]. In this case, the distribution that is elongated to higher values of Hc is an artifact of the ISFD modified by the MFI.

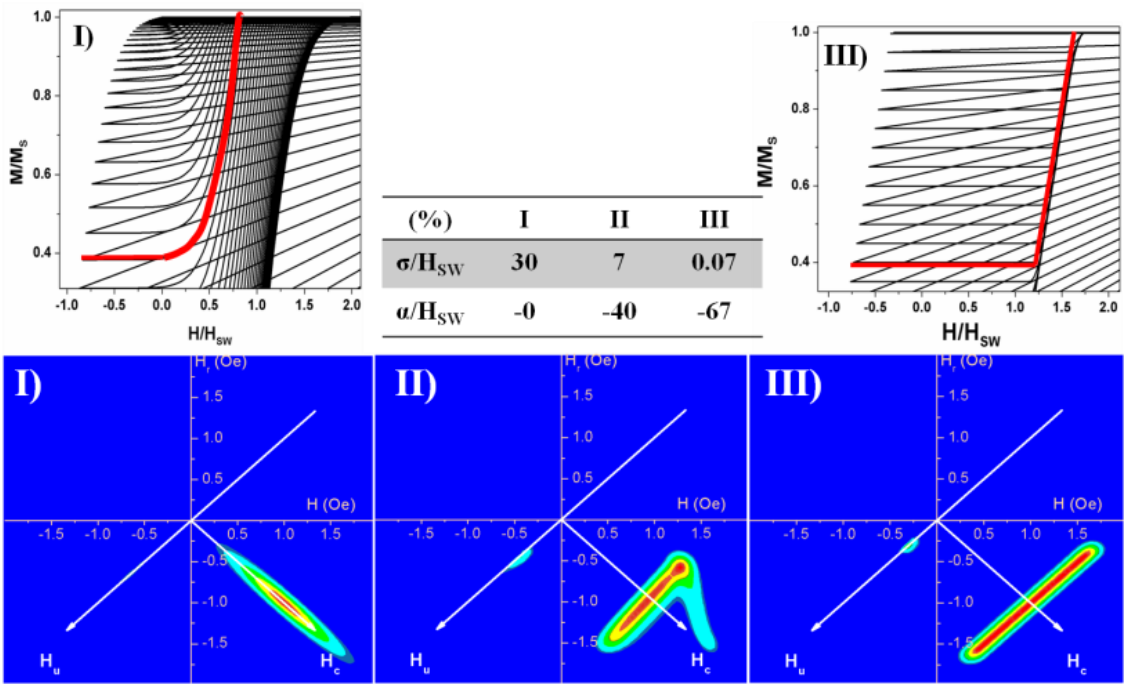

(%)	I	II	III
σ/H_{SW}	30	7	0.07
α/H_{SW}	-0	-40	-67

***Figure 4.6**: FORC diagrams for three different SFD corresponding to the values showed in the table. The examples of generated FORC are also showed for the cases (I) and (III).*

4.3.3. REVERSIBLE MAGNETIZATION PROCESSES IN FORC ANALYSIS

Following the methodology of previous sections, it is necessary to introduce a mathematical expression to take into account magnetic rotation as reversible process. Comparing with the last cases, the reversible magnetization rotation could be expressed as a distribution centered at zero applied magnetic field. This results in a non-hysteretic process that can be added to the previous distributions. Although this approximation works, the absence of physical parameters which are commonly employed to characterized this kind of magnetic behavior and the analytical decoupling with the hysteretic processes, have made interesting to redefine the reversible process of magnetization in terms of the anisotropy field distribution (AFD) [Barandiaran 1989, De La Torre Medina 2009].

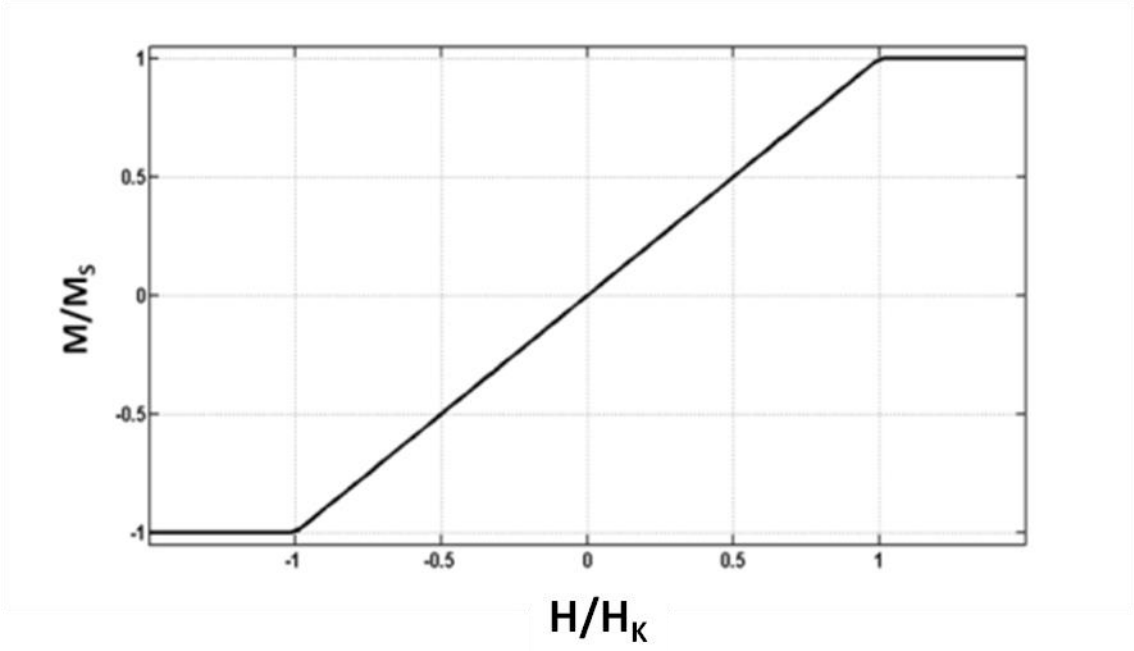

***Figure 4.7**: Reversible magnetization process under the Stoner-Wohlfarth model represented against the applied magnetic field normalized to the anisotropy field (H_K).*

In case of reversible magnetization rotation, as a first approximation, the magnetization exhibits a linear dependence with respect the applied magnetic field up to a certain value at which all the magnetic moments are pointing along the same direction, reaching the saturation magnetization state. This field is commonly called anisotropy field (H_K). In *Figure 4.7* a typical pure reversible hysteresis loop is shown. It is easy then, in this case, to give a linear expression of the magnetization as a function of the anisotropy field of the system:

$$m_{rev}(H) = \frac{1}{H_K} H \cdot \theta(H_K - H) \cdot \theta(H + H_K) + \theta(H - H_K) - \theta(-H_K - H) \quad (4.10)$$

where the Heaviside functions confine the linear dependence in the region between $-H_K$ and H_K.

Nevertheless, for the case of a real magnetic material, the magnetization behaviour is subjected to distribution instead to the absolute values of a parameter. At this point it is possible to distinguish between two different scenarios. First, in many materials the global behaviour cannot be decomposed into completely bistable hysterons. In fact, each hysteron can contribute with a certain proportion of reversible processes via magnetization rotation to the overall magnetic moment [Pike 2003, Béron 2007]. In this sense, it appears reasonable to assume that if the distribution of hysteretic events is

originated from certain inhomogeneities of the sample, the anisotropy field distribution can be correlated with the previous one, which would mean that the standard deviation of both distributions should be the same. On the other cases, the reversible and the irreversible magnetization processes may arise from different magnetic phases or magnetic entities that, in principle, would be independent with no correlation among their distributions. Hereafter, we will focus the following explanations in the first case, by assuming that each nanowire can present a non pure hysteretic magnetization process. Thus it would be possible to define the AFD for a distribution of magnetic nanowires as:

$$G_{AFD}(H, H_K) = \frac{1}{\sigma\sqrt{2\pi}} e^{-\frac{(H-H_K)^2}{2\sigma^2}} \tag{4.11}$$

Following the distribution of equation (4.11), each nanowire has a different H_K, which means that the slope in equation (4.10) is different for each of them. The contribution of reversible magnetization processes to the magnetization reversal from all the nanowires can then be written as:

$$m_{rev}(H) = \int G_{AFD}(H_K) \left[\frac{1}{H_K} H \cdot \theta(H_K - H) \cdot \theta(H + H_K) + \theta(H - H_K) - \theta(-H_K - H)\right] dH_K \tag{4.12}$$

Once the reversible component is calculated, the total magnetization of the magnetic material can be expressed as a sum of their reversible and irreversible contributions:

$$m(H, H_r) = \mu \cdot m_{irr}(H, H_r) + (1 - \mu) \cdot m_{rev}(H) \tag{4.13}$$

where μ is the proportionality factor between reversible an irreversible processes. The major hysteresis loop as well as the FORC diagram for different values of μ, are plotted in *Figure 4.8*. The main result extracted from those diagrams is that the rotation, at least in case of non interacting system, does not modify the ISFD but just only adding a negative and positive distribution along the H_u axis.

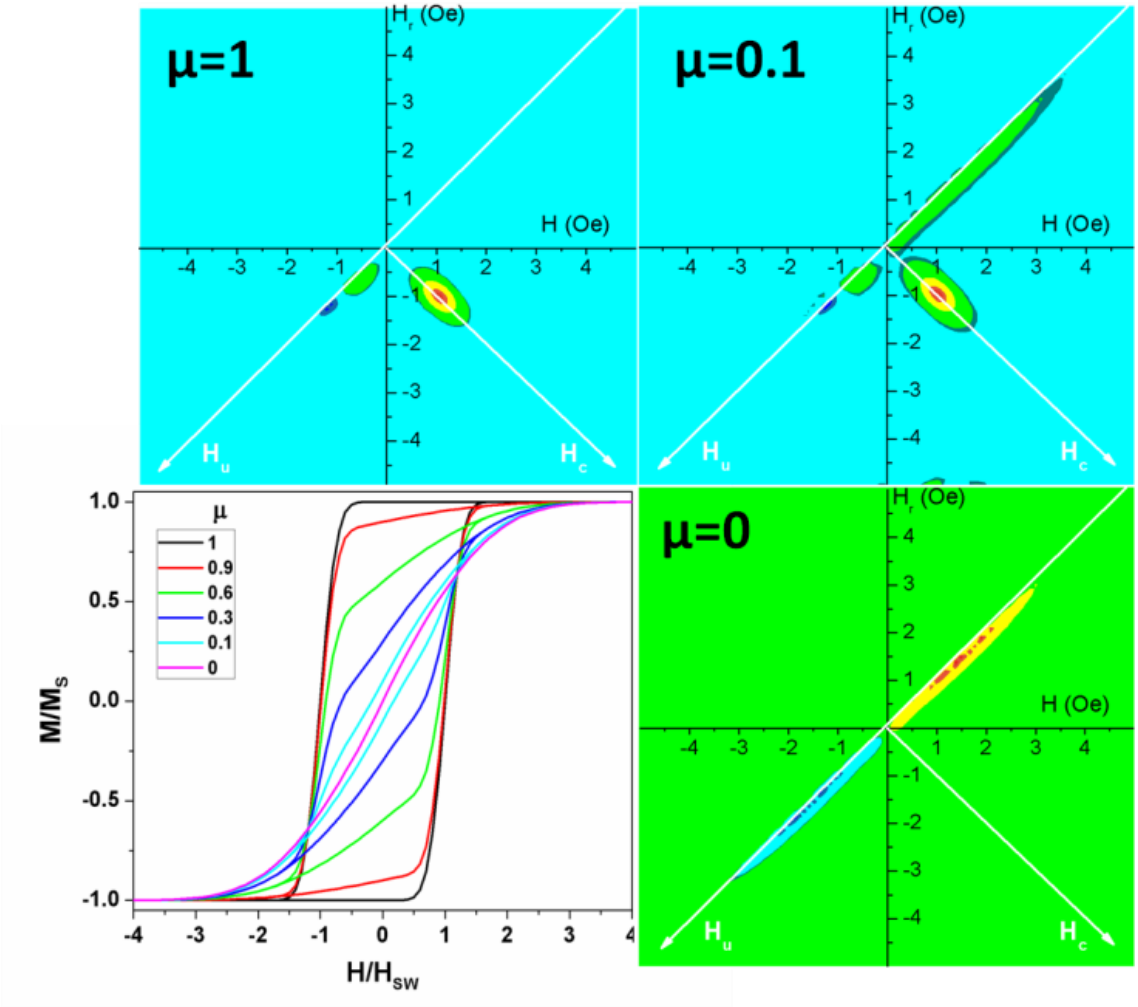

***Figure 4.8**: Major hysteresis loops and FORC diagrams for different proportionalities of the reversible component. The parameters of the hysteron distribution are* $\boldsymbol{H_K = 2H_{SW}}$, $\boldsymbol{\sigma_{ISFD} = 0.2H_{SW}}$ *and* $\boldsymbol{\sigma_{AFD} = 0.8H_K}$.

4.3.4. NON HOMOGENEOUS ISFD

In some magnetic materials, and more specifically, some types of nanowire arrays, it may be the case that more than one magnetic phase can be intrinsically present. For that reason, it is interesting to see how the FORC analysis works with more than one ISFD and if it is possible, to extract information about the interactions among them. Firstly, we will define an ISFD composed by two different, and in principle Gaussian, distributions $G(H, H_{SW1}, H_{SW2})$. In the case of non interacting nanowires, the FORC can be calculated by means of the same methodology as in section 4.3.1, substituting $G(H, H_{SW})$ by $G(H, H_{SW1}, H_{SW2})$. If we consider that the magnetic volume of both distributions is different:

$$m(H) = \varphi \cdot m(H, H_{SW1}) + (1 - \varphi) \cdot m(H, H_{SW2}) \qquad (4.15)$$

where φ defines the proportion between the two different distributions. By direct substitution of equation (4.8) in equation (4.15) for each distribution, the magnetization can be written as:

$$m(H) = \left[m_{Hr} + \varphi \cdot \left[1 + erf\left(\frac{H_b - H_{SW1}}{\sqrt{2\sigma_1^2}} \right) \right] + (1-\varphi) \cdot \left[1 + erf\left(\frac{H_b - H_{SW2}}{\sqrt{2\sigma_2^2}} \right) \right] \right] \cdot$$

$$\cdot \theta(-\mathrm{H_r} - \mathrm{H_b}) + \theta(H_b + H_r) \qquad (4.16)$$

where $m_{Hr} = \varphi \cdot m_{1,Hr} + (1-\varphi) \cdot m_{2,Hr}$.

An example of a major hysteresis loop, as well as two FORC, performed for the case of two distributions centered at H_{SW1} and H_{SW2}, respectively, are shown in *Figure 4.9*. Starting from negative saturation, and increasing the applied magnetic field value, the first distribution with lower switching field, in this case H_{SW1}, makes to increase the magnetization. If both distributions are well separated from each other, after the first switching, there is a plateau up to the field value corresponding to the one at which the second switching field distribution starts to increase the magnetization. In order to better explain how the FORC should work in those kinds of systems, it is enough to explain two different cases.

First of all, if after the positive saturation of the material, the magnetic field is reduced down to H_{r1}, only a fraction of nanowires of the distribution $G(H, H_{SW1})$ has been reversed. If H is increased again, the same portion of the distribution will switch at its specific value in the distribution $G(H, H_{SW1})$. On the other hand, if the reversal field is set to H_{r2} after saturation, the whole distribution referred to H_{SW1} will be reversed and a portion of the second or magnetically harder distribution is reversed. Increasing the magnetic field, $G(H, H_{SW1})$ will switch first and the positive magnetic saturation will not be achieved until the remaining portion of $G(H, H_{SW2})$ switches completely.

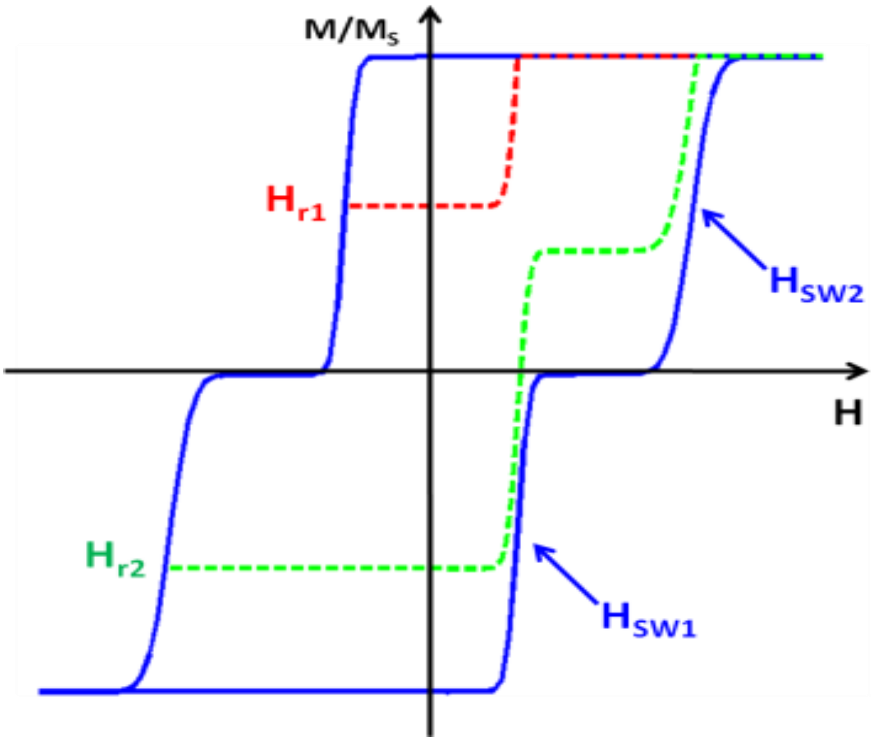

***Figure 4.9**: Major hysteresis loop and two FORC of non interacting two Gaussian distributions centered at $\boldsymbol{H_{SW1}}$ and $\boldsymbol{H_{SW2}}$, with standard deviations $\boldsymbol{\sigma_2 = 2\sigma_1}$ and proportion factor $\boldsymbol{\varphi = 0.5}$.*

More interesting that the case of MFI in the actual non homogeneous ISFD, is the possible influence of an interaction between the two magnetic phases, instead of the interaction among nanowires of the same distribution. A new magnetic scenario can be proposed, assuming that the presence of a hard magnetic phase (H_{SW2}) affects the switching field of a soft one (H_{SW1}). The effect of this interaction would shift the whole soft distribution along the axis of the applied magnetic field. In *Figure 4.10*, a factor of interaction has been introduced to the ISFD of the previous case, and in order to facilitate the explanation we will suppose the magnetic system shown in *Figure 4.10*, b). In this system the antiparallel configuration between the two different magnetic phases is supposed to be energetically favorable and the soft magnetic phase the one which is dependent on the magnetic state of the hard magnetic phase. Keeping the same definition of H_{SW1}, what it is modified is the FORC related to this distribution by a factor of ΔH, which at the same time introduce an asymmetry with respect the magnetic field. It is then clear that the intrinsic switching field of the soft magnetic phase is now $H_{SW(soft)} = H_{SW1} + \Delta H/2$. Starting from positive magnetic saturation, the magnetic field is reduced down to H_{r1}. In this case of antiparallel interactions and strong influence of the hard magnetic phase, the switching of the soft distribution is carried out at lower fields than its

intrinsic switching field due to the antiparallel configuration is favored by the negative interaction. Similarly, if at H_{r1} the applied field is increased, the switching of the soft phase will take place at higher values of its intrinsic switching field due to the switching of the soft magnetic phase to the parallel configuration is retained by the hard phase. However, if the reversal field is set to H_{r1} the whole soft magnetic phase will be pointing towards the negative saturation. In turn, a portion of the hard magnetic phase will be also pointing along the same direction as the soft one. Increasing the magnetic field from H_{r2} to positive saturation, it is possible to distinguish three different events. The first of them is related to the portion of the hard magnetic phase that has been switched. In this case, the soft magnetic phase related to the hard magnetic phase that has been switched will be in a parallel state so it will reversed its magnetization before $H_{SW(soft)}$, and more precisely at H_{SW1}. After this point, there is still a portion of the soft magnetic phase that remains in an antiparallel configuration with respect the hard one. As it was mentioned above, this part of the material will reverse its magnetization at $H_{SW1} + \Delta H$. Finally, the amount of switching events produced on the hard magnetic phase at H_{r2} has to reverse their magnetization when the applied magnetic field reaches H_{SW2} that, in fact, is the intrinsic switching field of the hard magnetic field.

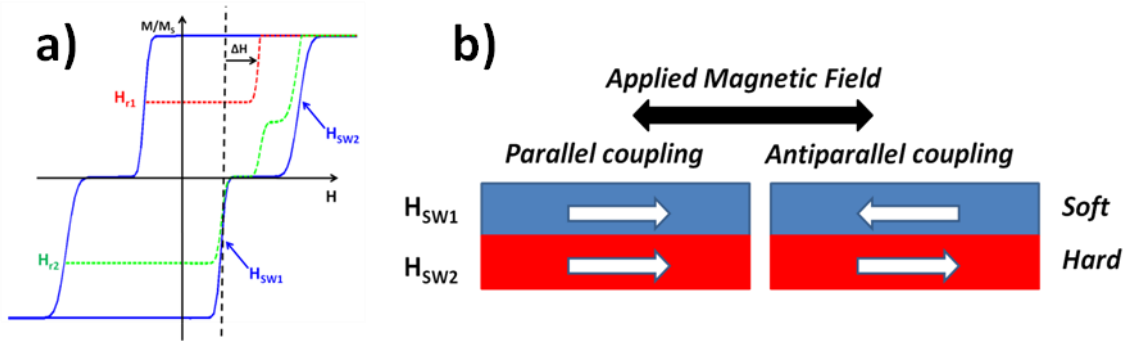

***Figure 4.10**: a) Major hysteresis loop and two FORCs of the same ISFD as in Figure 4.9, modified by interaction between the two phases. b) Example of magnetic system that can follow the magnetic behavior presented in a).*

In order to study how the previous magnetic interaction modifies or affects the FORC diagram, it becomes necessary to express its magnetic behavior in mathematical terms. In order to reduce the length of the mathematical expressions, we further consider $f(H_b, H_{SWi}) = \left[1 + erf\left(\frac{H_b - H_{SWi}}{\sqrt{2\sigma_i^2}}\right)\right]$ where i refers to the distribution 1 or 2. Then the magnetization can be written as:

$$m(H_b, H_r) =$$

$$= \overbrace{\left\{ m_{Hr} + \varphi \cdot f(H_b, H_{SW1}) \cdot \frac{f(-H_r, H_{SW2})}{2} + (1-\varphi) \cdot f(H_b, H_{SW2}) \right\}}^{I} \cdot \theta(-H_r - H_b) +$$

$$+ \left\{ \overbrace{\varphi \cdot f(H_b, H_{SW1} + \Delta H) \cdot \left(1 - \frac{f(-H_r, H_{SW2})}{2}\right)}^{II} + \right.$$

$$\left. + \overbrace{\left[m_{Hr} + \varphi \cdot f(-H_r, H_{SW1}) \cdot \frac{f(-H_r, H_{SW2})}{2} + (1-\varphi) \cdot \quad f(-H_r, H_{SW2}) \right] \cdot \theta(H_r + H_b)}^{III} \right\} \cdot$$

$$\cdot \overbrace{\theta(-H_r + \Delta H - H_b)}^{(II,III)} + \overbrace{\theta\big(H_b - (-H_r + \Delta H)\big)}^{IV} \qquad (4.17)$$

One important term in equation (4.17) is $\frac{f(-H_r, H_{SW2})}{2}$ that denotes the amount of hard magnetic switching produced by the effect of H_r. If that distribution is completely switched, i.e., H_r is set to negative saturation, the value of the previous term is 1. The first term in equation (4.17) is the responsible of the reversal at H_{SW1}, characteristic of the parallel coupling between the two magnetic phases. The factor (II), takes into account the part of the soft distribution that is antiparallel coupled with the hard one and has not been switched by H_r. Then this distribution is apparently shifted by a factor of ΔH, contributing to the overall magnetization up to $(-H_r + \Delta H) = H_b$ controlled by $\theta(-H_r + \Delta H - H_b)$. On the other hand, the factor (III), is the value of magnetization of the term (I) at $H_b = -H_r$, so it corresponds to the limit at which the distribution followed by the first term is completely reversed again, resulting in the plateau between $-H_r$ and $-H_r + \Delta H$.

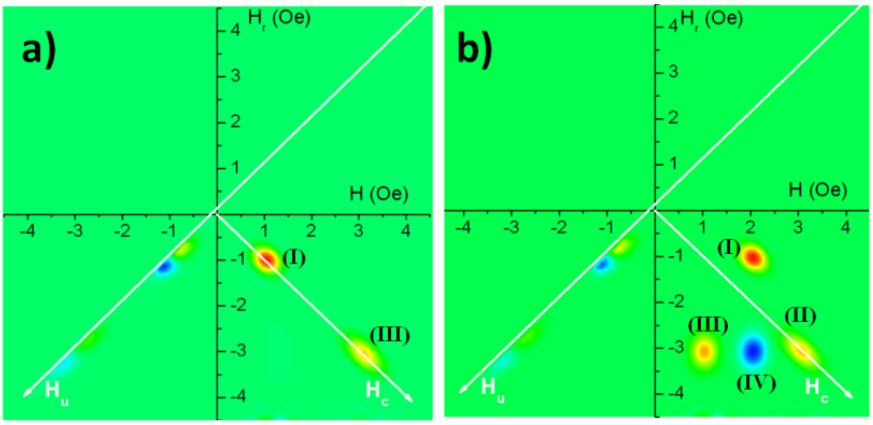

***Figure 4.11**: FORC diagrams of not interacting a) and interacting b) distributions related to Figure 4.9 and Figure 4.10 respectively. More precisely, $\boldsymbol{H_{SW2} = 3H_{SW1}}$ and $\boldsymbol{\Delta H = 2H_{SW1}}$.*

The FORC diagrams for the cases of not interacting and interacting magnetically soft and hard distributions are shown in *Figure 4.11*, a) and b), respectively. The FORC diagram for the case of not interacting SFD displays the two distributions centered at their respective H_{SW} values, without any component on the H_U axis. On the other hand, when $\Delta H \neq 0$, the FORC diagram becomes more complicated. In this diagram four different distributions can be clearly distinguished, (I) along the $H_r = -H_{SW1}$ and (II, III, IV) along $H_r = -H_{SW2}$. The above mentioned, suggest that the first distribution comes from the FORC when H_r only reverses the soft phase. In contrast, (II, III, IV) refer to FORC made when some part of the hard phase is switched at H_r. Comparing directly with Figure 4.10 a), it is possible to associate (III) with the switching at H_{SW1}, (IV) at $H_{SW1} + \Delta H$ and (II) at H_{SW2}. The negative sign of the distribution (IV) comes from the factor $1 - \frac{f(-H_r, H_{SW2})}{2}$ in the second term of equation (4.17). This sign appears with the reversal of the magnetically hard distribution, which can also be associated with the fact that the effect of the reversal of the hard phase at H_r is to reduce the switchings at $H_{SW1} + \Delta H$. The specific coordinates of each distribution are collected in *Table 4.1*. As it can be seen, the positions of the distributions also describe the non interacting state. If $\Delta H = 0$, then (I) and (II) would appear centered at $(H_{SW1}, 0)$ and $(H_{SW2}, 0)$, respectively. Moreover, (III) and (IV) would collapse at the same point annihilating between them due to their different sign, providing the FORC diagram shown in Figure 4.11, a).

FORC distribution	H_C	H_U
(I)	$H_{SW1} + \frac{\Delta H}{2} = H_{SW(soft)}$	$\frac{\Delta H}{2}$
(II)	H_{SW2}	0
(III)	$\frac{H_{SW1} + H_{SW2}}{2}$	$\frac{H_{SW1} - H_{SW2}}{2}$
(IV)	$\frac{(H_{SW1} + \Delta H) + H_{SW2}}{2}$	$\frac{(H_{SW1} + \Delta H) - H_{SW2}}{2}$

***Table 4.1**: Coordinates of FORC distributions related to the case showed in Figure 4.11, b).*

On the other hand, another interesting behavior occurs when ΔH is such that the distribution referred to H_{SW1} switches at H_{SW2} when the FORCs start at $H_r < H_{SW2}$, i.e., $\Delta H = H_{SW2} - H_{SW1}$. The FORC diagram of this specific behavior is shown in *Figure 4.12*. In this case, (I) and (III) will be symmetric with respect the H_C axis and located at $(H_C, H_U) = \left(\frac{H_{SW1}+H_{SW2}}{2}, \frac{H_{SW2}-H_{SW1}}{2}\right)$ and $\left(\frac{H_{SW1}+H_{SW2}}{2}, -\frac{H_{SW2}-H_{SW1}}{2}\right)$ respectively. In turn, the distribution (IV) is shifted to $(H_{SW2}, 0)$, collapsing with (II). However, (IV) does

not annihilate (II) because both distributions are elongated perpendicularly between them. The previous fact causes a "butterfly" shape in the FORC diagram which is characteristic of this kind of behavior [Pike 1999].

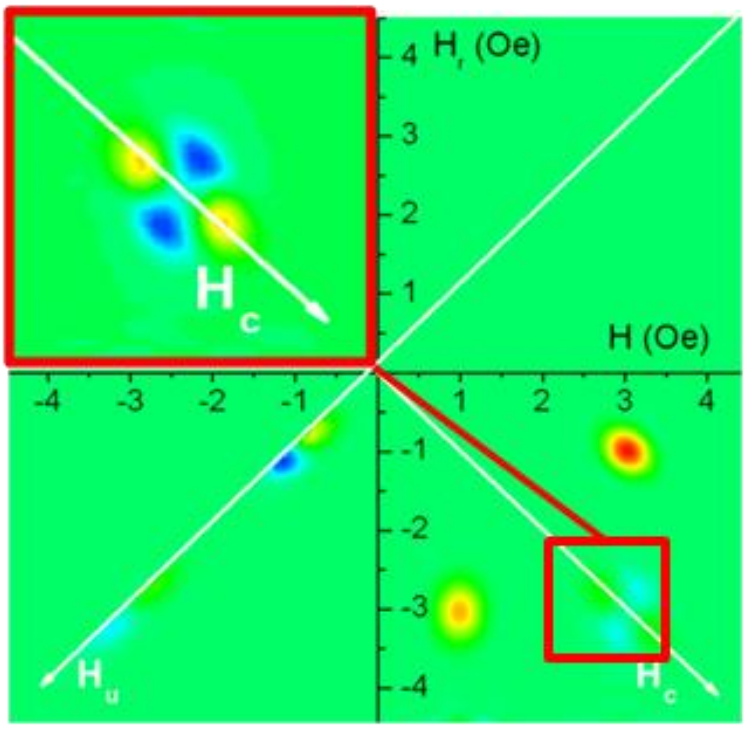

Figure 4.12: *FORC diagram in case of* $\Delta \boldsymbol{H} = \boldsymbol{H_{SW2}} - \boldsymbol{H_{SW1}}$. *The inset shows the detailed region where the "butterfly" structure appears indicated by the square.*

4.4 EXCHANGE COUPLING BETWEEN FERROMAGNETIC PHASES

In order to study the global behavior of a magnetic system composed by two different magnetic phases coupled by exchange, the following experiment has been proposed. Porous anodic alumina membranes (PAAM), anodized in 0.3M oxalic acid under standard conditions, have been employed. After opening the barrier layer, the mean pore diameter has been found to be 42 nm and the interpore distance of 105 nm has not been modified during the process. The studied nanowire array was prepared by a first electrodeposition of pure Ni long nanowires and a subsequent electrodeposition of pure Co long nanowires. A schematic image of such nanowire array can be found in *Figure 4.13* a). In order to compare the effect of the coupling between the two nanowires with different composition, arrays with only Ni or Co nanowires have been fabricated as a reference of each nanowires composition. The electrodeposition of Co and Ni nanowires was carried out by means of the Watts type electrolyte: 300g/l$CoSO_4 \cdot 7H_2O$+ 45g/l$CoCl_2 \cdot 6H2O$+ 45g/lH_3BO_3 and 300g/l $NiSO_4 \cdot 6H_2O$+45g/l $NiCl_2 \cdot 6H2O$+45g/l H_3BO_3, respectively. The temperature of the electrolytes was kept at 45ºC during the

electrodeposition to avoid boric acid precipitation. Co and Ni nanowires were electrodeposited at -1V and -1.2V vs. an Ag/AgCl reference electrode, respectively, for 10 minutes in both cases. *Figure 4.13* b) shows an EDX linescan made on the bimagnetic nanowire array pointing out the part of Ni nanowire and the corresponding to the Co one. The length of the Co and Ni segment is around 16 µm and 20 µm respectively thus the high aspect ratio is assured.

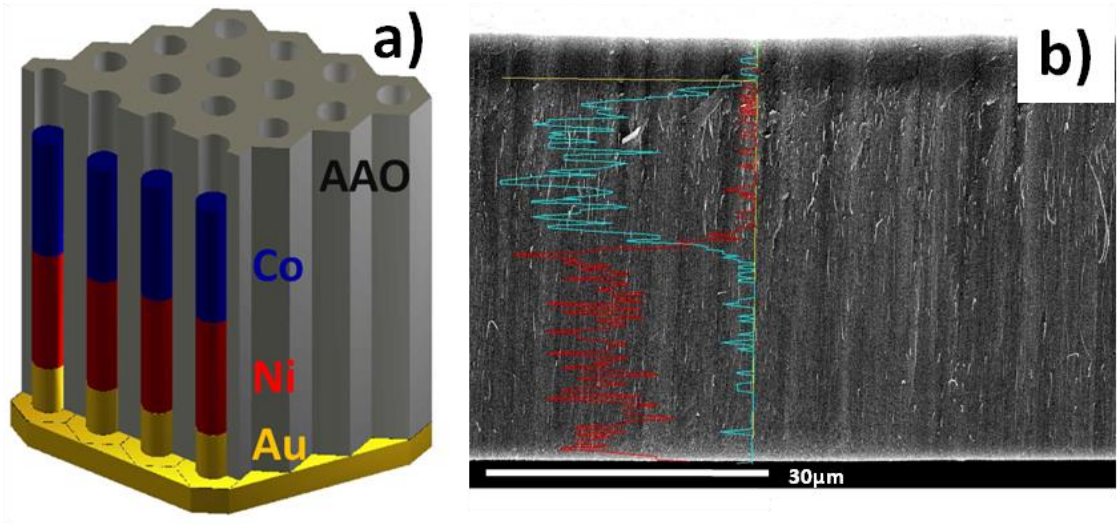

***Figure 4.13**: a) Cross section schematic draw of the studied sample of Ni(red)/Co(blue) exchange coupled nanowires array. b) EDX linescan made on the cross section of sampled schematized in a) where the signal provided by Ni and Co is represented in red and blue respectively.*

In order to study the effect of the coupling into nanowires on the magnetic properties, first of all it is necessary to characterize each kind of nanowire array separately. In *Figure 4.14* the room temperature parallel HL of Ni and Co nanowire arrays are compared. The main difference between both nanowire arrays lies on the coercive field which is larger in case of pure Co ($H_c^{Co} = 1296\ Oe$) than pure Ni ($H_c^{Ni} = 884\ Oe$) nanowire array. In both cases the HL width is constant between negative and positive saturation magnetization states, guaranteeing the bistability of the switching processes that take place along the magnetization easy axis which lies along the parallel direction with respect to the nanowires axis. In addition, the HL of Co nanowire array is more tilted towards the magnetic field axis which is characteristic of stronger magnetostatic interactions between nanowires. Since the geometrical characteristics of the arrays are the same in both kinds of samples, such a difference on the interaction between nanowires is ascribed to the different saturation magnetization of Ni and Co, being higher in the last case.

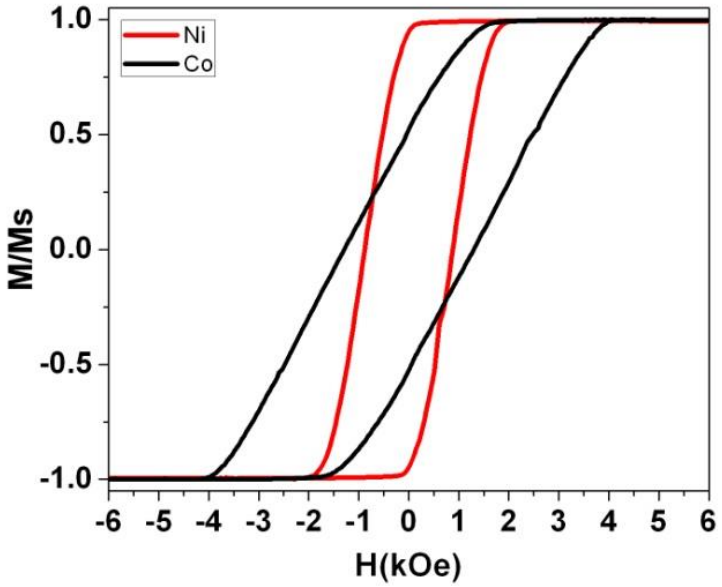

***Figure 4.14**: Room temperature hysteresis loops measured along the nanowires axis in Ni (red) and Co (black) nanowire arrays.*

In order to extract the intrinsic SFD of the Co and Ni nanowire arrays and evaluate the magnetostatic interaction between nanowires, FORC analysis has been performed on these samples. The FORC diagrams of both samples are presented in *Figure 4.15*. In principle, the FORC distribution of both nanowire arrays resembles to the "wishbone" shape explained in a previous section, however some differences can be observed. First of all, in case of the Co nanowire array the FORC distribution is bent to lower values of Hc when Hu is positive. Such behavior has not been ascribed to an asymmetry of the SFD, but instead to an inhomogeneity of the mean field interaction. As it was discussed in section 4.3.2., under the MFI theory, the magnetostatic interaction between nanowires is proportional to the magnetization. This means that at the coercive field, where the net magnetization is 0, the magnetostatic interaction strength should be also zero. However, the characteristic arrangement of nanowires in case of PAAM templates can play an important role in how the nanowires interact near the coercive field of the system. This inhomogeneity can be taken into account by adding a second term to the MFI as follows [Che 1992, Huerta 2012]:

$$H_{eff} = H_{app} + \alpha m + \beta(1 - m^2) \qquad (4.18)$$

In *Figure 4.15* the effect of β on simulated FORC distributions can be observed, which fixes well with the experimental FORC distribution in the specific case of Co

nanowire arrays. Nevertheless, the experimental diagram showed by the Ni nanowire array cannot be explained or reproduced by the addition of the previous interaction parameter β. Even though such diagram could correspond to the presence of a second harder SFD which would not be interacting, it is hardly understood the presence of such different switching fields up to 2000 Oe while the main distribution is around 900 Oe. Furthermore, both crystalline structure and morphology of the electrodeposited Ni nanowires are very homogeneous which would reduce the probability to find different phases with such a difference in their switching fields [Proenca 2012]. It is worth checking then if the interaction between nanowires can be the responsible of the high coercivity distribution. In this contest, the shape of the FORC diagram of Ni nanowire array can be assumed as a "wishbone" shape that is in fact distorted by a none linear dependence of the interaction with respect the reduced magnetization. Nevertheless, comparing the FORC diagrams of Ni and Co nanowire arrays, it is evidenced again the stronger magnetostatic interaction between Co nanowires due to the elongation along the Hu axis where the value of the MFI at saturation (α) is around 2000 Oe and 800 Oe for Co and Ni nanowire arrays, respectively.

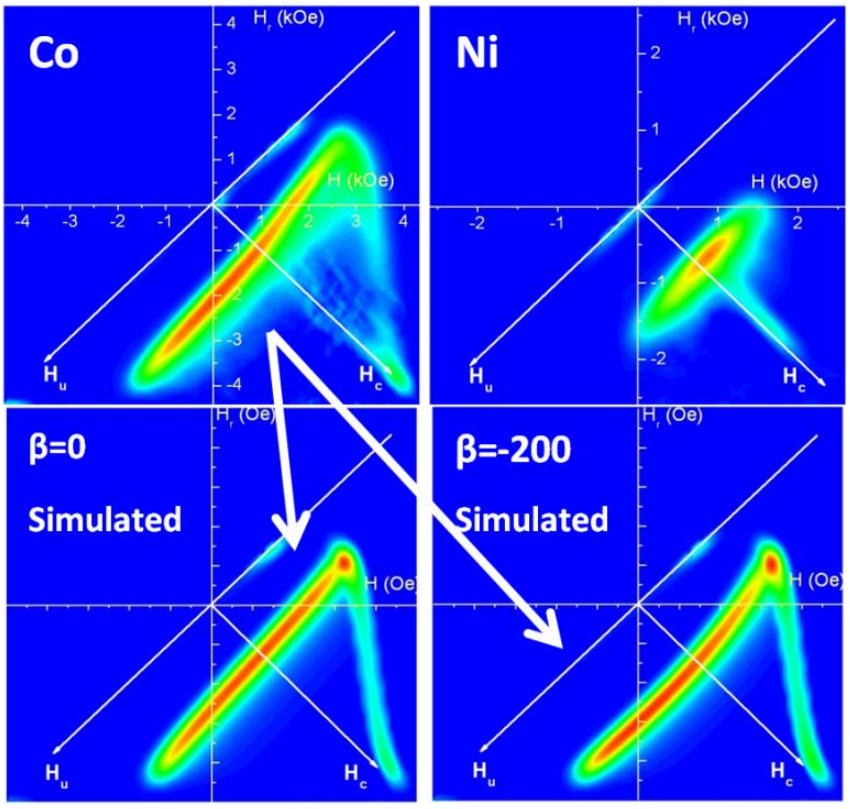

***Figure 4.15**: (top) Experimental FORC diagrams of Co (left) and Ni (right) nanowire arrays measured along the nanowires axis. (bottom) Simulated FORC diagrams with fixed values of Hsw and α, for β=0 Oe (left) and β=-200 Oe (right).*

Although the last measurements would be sufficient for the comparison with the bimagnetic Ni/Co nanowire arrays, an array of Co nanowires plus an array of Ni nanowires were stacked and measured together in order to reproduce a non interacting bimagnetic system where Ni and Co nanowires are not in contact. Hereafter this sample will be referred to us as Ni+Co to avoid any confusion with the Ni/Co nanowire array. The HLs of each sample measured along the magnetization easy axis are plotted in *Figure 4.16*. In *Figure 4.16* a), HLs of Ni and Co nanowire arrays are compared with the non interacting Ni+Co nanowire array. As it was expected, the resulting magnetic behavior of Ni+Co sample is the sum of the independent HLs of Ni and Co nanowires. If we have a look at the descendant branches of the HLs, it is possible to distinguish the contribution of each kind of nanowire. First, as the magnetic field is reduced in the Ni+Co sample the magnetization drops down to the same value as the Co nanowire array does. Further decrease of the magnetic field provokes a second drop of the magnetization corresponding to the switching of Ni nanowires. On the other hand, the Ni/Co nanowire array shows a more complex behavior suggesting that the switching of one of the nanowire affects the other one coupled by exchange at the interface.

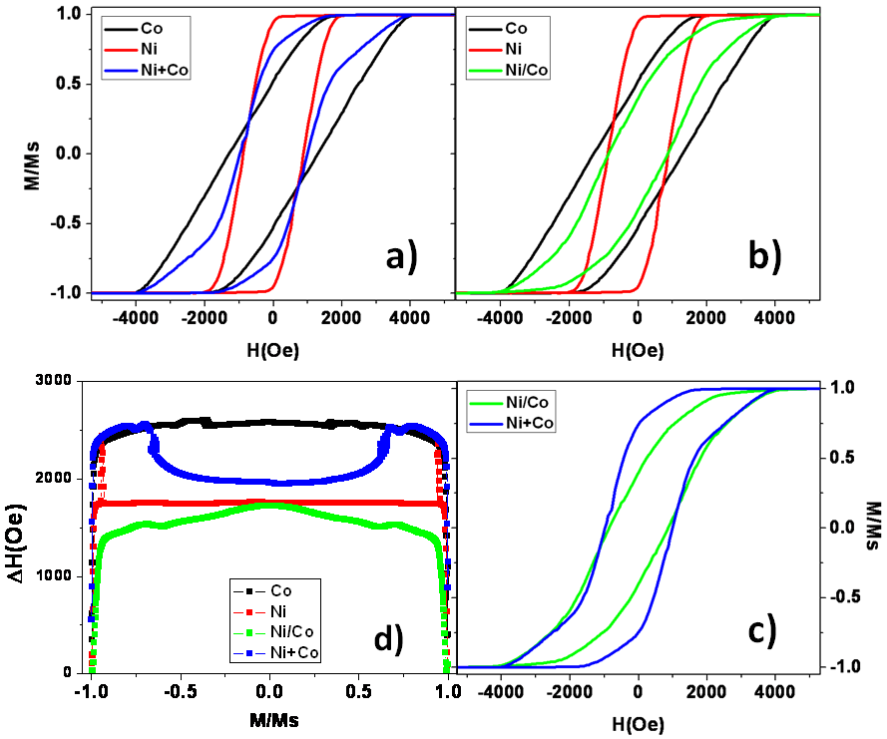

***Figure 4.16**: Comparison of room temperature hysteresis loops measured along the nanowires axis among Ni, Co and Ni+Co a); Ni, Co and Ni/Co b); Ni+Co and Ni/Co c). In d) the comparison of the hysteresis shape extracted from previous HLs for all samples is presented.*

The comparison of the Ni/Co HL with respect the Ni and Co nanowire arrays can be seen in *Figure 4.16* b) whilst it is compared with the Ni+Co one in *Figure 4.16* c). The differences with respect the non interacting Ni+Co nanowire array are clearly evidenced. If we left the positive saturation magnetization through the descendant branch of the Ni/Co HL, the switching fields start earlier than in case of Ni+Co and therefore before the Co first and the Ni afterwards. In principle, the magnetization process seems to be driven by the softer magnetic phase since the overall hysteresis is reduced as can be seen in *Figure 4.16* d). Furthermore, in case of the Ni+Co sample, the hysteresis of each composition is clearly evidenced while in case of Ni/Co nanowire array such differences are removed and the overall magnetic hysteresis is close to that shown by the Ni nanowire array. In summary, the hysteresis and the tilt of the Ni/Co HL resemble to the equivalent switching of a Ni nanowire array with the MFI strength presented by the Co one.

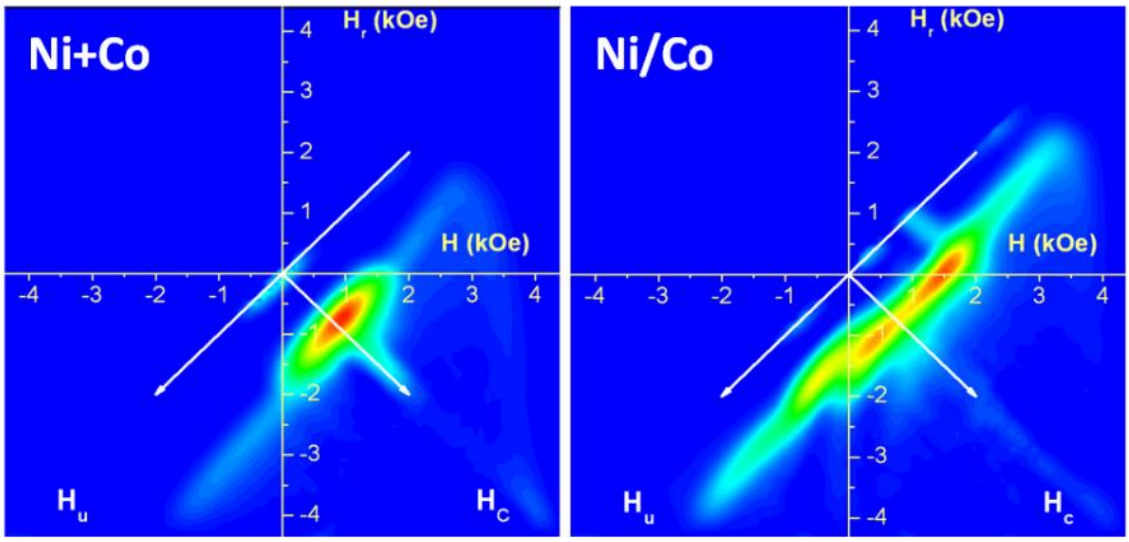

***Figure 4.17**: FORC diagrams measured along the magnetization easy axis in Ni+Co (left) and Ni/Co (right) nanowire arrays.*

In order to complete the magnetic characterization of such interacting nanowire array, FORC have been also compared. The FORC diagram of Ni+Co nanowire array is exactly what is expected since it corresponds to the sum of the individual FORC diagrams of Ni and Co nanowire arrays, as can be seen in *Figure 4.17*. However, the differences between the Ni/Co FORC diagram and the previous one point out that some additional effect must be taken into account. As the unique difference between the Ni/Co and Ni+Co nanowire arrays lies on the fact that the nanowires are in contact, it is reasonable to think that the exchange coupling at the interface is the responsible of such a complex FORC distribution.

Let us consider the magnetization reversal process of one of the Ni/Co bi-magnetic nanowire as it is represented in *Figure 4.18*. In addition, we will represent the intrinsic switching field of Ni and Co as H_{SW1} and H_{SW2} respectively, where $H_{SW1} < H_{SW2}$ as it was reflected by the HLs of Ni and Co nanowire arrays. In principle, if we reduce the applied magnetic field from saturation the Ni segment of the nanowire should reverse its magnetization first and more precisely at H_{SW1} (see the non-interacting case in *Figure 4.18* a)). However at this point, the respective moments of Ni and Co at the interface would be confronted which would not be a stable magnetic configuration. Furthermore, it is reasonable to think that the system would attempt to avoid such configuration, being able to accomplish it via two different ways. First, the reversal magnetization process produced in Ni segment could be propagated through the Co one provoking its magnetic reversal before its intrinsic switching field (see the case (I) in *Figure 4.18* b)). This case would result in a one step magnetization reversal of the Ni/Co nanowire driven by the magnetically softer phase, i.e., Ni segment in this case. Moreover, if the two segmented nanowire behaves like a homogeneous one [Navas 2012], the saturation magnetization of the equivalent nanowire would be an average between the separated nanowires which would result in a different apparent mean interaction field. More precisely, the switching field of the bi-segmented nanowire would be close to one presented by Ni segment, while the mean interaction field would be increased by the Co segment since Co presents higher saturation magnetization. On the other hand, if H_{SW1} and H_{SW2} are different enough, it is possible that the magnetization reversal cannot be carried out in one step. In this case, after the switching of the Ni segment the system would remain in the antiparallel configuration until the switching of the Co segment. As Ni and Co segments are exchange coupled, the presence of Co one could retain the switching of the Ni segment increasing H_{SW1} which would depend on the strength of the coupling (see case (II) in *Figure 4.18* c)). Taking into account what was mentioned in section 4.3.4, the FORC diagram of *Figure 4.17* b) suggests that the FORC behavior is different with respect the uncoupled case. If after magnetization saturation the applied magnetic field is reduced down to the switching of the Ni segment in order to start the FORC from the antiparallel configuration, the minor hysteresis loop would not back to saturation through H_{SW1} (red FORC in *Figure 4.18* c)) due to the presence of such coupling. As H_{SW1} could be increase when the applied field is reduced from saturation, the switching of the Ni segment starting from the antiparallel configuration could be

reduced when the applied field is increase along the FORC measurement in order to leave such antiparallel state as soon as possible. This effect would result in an effective shift on the switching of the Ni segment to negative values of the applied magnetic field, i.e., to negative values of Hu.

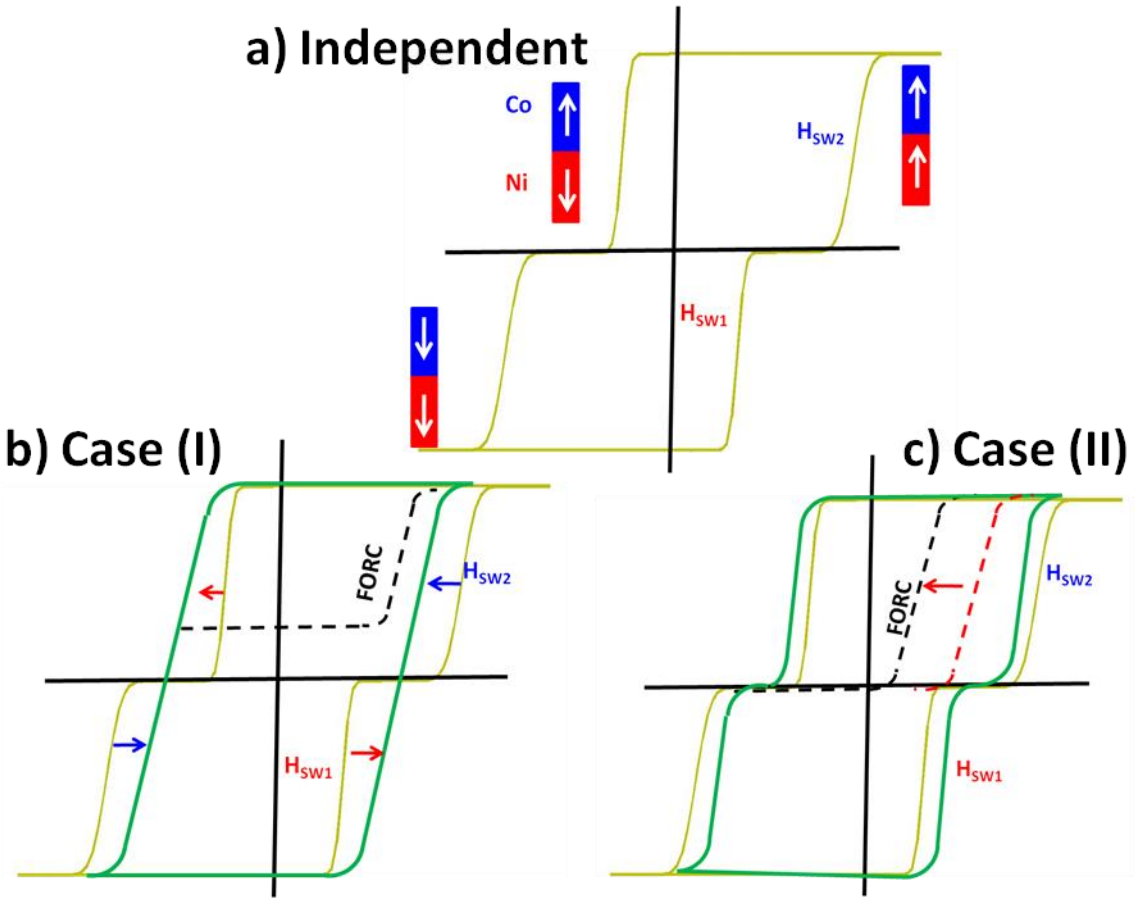

***Figure 4.18**: a) Schematic HL of two independent magnetic phases which reverse their magnetization at their intrinsic switching fields $\boldsymbol{H_{SW1}}$ and $\boldsymbol{H_{SW2}}$. b) and c) shows the modifications that the last HL can present where the exchange coupling between the nanowires is taken into account. Case I denote an averaged magnetic behavior where the reversal is carried out as in a homogeneous nanowire with average magnetic properties. Case II takes into account the antiparallel configuration which would modify the magnetic behavior of the softer phase along the FORC, being in this case Ni nanowires. Green lines denoted the resultant major hysteresis loop.*

4.5. Summary and Conclusions

In this chapter, a general overview of the method based on the FORC measurement as a powerful tool for evaluating the hysteretic processes involved in the magnetization reversal of magnetic nanowire arrays is presented. In order to prove the

potential of this method and, as well as, to support the discussion of the different experimental FORC diagrams performed in this work, a computational program based on a statistical approach has been performed and proved to be an accurate method for understanding the magnetization process in magnetic materials. Different characteristic scenarios, as distribution of switching fields, magnetostatic interactions among nanowires, reversible magnetization processes as well as more complex interactions between different ferromagnetic phases, have been studied in detail. All these previous scenarios have been correlated with experimental FORC diagrams obtained in the different kind of samples investigated in the present work, offering the possibility to deeply understand their magnetization process and evaluate the contribution of each scenario that could influence it.

In order to test the computational program as well as the FORC method by itself, exchanged coupled Ni/Co bi-segmented nanowire arrays have been fabricated and magnetically characterized. In order to extract the contribution of each nanowire composition as well as the different interactions between them, Ni and Co nanowire arrays, and both stacked nanowire arrays (Ni+Co sample) have been also investigated. From hysteresis loops at room temperature, both Ni and Co nanowires present a well-defined magnetization easy axis, which lies along the nanowire axis. Furthermore, Ni nanowires have been found to be magnetically softer than the Co ones allowing a well differentiation of each ferromagnetic phase when both types of nanowires are measured together, i.e., Ni+Co sample. As a first result, the magnetic behavior of this Ni+Co sample corresponds to the superposition of the respective Ni and Co independent magnetization reversal behaviors. Moreover, when the nanowires are exchange coupled at one end, hysteresis loops and thus the FORC are modified drastically with respect to the not-interaction case, which suggest that some additional effect is provided by the interface between Ni/Co bi-segmented nanowires. In a first approximation, the hysteresis loop of the exchange coupled Ni/Co nanowire array suggests that the effective magnetization reversal process would be driven by the softer ferromagnetic phase, in this case Ni segment, as far as the overall magnetic hysteresis is reduced taking values closer to the Ni nanowire array ones. However, even in the hysteresis loop, more than one magnetization reversal process can be distinguished. It results interesting the possibility to associate one of these processes with a magnetization reversal which would correspond to a magnetic phase with the switching field of the Ni nanowires, but with a magnetostatic

interaction strength among nanowires of Co array that is stronger than the respective of the Ni sample due to its higher saturation magnetization. Concerning to the FORC analysis made on this sample, other evidences of the coupling between the nanowires of Ni and Co have been found. The FORC diagram for Ni/Co sample can be associated with a system in which the antiparallel magnetization configuration in each nanowire is not energetically favorable.

5. MULTI-SEGMENTED Co_xNi_{1-x} NANOWIRE ARRAYS

Electroplated Cobalt has attracted much attention of scientific community as magnetic material due to its unique magneto-crystalline properties in terms of its capability to crystallize either in a fcc structure or hcp one. The ability to control the crystalline structure and/or the direction, at which the c-axis of the hcp phase growths, makes possible to tune the magnetic properties of the electrodeposited material. Since the shape anisotropy factor is independent of the composition, Co electroplating offers the possibility of modulating the magneto-crystalline anisotropy by adjusting the electrodeposition conditions in the appropriated way. Particularly, the effective magnetic anisotropy of electroplated Co nanowires can be tailored by controlling the pore diameter and the length of the nanowires, pH, current density or temperature of the electrolyte [Darques 2005, Vivas 2012, Vivas 2012 b]. Moreover, another route to change the crystalline properties of the Co is to alloy it with another material. In this sense, the high miscibility between the Co and Ni, together with the fcc structure of the last one are facts that have been extensively investigated and demonstrated to be a good manner of changing the magneto-crystalline properties of the material by properly adjusting its composition [Cheng 2008, Vega 2012, Vivas 2012 c].

The development of heterogeneous nanostructured materials as multi-layers or core-shell structures has also attracted much attention due to the capability to modify its physic-chemical properties for applications in many fields as opto-electronics and magnetic materials [Yoon 2010, Levy 1994]. The different contributions that can be dominant in the global behavior of the material concern the interface and collective contributions [Camley 1993]. In some cases the material behavior is driven by different structures, or contrary the different structures interact between each other showing complete different properties that are not necessarily a sum of the individual contributions.

In this chapter, the magnetic properties of multi-segmented $Co_{54}Ni_{46}/Co_{85}Ni_{15}$ nanowire arrays have been studied. In order to extract the influence of each segment to the collective magnetic behavior, the magnetic properties of nanowires with homogeneous composition and the same length as the multi-segmented ones have been compared. Furthermore, nanowires composed by one and three segments have been also

fabricated in order to study the influence of the multi-segmented arrangement of the composition. Due to the strong influence of the magneto-crystalline anisotropy on the magnetic properties, the crystalline structure of each composition will be studied in detail and correlated with the magnetic behavior afterwards.

5.1. EXPERIMENTAL PROCEDURE: SYNTHESIS OF CO-NI MULTI-SEGMENTED NANOWIRES

Nanowires with compositions $Co_{54}Ni_{46}$ and $Co_{85}Ni_{15}$ as well as the multi-segmented $Co_{54}Ni_{46}/Co_{85}Ni_{15}$ ones were grown by potentiostatic and pulsed potentiostatic electrodeposition, respectively, into the pores of Hard Anodized-porous anodic alumina membranes (HA-PAAM). The synthesis of these kinds of templates is explained in chapter 3, nevertheless the use of such a templates result in a pore diameter and therefore nanowires diameter of about 180 nm. On the other hand, the distance between pores or nanowires is nearly 300 nm. In order to protect the surface of the nanowires for the TEM characterization, the membranes where covered, after the freestanding of the HA-PAAM and previous to the electrodeposition of the nanowires, with a conformal SiO_2 layer of 2 nm thickness, by Atomic Layer Deposition (ALD) at 150ºC [Bachmann 2008].

Co_xNi_{1-x} nanowires were further electrochemically deposited starting from a Watts-type electrolyte containing 0.36M $CoSO_4$+ 0.04M $CoCl_2$+ 0.76M $NiSO_4$+ 0.13M $NiCl_2$ +0.073M H_3BO_3. The pH was maintained between 4 and 4.2 by adding NaOH up to the desired value. In order to avoid the precipitation of the boric acid, the electrodeposition was carried out at 35ºC without mechanically stirring. Such electrodeposition process was carried out under potentiostatic conditions in a three electrode electrochemical cell equipped with an Ag/AgCl reference electrode. Taking into account that the standard reduction potentials of Co and Ni are quite similar, in principle both elements would be deposited at the same ratio under a certain applied electrodeposition potential. This would mean that if the composition of the electrodeposit had to be changed, the only way to do it would be by varying the concentration of the starting electrolyte. However, an anomalous electroplating behavior appears in Co-Ni based electrodepositions, resulting in a preferential deposition of Co atoms at low values of the deposition potential [Tian 2011, Gómez 1998, Gómez 2005, Ghahremaninezhad 2009]. This fact offers the possibility of modifying the Co-Ni composition of an electrodeposit by directly varying the deposition potential [Vega 2012, Prida 2013],

which allows the synthesis of multilayered or multi-segmented Co-Ni nanomaterials. It is clear that, by varying the electrodeposition potential between two values during the same electrodeposition, it is possible to tune the desired composition of the nanowire along its length. Furthermore, by adjusting the time at which the potential is constant at a certain value, the length of the different segments can also be tuned.

The dependence of the alloy composition and growth rate on the electrodeposition potential was determined by SEM and EDX studies for homogenous Co-Ni alloy nanowire arrays. Those nanowires were grown at several deposition potentials in order to optimize the parameters of the pulse sequence attending to the composition and growth rate. The optimized electrochemical parameters were further employed for the fabrication of multi-segmented $Co_{54}Ni_{46}/Co_{85}Ni_{15}$ nanowire arrays. These results are illustrated in *Figure 5.1* a). The growth rate increases from 150 nm/min to 1500 nm/min when the electrodeposition potential is decreased from −0.8 down to −1.4 V, whereas the cobalt content of the nanowire alloy increases from 54 up to 85 at.% in the same voltage interval. The pulsed electrodeposition potential sequence shown in *Figure 5.1* b), employed for the synthesis of multi-segmented Co-Ni nanowires, consisted of cycles comprising a first deposition pulse of 86.83 s at −0.8 V followed by a second deposition pulse with a duration of 7.09 s at −1.4 V, which results in nanowires composed of bi-segments consisting of $Co_{85}Ni_{15}$ and $Co_{54}Ni_{46}$ alloys with a mean length of 200nm.

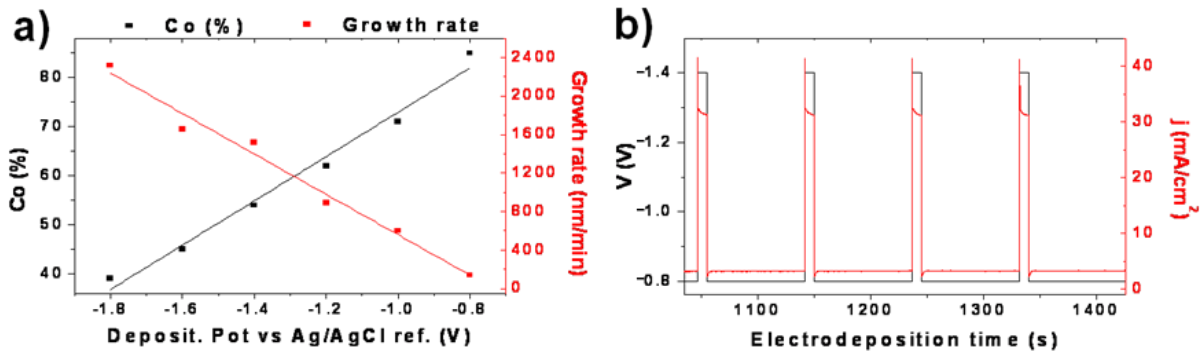

***Figure 5.1**: a) Linear dependence of the Co content and Growth rate of the nanowires as a function of the deposition potential measured in electrodeposited homogeneous nanowires. b) Pulsed electrodeposition employed in the fabrication of multi-segmented nanowires where the applied potential is varied between -1.4V and -0.8V vs an Ag/AgCl reference electrode.*

As it was mentioned at the beginning of this chapter, different kinds of samples have been fabricated. A detailed summary of the different types of Co-Ni nanowires can be found in *Table 5.1*. The multi-segmented nanowires consist in 25 segments of each

composition, 50 segments in total, what means that the entire nanowire is 15 µm long. At the same time, homogeneous long nanowires have been made to clarify if the global geometry of the nanowires affects the magnetic behavior of the material, or in contrast it is mainly determined by the multi-segmented nature of the nanowires. After each electrodeposition process, a gold cap was electrodeposited on top of the nanowires in order to avoid oxidation or damage at the end of the nanowires

Nanowires	Composition (at. %)	Length
Homogeneus	$Co_{54}Ni_{46}$	~12 µm
	$Co_{85}Ni_{15}$	~12 µm
One Segment	$Co_{54}Ni_{46}$	290 nm
	$Co_{85}Ni_{15}$	422 nm
Three Segments	$Co_{54}Ni_{46}$/ $Co_{85}Ni_{15}$/ $Co_{54}Ni_{46}$	~1 µm
	$Co_{85}Ni_{15}$/ $Co_{54}Ni_{46}$/ $Co_{85}Ni_{15}$	~1.1 µm
Multi-segmented	……$Co_{85}Ni_{15}$/$Co_{54}Ni_{46}$ ……..	~15 µm

Table 5.1*: Summary of fabricated Co-Ni nanowire arrays varying both, length and number of segments with different compositions.*

5.2. MORPHOLOGICAL AND CRYSTALLOGRAPHIC CHARACTERIZATION

In order to perform TEM studies on the Co-Ni nanowires, an additional preparation of the nanowires is required. Since the electron beam has to cross the sample, it needs to be as thin as possible. The most common procedure to prepare freestanding nanowires grown by the template assisted method studied in this work is dissolving the PAAM template resulting in a solution of the freestanding nanowires. This process is performed by the same chemical etching employed between the first and the second anodization ($0.18M\ CrO_3 + 0.61M\ H_3PO_4$). It is along this process when the protective layer of SiO_2 grown by ALD plays a critical role, avoiding the etching of the magnetic nanowire itself.

SEM micrograph of the nanowires array and TEM images of isolated nanowires have been taken to verify the multi-segmentated structure of the Co–Ni alloy nanowires made by pulsed electrodeposition. The *Figure 5.2* a), corresponds to a SEM cross-section view of multi-segmented nanowires where the bottom and top protective Au caps can be clearly distinguished. The multi-segmented $Co_{54}Ni_{46}$/$Co_{85}Ni_{15}$ structure is also visible

with a slight change in the contrast of the image. More detailed TEM micrographs in *Figure 5.2* b) also reveal the sequence of segments with alternating Co–Ni alloy composition. The EDS line scan performed in the middle along the longitudinal axis of a single $Co_{85}Ni_{15}/Co_{54}Ni_{46}$ segmented nanowire (*Figure 5.2* c), d)), discloses that the Co and Ni content distributions are very uniform in each segment of the nanowire. On the other hand, the distribution of both Co and Ni fluctuates among adjacent segments and thus, the composition of segments alternates between $Co_{55}Ni_{45}$ and $Co_{82}Ni_{18}$, in agreement with previous results obtained from the SEM/EDS characterization of homogeneous Co-Ni alloy nanowires. Furthermore, the nanowire segments that appear as thinner and longer are rich in Co, being the widest and shortest segments those with a higher Ni content. The mean length of the $Co_{54}Ni_{46}$ alloy segments estimated from these images was 290 ± 30 nm, and the mean length of the segments with $Co_{85}Ni_{15}$ alloy composition was 422 ± 50 nm. Although the pulse sequence of the electrodeposition process was designed basing on a previous calibration of the growth rate/composition for each deposition potential in order to keep the same length in both segments, the difference in the deposition efficiency has played an important role in such short deposition pulses and thereby the length of the Co-rich segments is slightly longer than that of the $Co_{54}Ni_{46}$ ones. On the other hand, the diameter modulation of each Co-Ni segment could be an indication of a slight chemical etching on the surface of Co-rich segments during the process of releasing the nanowires from the HA-AAO template. However, such etching or oxidation is not observed in the Ni-richer segments as a result of the different corrosion resistance behaviors of $Co_{85}Ni_{15}$ and $Co_{54}Ni_{46}$ alloys [Srivastava 2006].

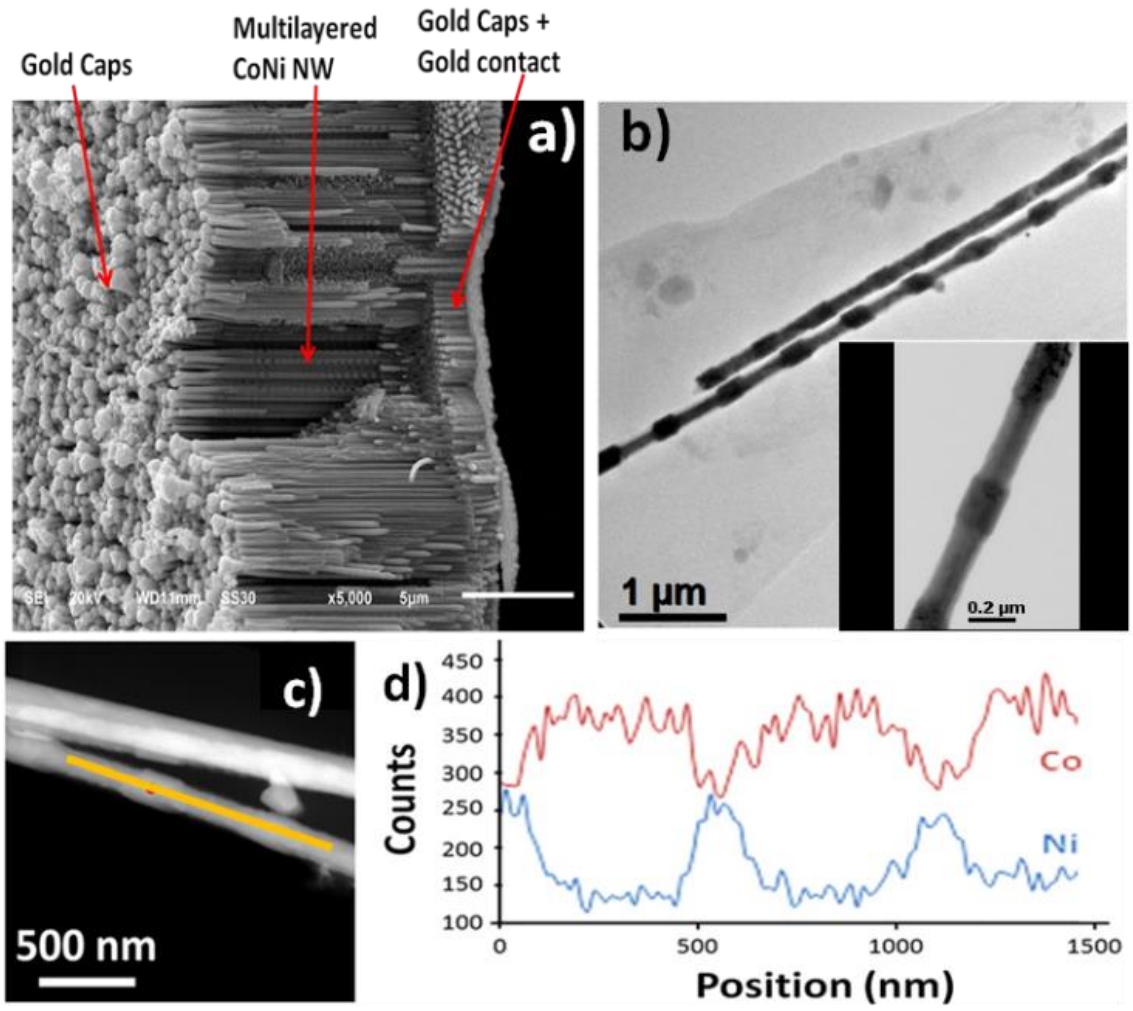

***Figure 5.2**: a) SEM cross section view of Co-Ni multi-segmented nanowires array, b) TEM image of made on free standing nanowires where the segmented regions are clearly seen. c) Marked region where the compositional line scan d) demonstrate the compositional modulation of the nanowires.*

Once the multi-segmented pattern of the nanowires is characterized, it becomes necessary to study the crystalline structure of each segment of different composition, which will affect strongly the magnetic properties of the sample. In order to correlate the different crystalline phases with the different compositions, XRD measurements have been done in the homogeneous nanowires of each composition as well as in the multi-segmented ones. The indexed XRD pattern of each type of nanowire array can be found in *Figure 5.3*. In the case of nearly equiatomic composition of Co–Ni alloy, its crystalline phase is a fcc structure that can be ascribed to the influence of Ni atoms. Moreover, as the Co content is increased, the main crystallographic phase is turned to Co-hcp one. However, the previous fcc phase is still present into the alloy what can be correlated with an small influence of the low portion of Ni atoms together with the tendency of Co to

crystallize under fcc phase during the first moments of the electrodeposition [Pirota 2011]. The XRD pattern corresponding to the multi-segmented Co–Ni alloy nanowires shown in *Figure 5.3* c) exhibits a mixture of fcc and hcp phases since these nanowires are formed by an alternating sequence of segments of both previous compositions.

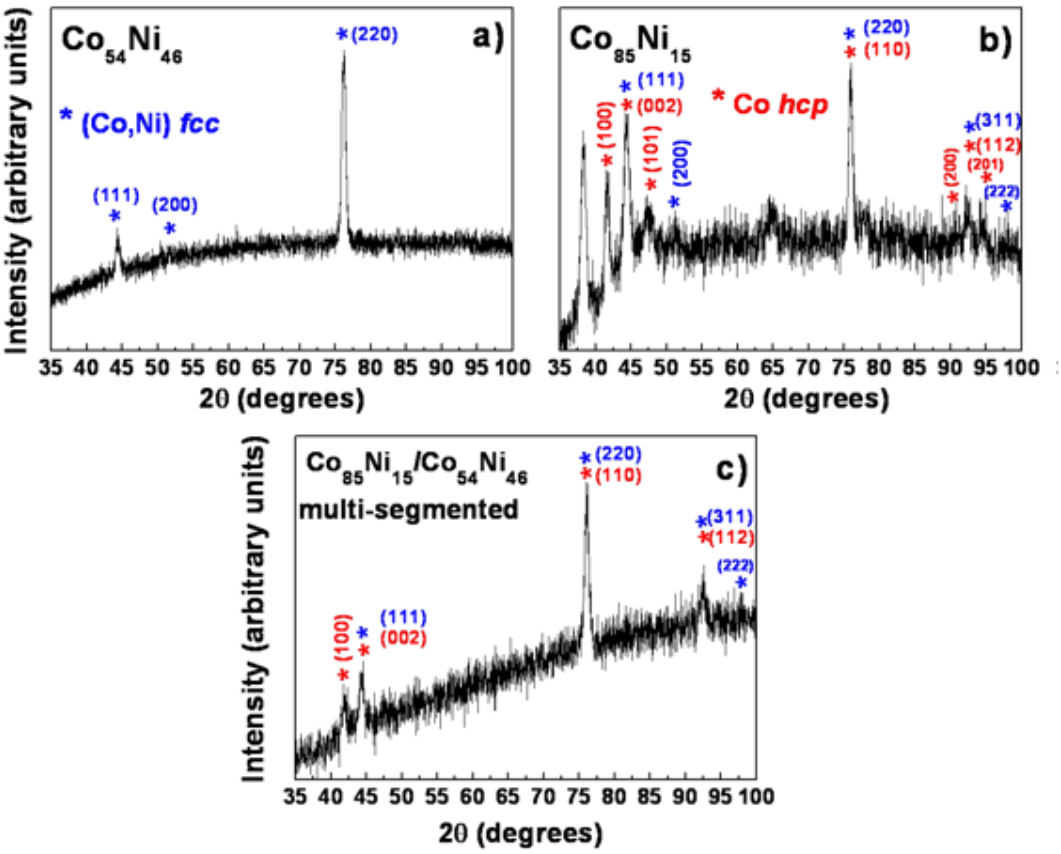

***Figure 5.3**: XRD patterns of homogeneous $Co_{54}Ni_{46}$ a), $Co_{85}Ni_{15}$ b) and multi-segmented c) nanowires arrays.*

In order to study the influence of the pulsed electrodeposition process as well as the influence of the previous segment acting as working electrode for the following segment in the electrodeposition, SAED spectra have been taken in different segments of the multi-segmented nanowires. The left image of *Figure 5.4* shows typical TEM images of the Co-Ni nanowires, where their multi-segmented structure is again evidenced. The SAED patterns of two different representative segments of the same Co-Ni nanowire (highlighted by circles in the TEM micrograph), allow to distinguish between the structure of both segments, being hcp for the $Co_{85}Ni_{15}$ segment (1), while fcc is the corresponding to the $Co_{54}Ni_{46}$ one (2). The local examination of the microstructure and composition of the different nanowire segments reveal that their crystalline structure

changes as the Co/Ni ratio is modified. Particularly, it was found that nanowire segments with high cobalt content display SAED patterns that correspond to hcp single crystals observed through the [0001] plane, what means that the c-axis of the hcp phase grows perpendicular to the nanowires. On the other hand, nanowires segments with almost equiatomic composition exhibit SAED patterns corresponding to a Co-Ni alloy single crystal with a fcc structure, where the <111> direction lies along the nanowire axis. Interestingly, in several of these SAED patterns, either the diffraction spots appear slightly elongated or such spots appear splitted in two or three ones. This fact evidences fluctuations in the cell parameter as well as in small rotations of the crystalline structure what can be ascribed to a gradient of the Co/Ni ratio into the same segment and/or the effect of transversal stresses produced by the confined nanowires growth into the pores of the alumina template. The appearance of the hcp structure for Co-Ni alloys with high Co content is in agreement with its equilibrium phase diagram [Hansen 1958]. However, it is worth noting that in some of the studied nanowire segments, the hcp phase has been also found in $Co_{54}Ni_{46}$ segments, probably as a consequence of the non-equilibrium nature of the electrodeposition processes**.**

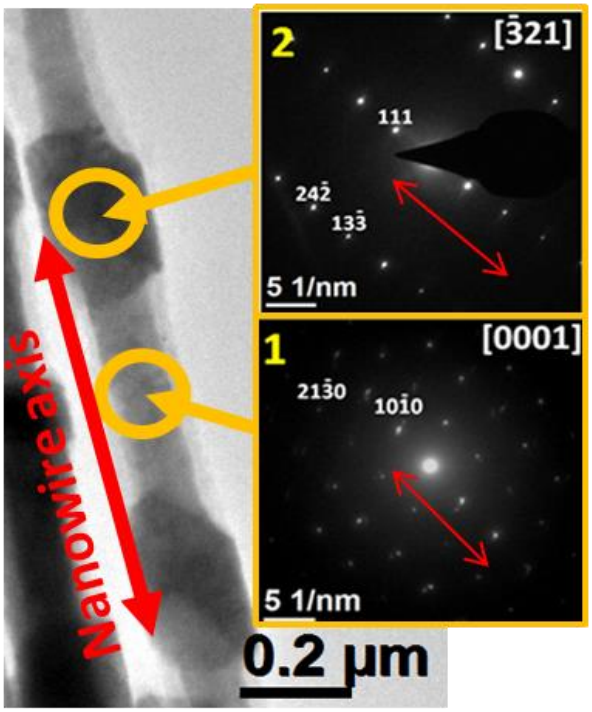

Figure 5.4*: SAED spectra measured in segment $Co_{85}Ni_{15}$ 1) and $Co_{54}Ni_{46}$ 2) where an hcp and fcc phase respectively can be indexed. Both measurements also reveal the preferential orientations of the crystals where the c-axis of the hcp is perpendicular to the nanowires axis and the [111] direction of the fcc lies along the nanowires long axis.*

5.3. MAGNETIC CHARACTERIZATION

The aforementioned structural characterization has pointed out that the crystalline structure of the Co-Ni alloy is strongly dependent on its composition. In order to study the magnetic properties of samples with different crystalline structures and thus different compositions, nanowire arrays composed by only one segment will be studied first. In *Figure 5.5*, the major hysteresis loops (HL), measured along the parallel and perpendicular directions with respect to the nanowires long axis, are showed for $Co_{85}Ni_{15}$ and $Co_{54}Ni_{46}$ segments. In case of Co-rich segments, the HLs are very similar in both directions, indicating some kind of magnetic isotropy. As we know from the previous section, the Co-rich hcp structure tends to growth with its c-axis along the perpendicular direction, which would result in a transverse crystalline anisotropy. However, the small shape anisotropy of these short segments, slightly larger than the one corresponding to the equiatomic composition, and probably helped by the presence of a considerable fcc phase from the first stages of the electrodeposition, produces a competition between both types of anisotropies. In addition, there is an important reversible contribution of the magnetization process in both directions suggesting that two different processes are involved in the magnetization reversal. However, the HLs of $Co_{54}Ni_{46}$ show appreciable differences depending on the direction of the applied magnetic field. In case of the field perpendicularly applied with respect the nanowires axe, although a reversible behavior is present, a large part of the magnetization reversal is driven by a low coercive irreversible process. Two clearly irreversible behaviors take part on the magnetization reversal process along the parallel direction, as can be seen in the widening of the HL near the coercive field. Furthermore, the hysteresis shape along the parallel direction, that reveals again both behaviors with different contributions to the hysteresis, is shown in the inset of *Figure 5.5* b). The distribution with lower coercivity is clearly similar to the perpendicular one where the peak at M/Ms=0 is not observed. .

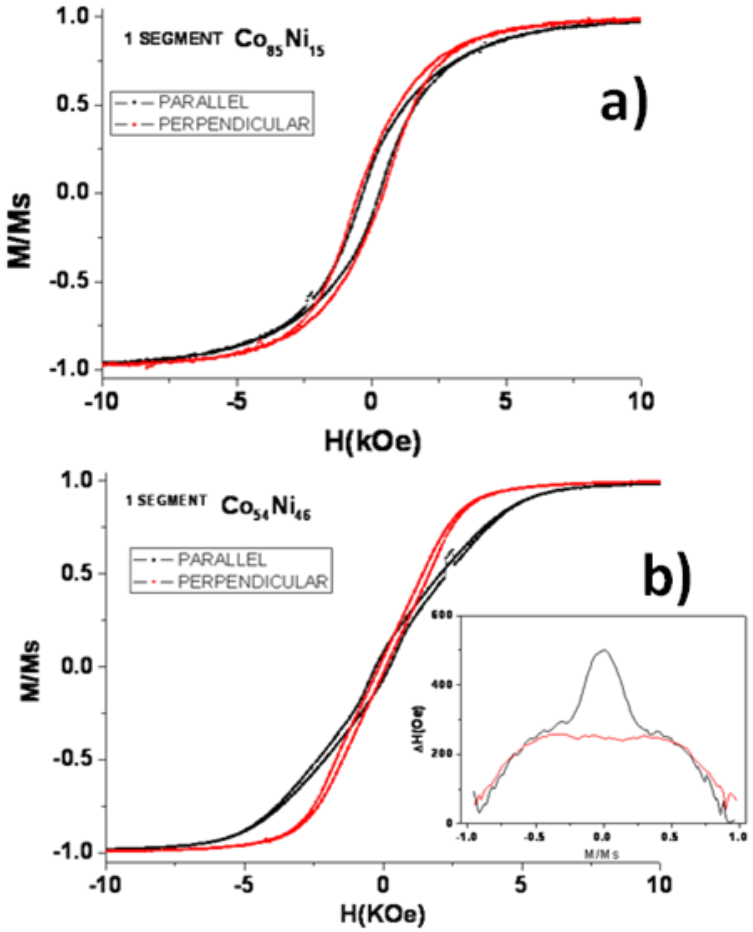

***Figure 5.5**: Hysteresis loops of $Co_{85}Ni_{15}$ a) and $Co_{54}Ni_{46}$ b) one segments measured along the parallel (black) and perpendicular (red) directions. The inset in b) presents the hysteresis shape of $Co_{54}Ni_{46}$.*

Figure 5.6 shows the hysteresis loops of $Co_{85}Ni_{15}$ and $Co_{54}Ni_{46}$ homogeneous long nanowire arrays measured along both, parallel and perpendicular directions. It can be shown that the samples do not exhibit a clear easy magnetization axis since the process is mainly driven by reversible magnetic rotation along both directions. In particular, the perpendicular HL of $Co_{85}Ni_{15}$ shows a more complex magnetic behavior composed of several contributions. In addition to the centered switching field distribution (SFD) two switching events appear (*Figure 5.6* c)), which can be associated with hysteresis (see *Figure 5.6* b)) near the magnetization saturation. The mixture of the different crystalline structures in case of $Co_{85}Ni_{15}$ alloy, highlighted by the XRD measurements, might be the responsible of the two different contributions to the SFD. Accordingly with the single segment nanowires studied above, the contribution to the hysteresis of 500 and 200 Oe (peaks in *Figure 5.6* b)) could be related to the presence of mixed hcp and fcc phases, respectively. The $Co_{54}Ni_{46}$ nanowire arrays show an unhysteretic behavior along the

perpendicular direction with respect to the nanowires axis. However, along the parallel direction the situation is almost the same with a small hysteresis and a very strong reversible magnetization reversal component with an anisotropy field even larger than in the previous direction.

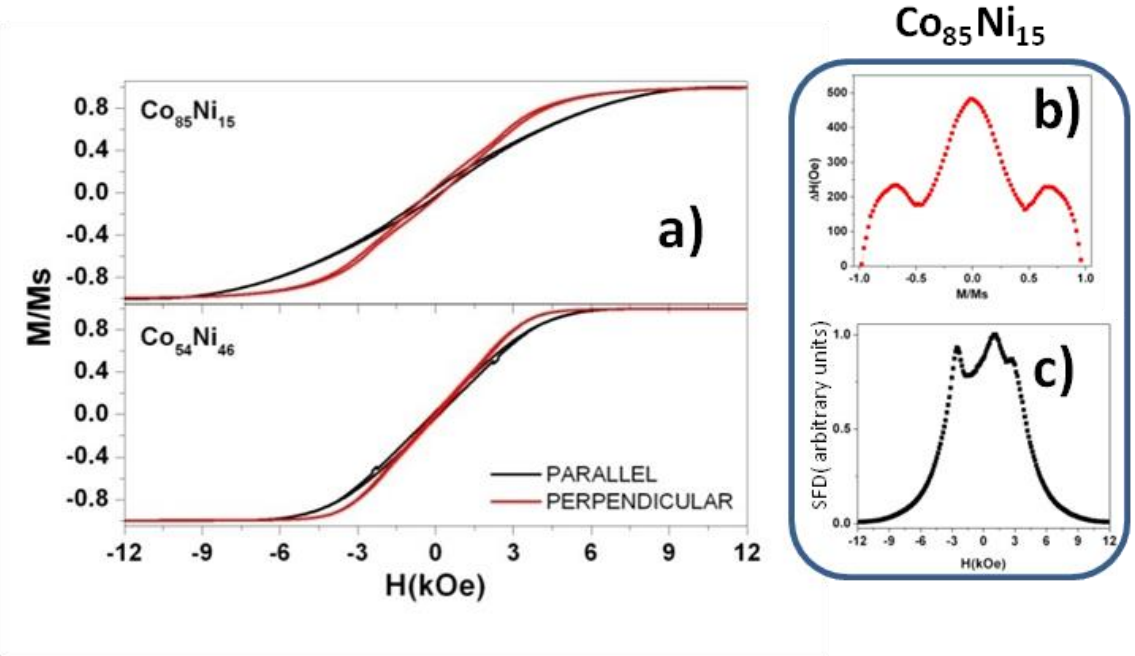

***Figure 5.6**: a) Hysteresis loops of $Co_{85}Ni_{15}$ (up) and $Co_{54}Ni_{46}$ (down) 10 µm homogeneous nanowires measured along the parallel (black) and perpendicular (red) directions. b) Hysteresis shape and c) switching field distribution of $Co_{85}Ni_{15}$ nanowire array measured along the perpendicular direction.*

The effect that the crystalline structure may have on the magnetization process has been evidenced, however if the segments of each composition are stacked together, the reversal process can be modified. In *Figure 5.7*, the HLs measured in nanowires composed of three segments in the two possible configurations are displayed. Both HLs appear very similar to the single segment of $Co_{54}Ni_{46}$, and a large amount of reversible processes plays the most important role. In order to study the reversal behavior in more detail, the hysteresis shape and the SFD have been extracted from the HLs. First, along the parallel direction, the SFD shows in both type of samples an increase of the susceptibility near the coercive field. However, this abrupt peak is not correlated with a hysteretic process since the hysteresis tends to zero near Hc, as can be seen in *Figure 5.7* c). This effect could be better correlated with a magnetization reorientation to a more stable configuration pointing along the perpendicular direction. Moreover, along this perpendicular direction, the sharp peak centered at Hc is still visible in *Figure 5.7* f), although in this case it can be

associated with hysteresis. In contrast, the two secondary peaks that appear for the $Co_{85}Ni_{15}$/ $Co_{54}Ni_{46}$/ $Co_{85}Ni_{15}$ at both sides of the central SFD peak are the responsible of the plateau observed near magnetization saturation (see *Figure 5.7* d)). The previous behavior is more pronounced in the case of three segments $Co_{85}Ni_{15}$/ $Co_{54}Ni_{46}$/ $Co_{85}Ni_{15}$, and is very similar with respect the one of $Co_{85}Ni_{15}$ long nanowires where the coexistence of crystalline phases was demonstrated by XRD.

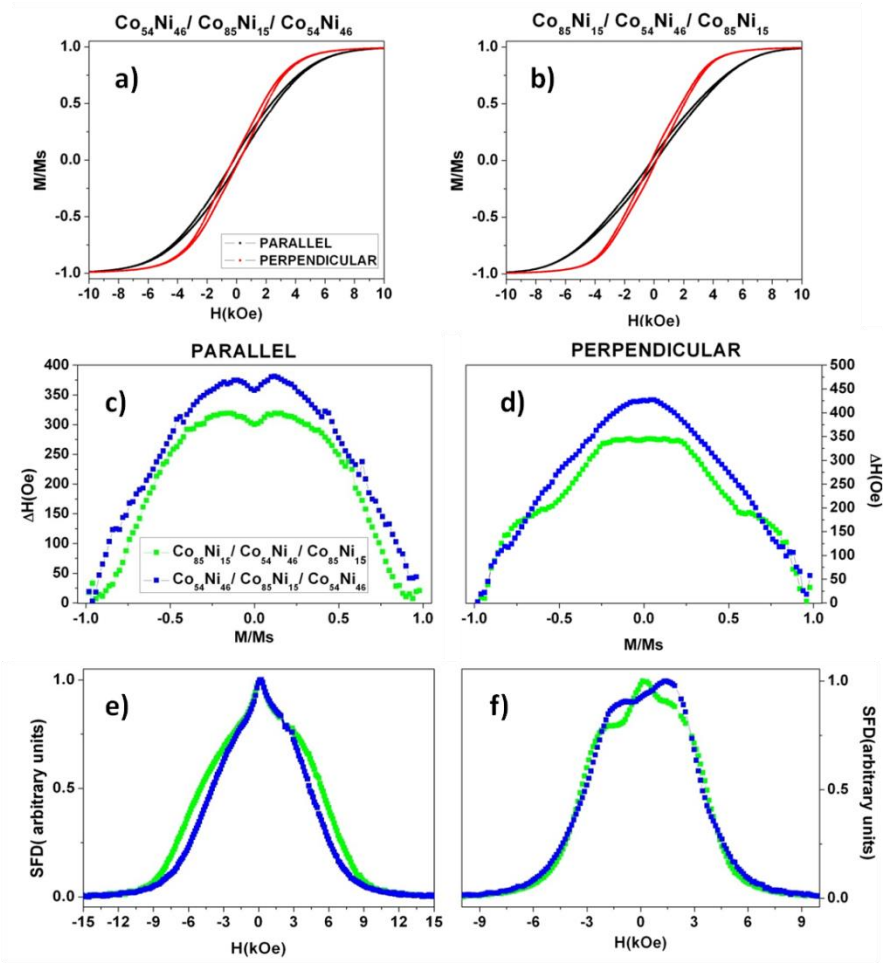

***Figure 5.7**: a) and b) Hysteresis loops of $Co_{54}Ni_{46}/Co_{85}Ni_{15}/Co_{54}Ni_{46}$ and $Co_{85}Ni_{15}/Co_{54}Ni_{46}/Co_{85}Ni_{15}$, respectively, measured along the parallel (black) and perpendicular (red) directions. c) and d) The hysteresis shapes of both samples obtained along the parallel and perpendicular directions respectively, while e) and f) are the switching field distributions.*

Finally, the multi-segmented nanowires array do not show a clear easy magnetization axis, where the Hc in both parallel and perpendicular directions is almost the same as can be seen in *Figure 5.8*. Moreover, the SFD and the hysteresis shape reveal two different magnetization processes along the perpendicular direction to the nanowires axis, in a similar way to the magnetic behavior presented by three segmented nanowires. With

respect to the long homogeneous nanowires, the effect of segments on the global magnetic behavior is to delocalize the effective magnetic anisotropy becoming in a more isotropic magnetization ascribed to the contribution of the two different alloy compositions present in the nanowires.

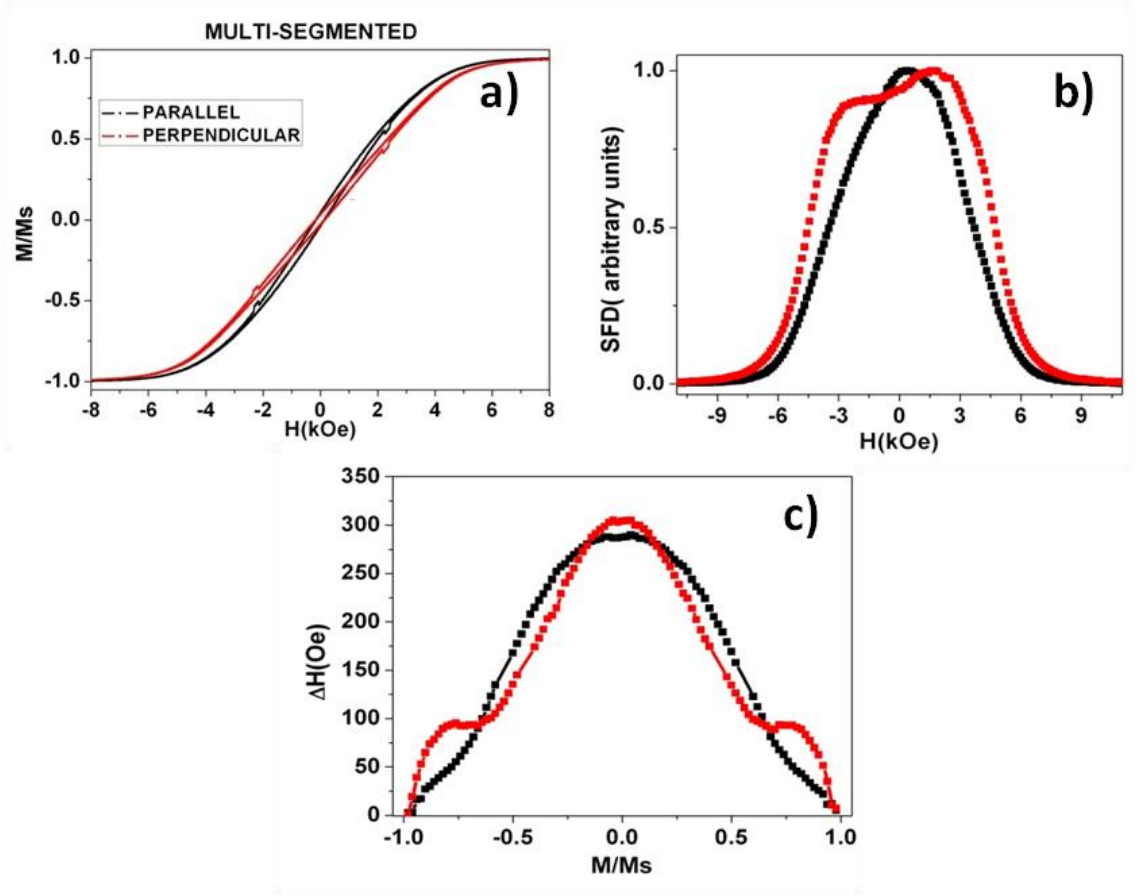

***Figure 5.8**: a) Hysteresis loops, b) switching field distribution and c) hysteresis shape of multi-segmented nanowire arrays along the parallel (black) and perpendicular (red) directions with respect to the nanowires long axis.*

As a brief summary of the information extracted from the previous magnetic characterization, the values of the coercive field and reduced remanence are collected in *Table 5.2*. Those values point out once more the isotropic behavior of all the nanowire arrays and the low coercivity and reduced remanence of the magnetization reversal processes.

Sample	Composition (at.%)	Hc (Oe)		M/Ms	
		Para.	**Perp.**	**Para.**	**Perp.**
Homogeneus	$Co_{54}Ni_{46}$	120	64	0.03	0.019
	$Co_{85}Ni_{15}$	180	240	0.033	0.05
One Segment	$Co_{54}Ni_{46}$	250	122	0.07	0.043
	$Co_{85}Ni_{15}$	310	450	0.15	0.19
Three Segments	$Co_{54}Ni_{46}$/ $Co_{85}Ni_{15}$/ $Co_{54}Ni_{46}$	175	215	0.043	0.055
	$Co_{85}Ni_{15}$/ $Co_{54}Ni_{46}$/ $Co_{85}Ni_{15}$	150	170	0.031	0.049
Multi-segmented	……$Co_{85}Ni_{15}$/$Co_{54}Ni_{46}$ ……..	144	150	0.04	0.032

***Table 5.2**: Collection of coercive fields and reduced remanences of all samples measured along the parallel and perpendicular directions to the nanowires axis.*

The magnetization reversal processes in most of the previous samples are composed by at least two different contributions, which were ascribed mainly to the coexistence of the two different crystalline phases. However, it is a difficult task to get a complete description about both contributions basing only on the major hysteresis loops [Pirota 2011]. For that reason, the different samples have been analyzed by measuring their FORC. As can be seen in *Figure 5.9*, for $Co_{85}Ni_{15}$ single segment nanowire arrays, a wide distribution of low coercivities can be appreciated near Hc=500 Oe. The strong component of reversible magnetization processes affects the distribution through the measurement since the increment of Hr has to be chosen large enough to measure the FORC in an acceptable period of time. This means that the number of reversal fields along the distribution is lower than usual elongating then the FORC distribution along Hc and Hu in the same way and resulting in a wide spot. On the other hand, the parallel FORC diagram of $Co_{54}Ni_{46}$ shows the same characteristics as the previous ones, although a more complex behavior is observed along the perpendicular direction. The FORC diagram shown in *Figure 5.9* obtained for $Co_{54}Ni_{46}$ along the perpendicular direction, suggest that there are some irreversible processes near the magnetization saturation that in addition are shifted along the applied magnetic field axis. According to the FORC diagram and the SFD as well as the hysteresis plots, the switching distribution centered at the coercive field could be affecting strongly the switching of another magnetically softer phase. If the applied magnetic field is decreased from saturation, the softer magnetic phase switches earlier due to the negative interaction with the centered distribution which would tend to remain in an antiparallel configuration. Moreover, when the centered peaks

on the SFD of *Figure 5.7* f) starts to switch the magnetization it also promotes, through a strong interaction, a simultaneous switching of the magnetically softer phase being redirected against the applied magnetic field. Then the soft magnetic phase has to be switched again symmetrically with respect the switching of the centered peak of the SFD.

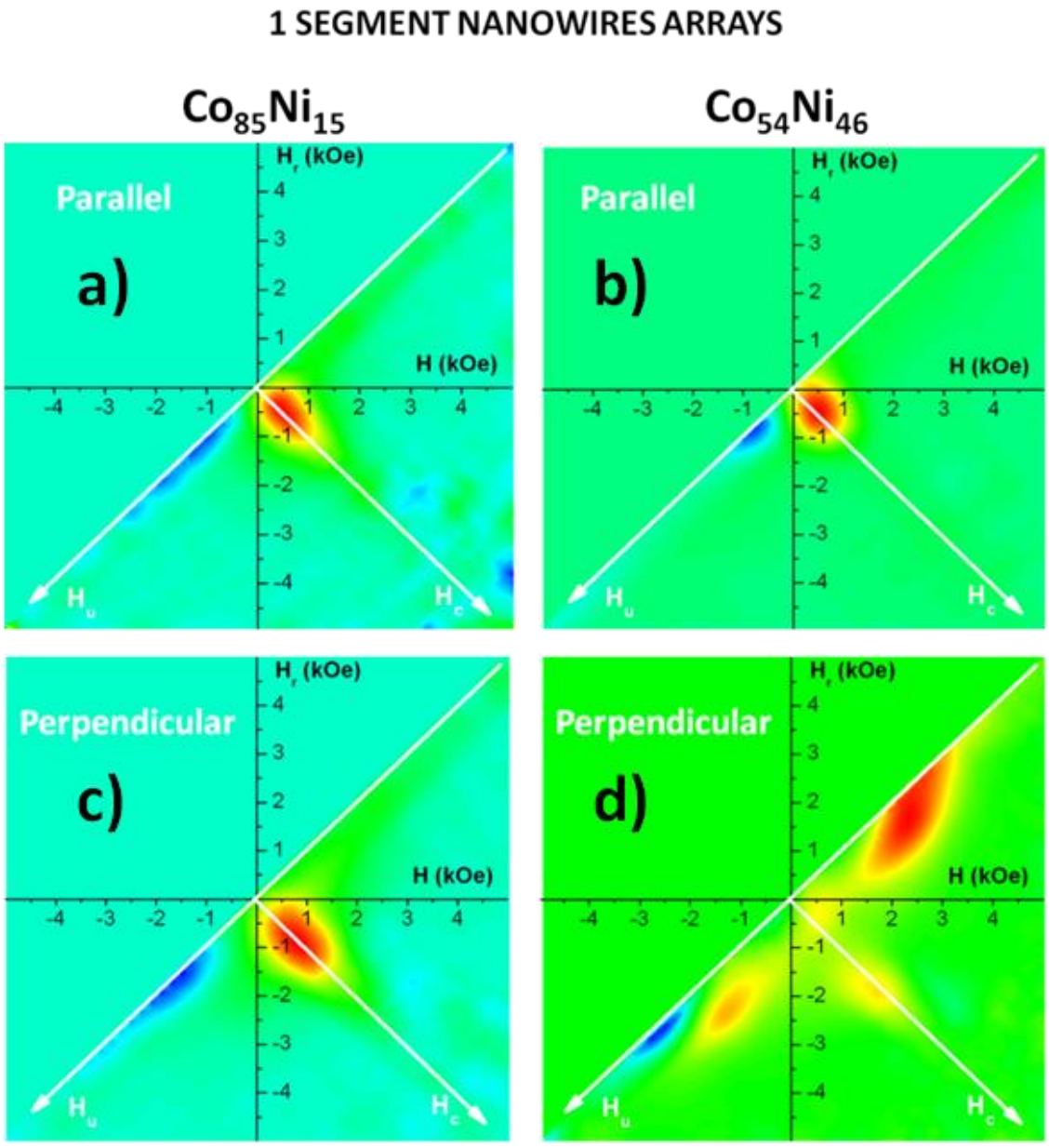

***Figure 5.9**: FORC diagrams for one segment nanowire arrays of $Co_{85}Ni_{15}$ and $Co_{54}Ni_{46}$ along the parallel (a,b) and perpendicular (c,d) directions, respectively.*

As the previous magnetic behavior was only detected along the perpendicular direction to the nanowire axis, our study will be focused along that direction in order to see how the effect depends on the number of segments as well as on the composition of the homogeneous nanowires. The comparison between the most illustrative samples has

been done by representing the Hu profile made on the FORC diagrams at Hc constant as can be seen in *Figure 5.10*. The observed behavior is in agreement with the existance of two different SFD coupled with a strong negative interaction between them. Under this context, when the interaction is becoming stronger, the SFD of the softer magnetic phase is shifted along the applied magnetic field, i.e. along the Hu axis in the FORC diagram. Furthermore, with stronger negative interactions, the switching of the centered SFD responsible of the Hc of the major HL may be able to reverse the magnetically softer phase against the applied magnetic field again, (see *Figure 5.11*). However, the switching of the magnetic phase responsible of the coercive field, in general, does not reverse the magnetization of the whole magnetically softer distribution, what means that the intensity of the peak at -Hu will be lower than the one at Hu, and even more, the lower the negative interaction the smaller the peak at –Hu. It can be seen in *Figure 5.10* that when the peaks related to the shifted SFD appear at larger Hu (stronger interactions) the differences between the peaks intensity at Hu and –Hu is decreasing. On the other hand, in the case of $Co_{54}Ni_{46}$/ $Co_{85}Ni_{15}$/ $Co_{54}Ni_{46}$, the shifted SFD appears at lower values of |Hu| what means a lower interaction, and probably too low to induce the reversal of the softer magnetic phase at Hc disappearing the FORC distribution at –Hu.

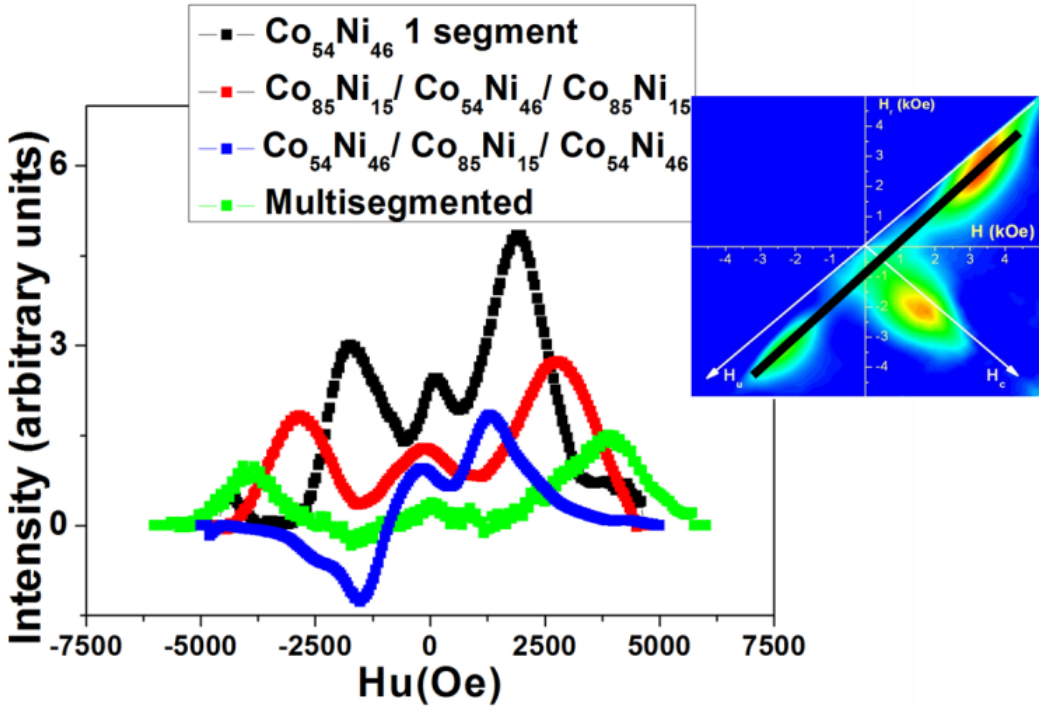

***Figure 5.10**: Hu profiles obtained from the perpendicular FORC diagrams as a function of the number of segments. In the inset the black line marks the position corresponding to an example of a Hu profile.*

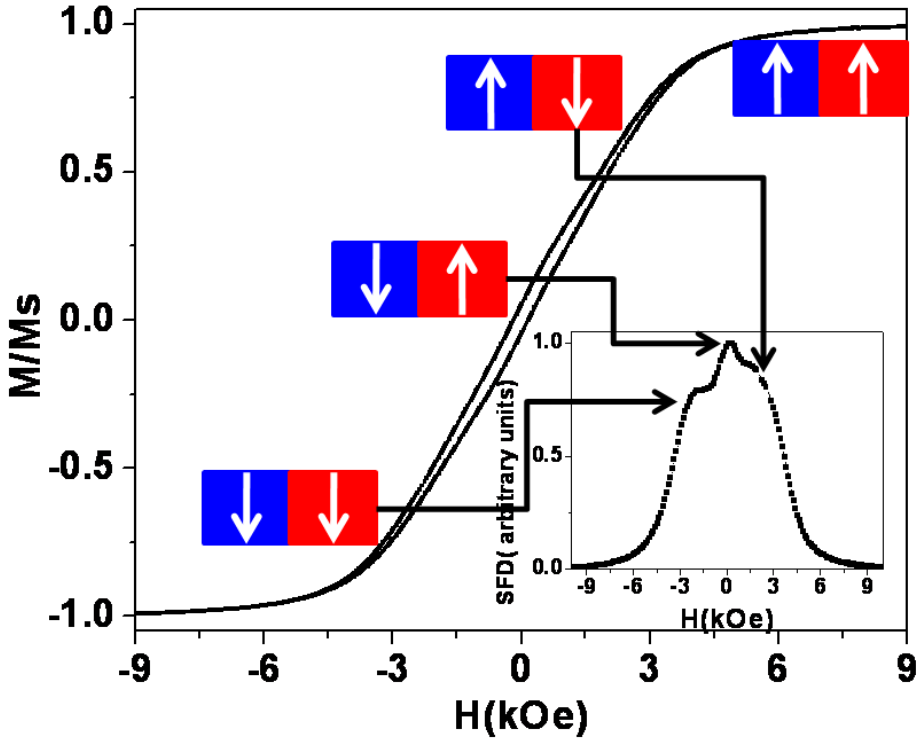

***Figure 5.11**: Hysteresis loop and SFD (inset) where the different switching process and magnetic configurations are schematically shown.*

5.4. SUMMARY AND CONCLUSIONS

$Co_{85}Ni_{15}/Co_{54}Ni_{46}$multi-segmented nanowires arrays have been successfully fabricated by means of pulsed electrodeposition into the pores of hard anodized nanoporous alumina membranes. The ability to change the composition of Co-Ni alloy by modifying the electrodeposition potential has allowed the growth control of such multi-segmented heterogeneous nanowires. Nanowire arrays consisted in long homogeneous nanowires of each composition, a short-segment array for each composition, as well as three segments in each nanowire in two different configurations have been also fabricated and used as reference samples to compare the effect of the multi-segmentation of the nanowires.

Form XRD characterization made in the homogeneous long nanowires arrays and in the multi-segmented ones, it can be concluded that in the case of the nearly equiatomic

composition nanowires, the main phase is the fcc crystalline structure being associated with the effect of the Ni crystallization promoting the same phase in Co. However, in case of Co-rich nanowires, a mixture of fcc and hcp phases has been found. In case of the multi-segmented nanowires, this mixture has been also found, as it was expected, since those nanowires are composed by the two different compositions. Along with the compositional modulation of the multi-segmented nanowires, and as a consequence of it, a multi-segmented modulation of the crystalline structure has been also confirmed. A more localized structural characterization has been performed by TEM/SAED on each composition segment. In the case of Co-rich segment, the crystalline structure corresponds to the uniaxial hcp phase with its c-axis grown along the perpendicular direction with respect to the nanowire axis. In contrast, the main crystalline phase in $Co_{54}Ni_{46}$ segment corresponds to the fcc one, although some segments show the hcp phase.

Room temperature hysteresis loops show that, in general, all samples display low coercive field and reduced remanence values, together with a not well-defined uniaxial magnetic anisotropy. The single segment nanowire arrays present the largest differences between $Co_{85}Ni_{15}$ and $Co_{54}Ni_{46}$ above mentioned magnetic parameters. In the first case, the higher value of the coercive field is obtained together with a near isotropic behavior mainly ascribed to the competition between shape and crystalline magnetic anisotropies, in such short segments. For the one $Co_{54}Ni_{46}$ segment nanowire array does not show a clear magnetization easy axis although there are differences between the measurement along the parallel and perpendicular direction with respect to the nanowire axis. Interestingly, when both kinds of segments are stack together in the three segment nanowire arrays, the behavior observed in$Co_{85}Ni_{15}$ one segment nanowire array is not observed anymore and, the magnetization reversal behavior is similar to the one presented by the $Co_{54}Ni_{46}$ one segment nanowire array. One of the possibilities responsible of this behavior can be extract from last section in chapter 4 since one of the segments would drive the magnetization reversal process. The main difference in the hysteresis loop of the multi-segmented nanowire array with respect to the one corresponding to the homogeneous long nanowire array, and in turn to the three segment nanowire array, lies on a rather isotropic magnetization reversal behavior.

However, paying more attention to perpendicular hysteresis loops, different hysteresis sources were detected. In order to analyses such peculiar behaviors, FORC

characterization has been performed in these samples. FORC diagrams along the perpendicular direction point out two different contributions to the magnetization reversal process for all samples. These contributions cannot be correlated with the different segments, at least as a first approximation, since the homogeneous Co-rich long nanowire array also presents such behavior. In fact, due to Co-rich long nanowires show a mixture of crystalline phases, it makes reasonable to think that this mixture is the responsible of the observed two different magnetization reversal processes. In addition, the magnetic behavior of those nanowires along the perpendicular direction might correspond to two interacting ferromagnetic phases where the switching of one phase provokes the switching back of the softer phase during the magnetization reversal process.

6. NANOWIRES ARRAYS OF CO-CU SOLID SOLUTIONS

As was mentioned in the previous chapter, the cobalt role in magnetic nanomaterials has been extensively studied due to its characteristic uniaxial crystallographic phase. Furthermore, the management of magnetic properties through the controlled growth of a certain crystalline structure is interesting to model new functional magnetic devices. Together with their properties, the fabrication of Co and Co-based alloys by means of electrochemical processes is well established making also interesting the implementation of this material in template assisted methods. In the case of nanowires arrays growth into the pores of a porous anodic alumina membrane (PAAM) used as a template, Co has been extensively employed in order to introduce an additional anisotropy of crystalline origin which may reinforce or compete against the nanowire shape anisotropy. Particularly, Co-Cu alloy shows different magnetic behaviors depending on the composition as well as the fabrication procedure. In principle, Co-Cu forms a granular alloy since Co and Cu are poorly miscible. In this case, the formation of ferromagnetic clusters embedded in a non-magnetic and conductive matrix makes this system interesting especially in applications based on giant magneto-resistance [Berkowitz 1992, Xiao 1992]. In contrast, electrodeposition has been found to be a good technique to produce Co-Cu solid solutions where Cu atoms substitute Co sites forming a real alloy [Zaman 1998, Bakkaloglu 2001]. The addition of Cu distort the Co lattice parameters affecting strongly to the magnetic properties of the material becoming an additional tool to tune the overall magnetic behavior of, in the case which is concerning in this work, magnetic nanowires arrays [Karaagac 2010, Kashi 2011, Yang 2011].

In this chapter, the effects provided by the addition of different amounts of Cu into Co-Cu nanowires over the structural and magnetic properties will be study. For this purpose, several Co-Cu nanowires arrays with different compositions have been fabricated by means of an electrodeposition process. Morphological and structural analyses have been carried out through SEM, TEM/SAED and XRD techniques. Furthermore, in order to elucidate the role of Cu in the magnetic properties, room temperature hysteresis loops and FORC have been measured. In addition, several data treatments made on previous measurements as AFD, SFD and hysteresis shape plots have contributed to provide a more detailed interpretation of the different magnetization processes that take place in the different samples. Moreover, coercive field dependence

on the applied magnetic field direction with respect to the nanowires axis, also provides a valuable information concerning the physical nature of the switching magnetization processes. Finally, the magnetic properties of rich-Co nanowires show an anomalous temperature behavior that in fact is strongly modified by the Cu addition and a reorientation of the effective magnetic anisotropy can be found. Hysteresis loops measured at different temperatures have been used to study the temperature dependence of such magnetic behavior.

6.1. Fabrication and morphological characterization of Co-Cu nanowire arrays

The PAAMs used as templates have been prepared by the two step anodization method in oxalic acid under standard conditions (see chapter 3). These conditions result in a PAAM membrane with a pore diameter of around 40 nm and an interpore distance of 105 nm. The aqueous solution employed to electrodeposit pure Co nanowires was a Watts-type electrolyte, 1.07M $CoSO_4 \cdot 7H_2O$+ 0.19M$CoCl_2 \cdot 6H_20$+ 0.73M H_3BO_3, maintaining the pH=4.02 at 45ºC to avoid the boric acid precipitation. In order to fabricate the Co-Cu alloy nanowires, 0.04M $CuSO_4$ was added to the previous electrolyte as Cu^{2+} ions source. Three different samples have been prepared under the following deposition potentials, -0.75V and -1V for Co-Cu and -1V for Co nanowires arrays, measured versus an Ag/AgCl reference electrode. The electrodeposition was carried out for 10 min in all cases, obtaining long nanowires and consequently a high aspect ratio.

Transmission electron microscopy (TEM) studies were carried out in a FEI-TITAN 80-300 kV microscope operated at 300 kV in TEM and STEM (scanning transmission electron microscopy) modes. For all those characterizations, the isolated Co-Cu nanowires from the NAMs templates were dispersed in ethanol-distilled water mixture (1:1) and sonicated during 30 minutes at room temperature. The samples were deposited onto Au grids. Then, a drop of the resulting suspension was placed onto a lacey-carbon gold grid and the solvent was evaporated in ambient environment. In TEM mode, the images were acquired in a CCD camera Gatan with a digital resolution of 1K. In Figure 6.1 SEM and TEM images as well as the measured nanowires diameter dispersion are showed. The microscopy images point out the homogeneity and mechanical stability of the nanowires in both inside the pores and free standing ones. On the other hand, the

measurement of the diameter in several nanowires has result in a mean nanowires diameter of around 45 nm.

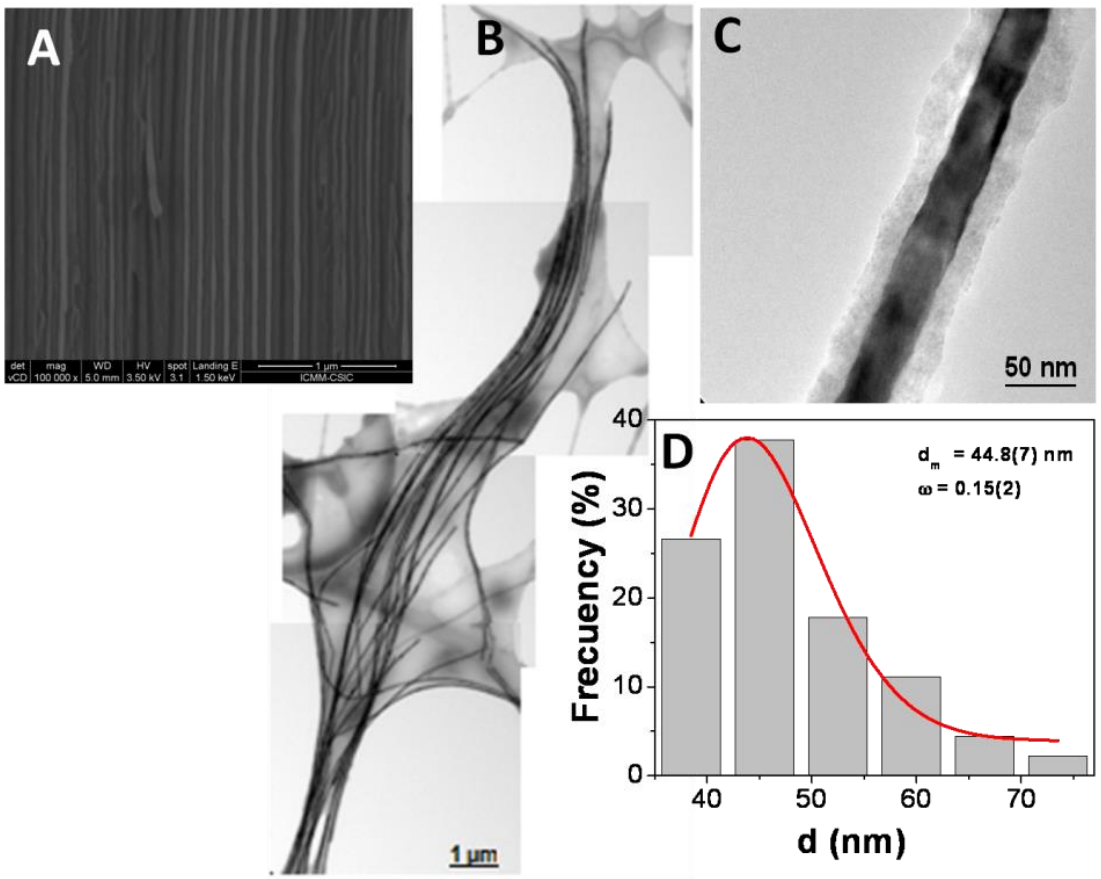

***Figure 6.1**: a) SEM cross section view of $Co_{92}Cu_8$ nanowires embedded into the pores of the AAO template, the bright colored regions correspond to the nanowires whilst dark part of the images correspond to the AAO template. b) and c) are TEM images of the same nanowires at different magnifications. d) Statistical study of nanowires diameters found that the mean value is around 45 nm.*

From SEM and EDS characterization made in the nanowires arrays, the nanowires lengths as well as the compositions are collected in Table 6.1 for the three samples investigated.

Voltage (V)	Composition	Length (µm)
-1V	Co	18
-1V	$Co_{92}Cu_8$	18
-0.75V	$Co_{73}Cu_{27}$	13

***Table 6.1**: Relative composition and nanowire length obtained for each potentiostatic voltage applied during the electrodeposition.*

However, it is worth to note that by SEM/EDS techniques it is not possible to clarify if the different elements are uniformly distributed along the nanowires. More

localized information can be obtained by high-angle annular dark-field (HAADF) technique incorporated to a STEM. This technique is strongly sensitive to the average atomic number of the material offering a mapping with compositional contrast. Furthermore, energy dispersive X-ray spectroscopy (EDS) and selected area electron diffraction (SAED) measurements were accomplished in order to gain information about the distribution of the elements and microstructure of individual Co-Cu nanowires. In Figure 6.2 it is possible to see that both Co and Cu are uniformly distributed into nanowires. In principle there is no evidences against that the Co and Ni could be alloyed in the nanowire, forming a solid solution that does not consist in a granular composition where the Cu is immersed in a Co matrix.

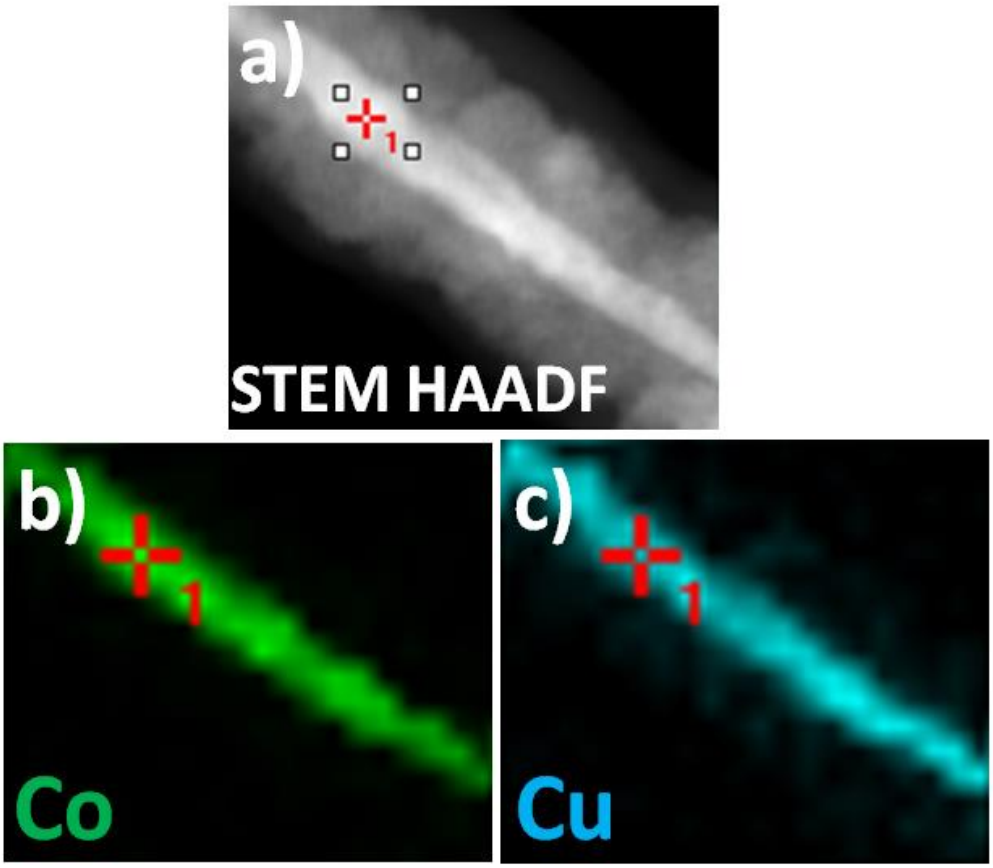

***Figure 6.2**: a) Micrograph of a single nanowire of the $Co_{73}Cu_{27}$ sample obtained by STEM operated in HAADF mode. (b-c) Elemental mapping of the same nanowire region showing the spatial distribution of b) Co and c) Cu.*

6.2 Structural analysis of Co-Cu electrodeposited nanowires

As was reflected in the previous chapter, the crystalline structure of Co can be modified, among others, by the addition of other element with a characteristic crystalline phase. Since the Cu tends to crystallize in fcc structure the phase diagram of the Co-Cu alloy can be shifted favoring the crystallization of Co in the same cubic structure. In *Figure 6.3*, XRD measurements are showed for the different samples investigated in this chapter. First of all, we will focus the structural study on the pure Co nanowires. The XRD pattern shows a clear coexistence of hcp and fcc phases. In case of the hcp one, the high intensity of the peaks related to the reflexions $(100)_{hcp}$ and $(110)_{hcp}$ together with the absence of the main peak characteristic of the hcp phase in powder diffraction, suggest a strong texture of the nanocrystals. That texture comes from a preferential orientation of the crystals growth during the electrodeposition. Moreover, the XRD pattern of Co nanowires suggests that the c-axis of the hcp phase grows perpendicular to the nanowires long axis. The main difference that can be appreciated when Cu atoms are added to the nanowires is that the amount of fcc phase grows with respect to the hcp one which indicates that Cu atoms favor the crystallization in the cubic phase. Due to the high texture it is difficult to obtain quantitative information of the relative amount of the different phases, however additional valuable information can be obtained from the XRD data. The $(100)_{hcp}$ peak is shifted to lower angles with the addition of Cu suggesting that Cu atoms substitute Co sites resulting in a deformation of *hcp-Co* structure.

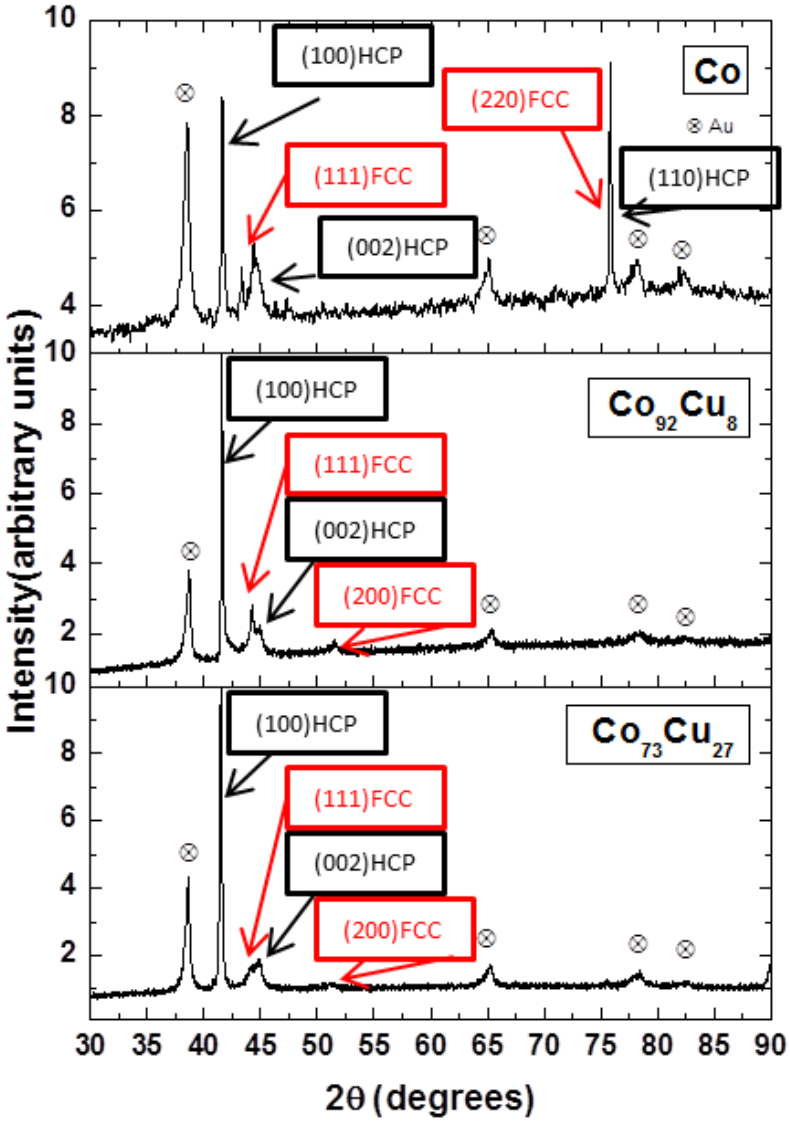

***Figure 6.3**: XRD patterns for Co (upper), $Co_{92}Cu_8$ (middle) and $Co_{73}Cu_{27}$ (bottom), with indexion of Co or Co-Cu fcc (red) and hcp (black) peaks.*

To determine more accurately the different orientations of crystals and the effect of the Cu atoms on the Co crystallization, selected area electron diffraction (SAED) measurements have been made in $Co_{92}Cu_8$ and $Co_{73}Cu_{27}$ nanowires. SAED patterns were interpreted with the Web-based Electron Microscopy Application Software: Web-EMAPS [Zuo 2004]. The electron diffraction patterns of different nanowire regions confirmed the coexistence of crystals with hcp and fcc phases in both Co-Cu samples. The microstructural analysis of $Co_{92}Cu_8$ sample is showed in *Figure 6.4* a), b) and c) while

the corresponding to the $Co_{73}Cu_{27}$ sample are presented in *Figure 6.4* d), e) and f). *Figure 6.4* b) shows the SAED pattern made on a section of the nanowire of $Co_{92}Cu_8$ corresponding to the TEM image shown in *Figure 6.4* a). Such pattern consists of slightly elongated spots, suggesting the presence of several crystals with the same crystalline phase and oriented along the same direction, but with a certain small angle of deviation. This pattern can be indexed to the [110] zone axis of a Co fcc phase or Co-Cu one. It was found that the <111> direction is next to the nanowire axis, with a deviation angle of around 7°. *Figure 6.4* c) displays a dark field TEM image obtained using the reflection (1-1-1), confirming the good crystals orientation. *Figure 6.4* e) corresponds to SAED pattern obtained from a segment of a single $Co_{73}Cu_{27}$ nanowire, whose TEM micrograph is presented in *Figure 6.4* d). This pattern can be associated to the [11-21] zone axis of a Co hcp-phase or Co-Cu one. Interestingly, the c-axis direction lies near the perpendicular direction to the nanowire axis; however, this pattern presents several remarkable peculiarities. In concrete, it is constituted by spots that tend to be accumulated forming "short lines". If the spots are elongated along the radial direction with respect the center of the SAED pattern, it means that a small distribution of lattice constants exists. On the other hand, if the spot is elongated tending to form a ring with its center coinciding to the SAED one, the distribution would lie on the crystallographic orientation. In our case, those lines appear straight or even convex with respect to the center of the SAED spectra. This indicates the presence of several nanocrystals, which tend to share the same crystallographic directions, and the presence of oriented lattice distortions in the attached crystallites, probably produced by the Cu incorporation into the Co structure. *Figure 6.4* f) represents a dark field TEM image obtained using the reflection (0-111).

Taken into account these results, we can conclude that the uniform insertion of Cu atoms in the Co structure has been achieved. Such insertion induces distortions in the crystal lattice favoring the formation of hcp crystallites attached with their [1-100] direction along the nanowire axis. Moreover, these distortions also favor the presence of fcc crystallites oriented with the [111] direction along the nanowire axis.

The distortions of the hcp lattice and the presence of fcc crystallites may reduce the contribution of the magneto-crystalline anisotropy to the effective magnetic anisotropy of the nanowires promoting a dominance of the shape anisotropy.

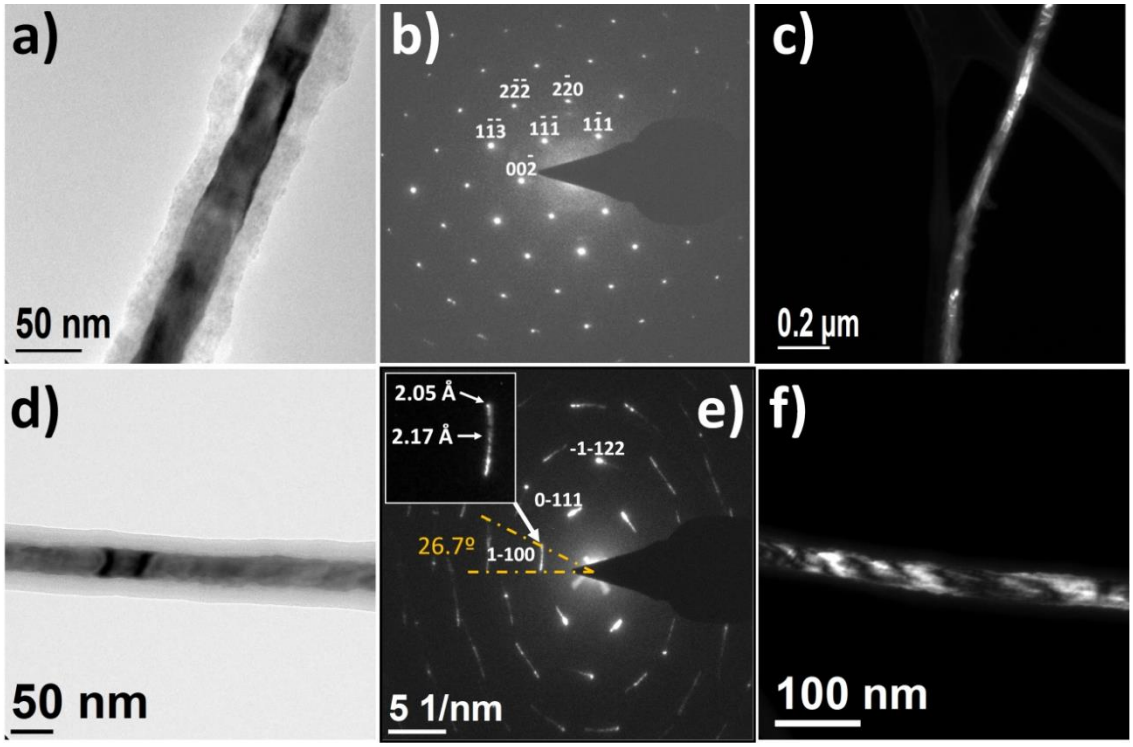

***Figure 6.4**: a) TEM micrograph made in a small region of an isolated $Co_{92}Cu_8$ nanowire. b) SAED pattern obtained in the nanowire segment of image a). c) (1-1-1) dark-field TEM image of the same nanowire. d) TEM micrograph of a segment of a $Co_{73}Cu_{27}$ nanowire. b) SAED pattern obtained for the nanowire segment of image d). e) (0-111) dark-field TEM image of the same nanowire.*

6.3 Effect of Cu content on the magnetic properties of Co-Cu nanowires arrays

6.3.1. Room temperature DC magnetization & its angular dependence

Magnetic hysteresis loops of the different nanowire arrays under a maximum field of ±1.5T have been measured at room temperature by a Vibrating Sample Magnetometer (KLA-Tencor EV7) as a function of the orientation of the applied field from parallel to perpendicular direction with respect to the nanowires axis.

From room temperature hysteresis loops, showed in *Figure 6.5* a), a clear uniaxial magnetic anisotropy with its magnetic easy axis pointing along the nanowires axis can be observed in all cases. Furthermore, the addition of Cu into the alloy increases both H_c and squareness. Taking into account what was mentioned in the structural analysis section, pure Co nanowires show an orientation of the hcp c-axis perpendicular to the nanowires axis what in principle it would result in a competition between shape and magneto-

crystalline anisotropies. However, Cu atoms favor the formation of the fcc structure, reducing the magneto-crystalline anisotropy and therefore reinforcing the uniaxial magnetic behavior dominated by shape anisotropy. In addition, $Co_{92}Cu_8$ nanowire array presents an interesting behavior with a change in the magnetic susceptibility at an applied field near the coercive one. If we pay attention on one descendant branch of the HL, the magnetization lefts the saturation nearly following the pure Co nanowires HL. As the magnetization is reaching its zero value at the coercive field its HL approaches to the $Co_{73}Cu_{27}$ one. That change on the susceptibility can be compared with what happens in the rest of the samples in such way that the softer phase could be related to the pure Co nanowire array and the harder phase with the high Cu content nanowire array. It can be seen even clearly on the SFD represented on *Figure 6.5* b). The SFD of the $Co_{92}Cu_8$ nanowire array can be seen as a sum of the corresponding SFD of pure Co and $Co_{73}Cu_{27}$ nanowire arrays.

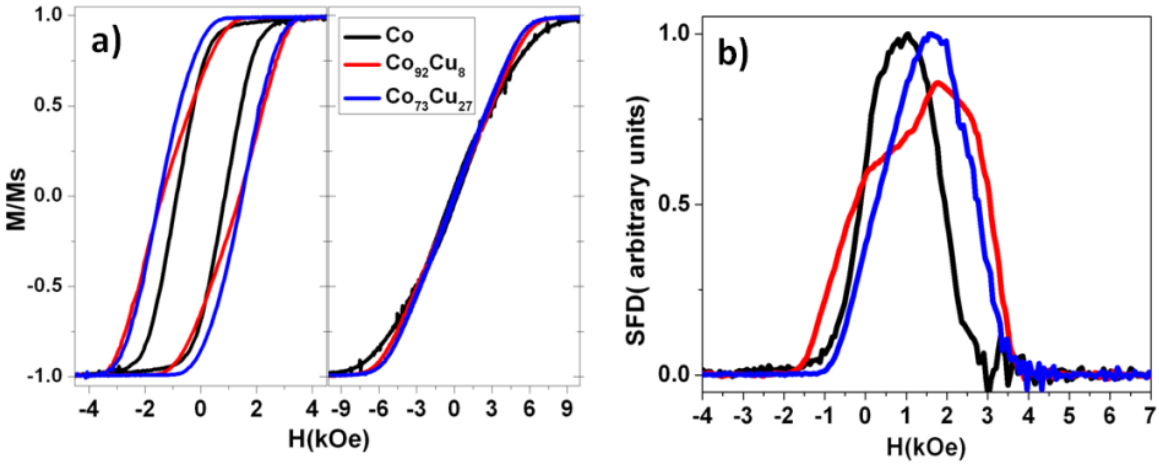

***Figure 6.5**: a) Room temperature hysteresis loops with the magnetic field applied parallel (left), and perpendicular (right) with respect to the nanowires axis. b) Switching field distribution obtained from the HL on a) for pure Co (black), $Co_{92}Cu_8$ (red) and $Co_{73}Cu_{27}$ (blue) nanowire arrays.*

The experimental angular dependence of the coercivity can be compared with its expected evolution according to analytical calculations considering three possible reversal modes, coherent rotation, and the nucleation and propagation of transverse and vortex domain walls. Although all three modes are possible in principle, the system will reverse its magnetization basically by the mode that offers the lowest coercivity, or in other words, by the process that needs the lower energy to be produced. To obtain a good agreement with experiments an out-of-plane magneto-crystalline anisotropy has been

considered in the calculations. Regarding the lack of perfect fitting it is important to note that the model does not consider inter-element interactions with surrounding wires. Nevertheless, if we assume that the interactions among nanowires are soft enough and they can be treated as a mean interaction field proportional to the magnetization, as was already discussed, the effect of the interactions to the coercive field can be negligible.

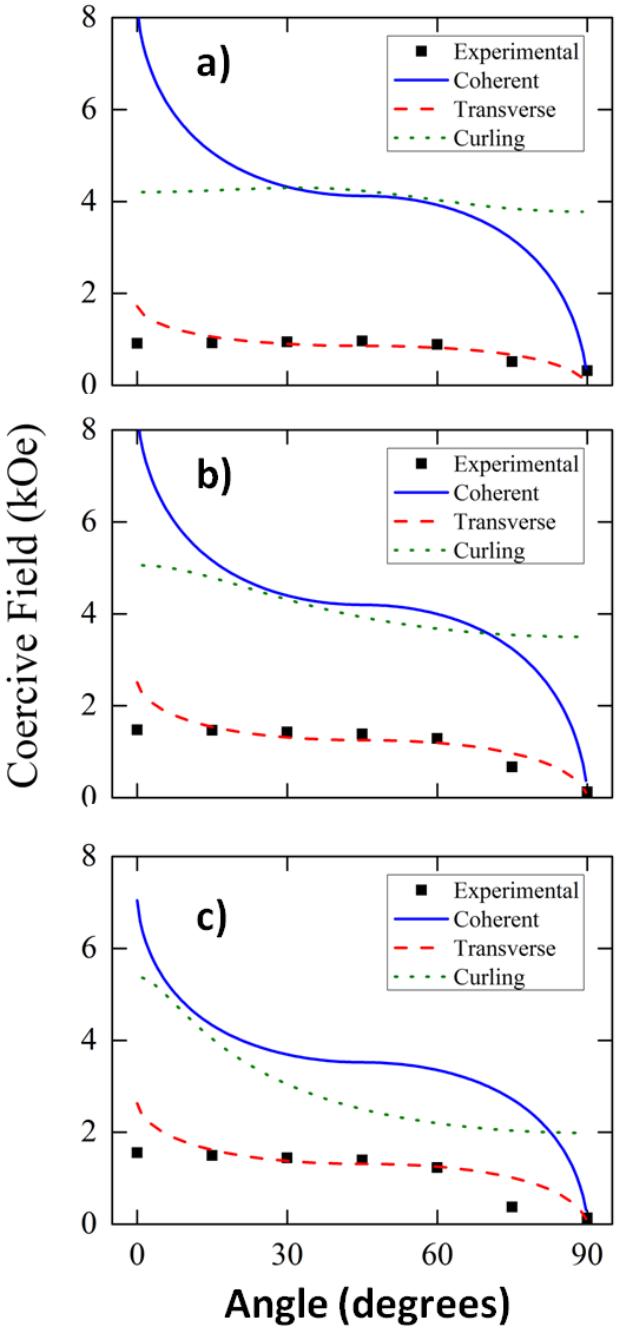

Figure 6.6*:Experimental and calculated coercivity for a) Co ($K_{mc} = -3.7 \times 10^4 J/m^3$); b) $Co_{92}Cu_{08}$ ($K_{mc} = 2.1 \times 10^4 J/m^3$) and c) $Co_{73}Cu_{27}$ ($K_{mc} = 3.3 \times 10^4 J/m^3$) nanowires as a function of the angle between the applied magnetic field and the long nanowires axis.*

Figure 6.6 a), b) and c) illustrate the experimental results for the three compositions together with the calculated data according to the three reversal modes for a nanowire length of 15 μm. In the figure caption, the different values of the crystalline anisotropy constant (K_{mc}) used in calculations in order to obtain the best agreement with experimental results are indicated. As it is observed, in all cases the magnetization reversal is driven by the nucleation and propagation of a transverse domain wall, so in principle the difference in the value of Hc arises from the change in the effective magnetic anisotropy instead of the type of reversal process. A comparison among the three samples on both the reduced remanence and the coercive field behaviors with respect to the angle formed by the nanowires axis and the applied magnetic field are plotted in *Figure 6. 7* d) and e). Interestingly, in terms of the coercive field, the sample $Co_{92}Cu_8$ follows the same behavior as the Cu-richer one while in the case of the reduced remanence occurs the opposite. This suggests that at least near the magnetization easy axis the coercive field is established by the harder phase while the remanence is controlled mainly by the softer phase. This is in accordance with what has been discussed before, where the sample $Co_{92}Cu_8$ seems to show two different behaviors with two different contributions of a pure Co-like phase and another Cu-richer phase.

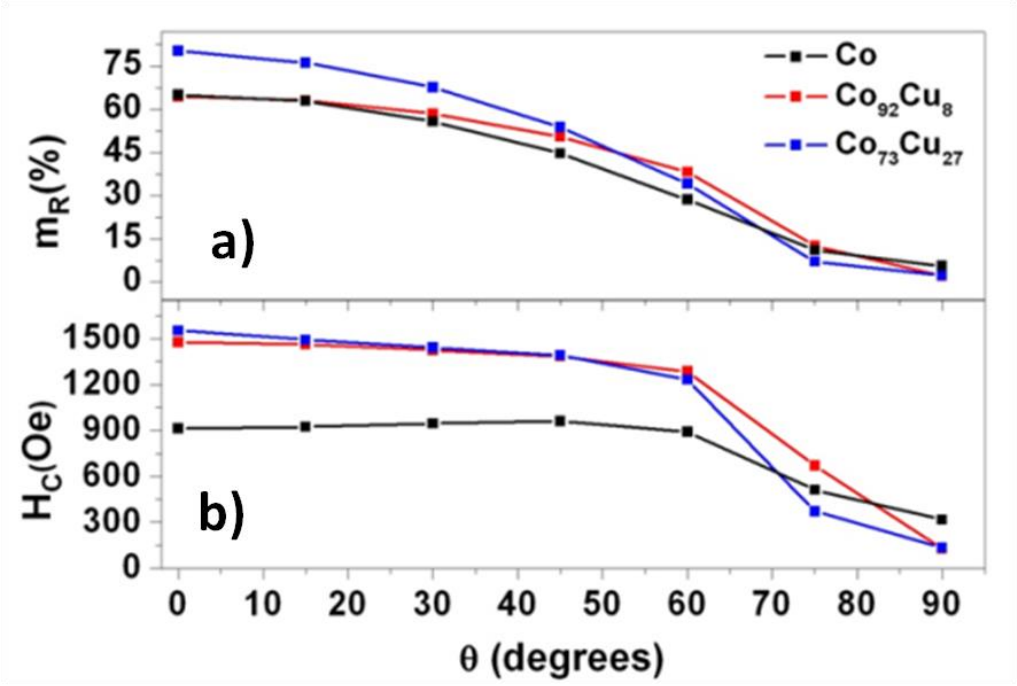

Figure 6. 7*: Comparison of reduced remanence a) and coercive field b) angular dependence among the three samples (Co in black, $Co_{92}Cu_8$ in red and $Co_{73}Cu_{27}$ in blue).*

Figure 6.8 collects the evolution of the magneto-crystalline anisotropy constant as deduced from the fitting of experimental and calculated data. From this figure we observe that the easy axis evolves from perpendicular (in the plane of the membrane) in the case of Co to longitudinal (parallel to the wire axis) in the case of Cu-rich alloy nanowires. This fact is in agreement with the formation of the fcc structure when Cu is added into the alloy, as it has been discussed in previous sections.

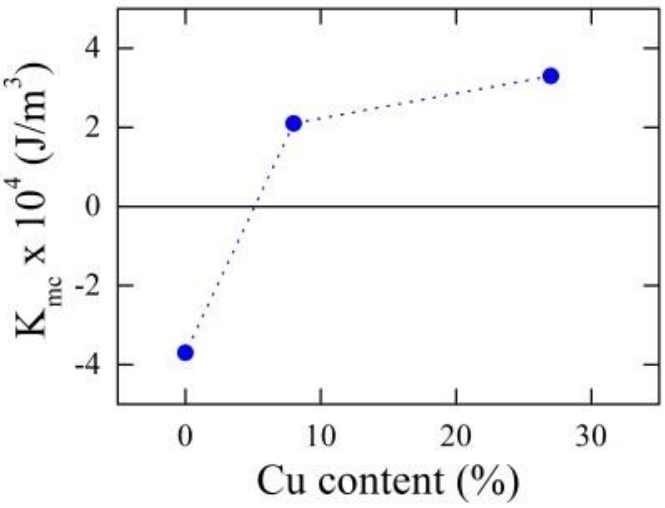

***Figure 6.8**: Evolution of the magneto-crystalline anisotropy constant, obtained from the fitting of experimental and calculated data, as a function of the Cu atomic content in the alloy.*

The study of the anisotropy field distribution, *AFD*, is a useful tool to determine the magnetic anisotropy and the parameters that influence the effective anisotropy field (H_{eff}) of a magnetic system [Barandiaran 1989, De La Torre Medina 2009]. This method for the anisotropy field evaluation makes use of the descendant branch analysis in the hysteresis loop from the magnetization saturation state to zero applied magnetic field measuring in the hard magnetization configuration which, as was mentioned above, corresponds to an in-plane direction with respect to the membrane, perpendicular to the nanowire axis. From the corresponding hysteresis loops, the anisotropy field distribution (σ) is obtained as:

$$\sigma = -H \frac{d^2}{dH^2} < m(H) > \qquad \textbf{(6.1)}$$

The distributions of the anisotropy field for the studied samples are collected in *Figure 6.9*, from which an effective uniaxial anisotropy field (H_K) is determined as the maximum of each anisotropy field distribution. With an ideal uniaxial magnetic

anisotropy, the AFD measured along the hard axis should be a narrow peak centered at H_K. The deviation of the effective magnetic anisotropy from the nanowires axis produces a broadening and a shift of the AFD along the perpendicular direction due to, in fact, this direction is no longer the hard axis. As it has been discussed above, Co-base nanowire arrays exhibit a significant magneto-crystalline anisotropy that mostly determines the magnetization easy axis of nanowires. In the present case, a texture $(100)_{hcp}$ can be assumed with an in-plane magnetization easy axis as was discussed in the XRD analysis. The evolution of the AFD with respect to the amount of Cu that is present into the alloy points out once more the reduction of the magneto-crystalline anisotropy and thus the competition between the different anisotropies as the peaks are becoming narrower in richer Cu nanowires.

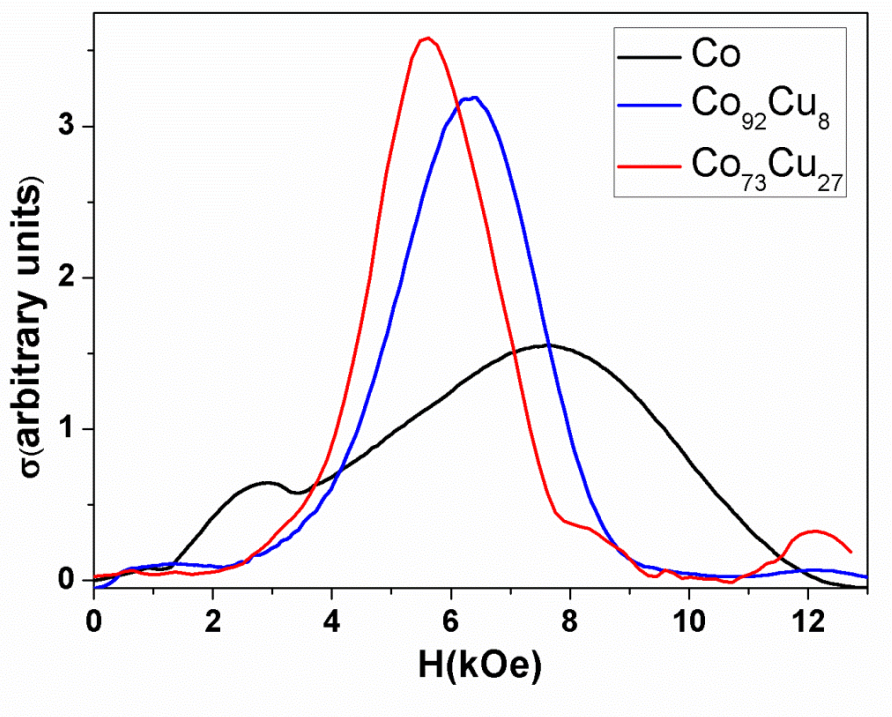

Figure 6.9: *Anisotropy field distribution calculated from the hysteresis loops measured along the hard magnetization axis (perpendicular to the nanowires axis), for Co (black), $Co_{92}Cu_8$ (blue) and $Co_{73}Cu_{27}$ (red) nanowire arrays.*

6.3.2 MAGNETIC CHARACTERIZATION BASED ON FORC

The FORC analysis made on the three nanowire arrays (see *Figure 6.10*) along the nanowires axis gives valuable information about magnetization processes and interactions that are taking place inside the materials when it is magnetized. In the case of Co and

$Co_{73}Cu_{27}$ nanowire arrays the typical "wishbone" shape characteristic of an interacting system can be observed. The main difference between them has already been displayed in the HL, i.e., the harder magnetic behavior of the $Co_{73}Cu_{27}$ nanowires. The values of H_C^{forc} extracted from the FORC profiles at Hu=0 reveal a coercive field of 826 Oe and 1513 Oe for the pure Co and $Co_{73}Cu_{27}$ nanowire arrays, respectively. However, this is the only difference between them since the standard deviation of the SFDs, as well as the strength of the interaction field at saturation (α) are the same in both cases, around 260 Oe and 1650 Oe, respectively. Therefore, it is reasonable to think that these previous parameters are mainly ascribed to the characteristics of the membranes used as templates. In the first case, the standard deviation could be a product of a distribution of different pore diameters produced during the anodization.

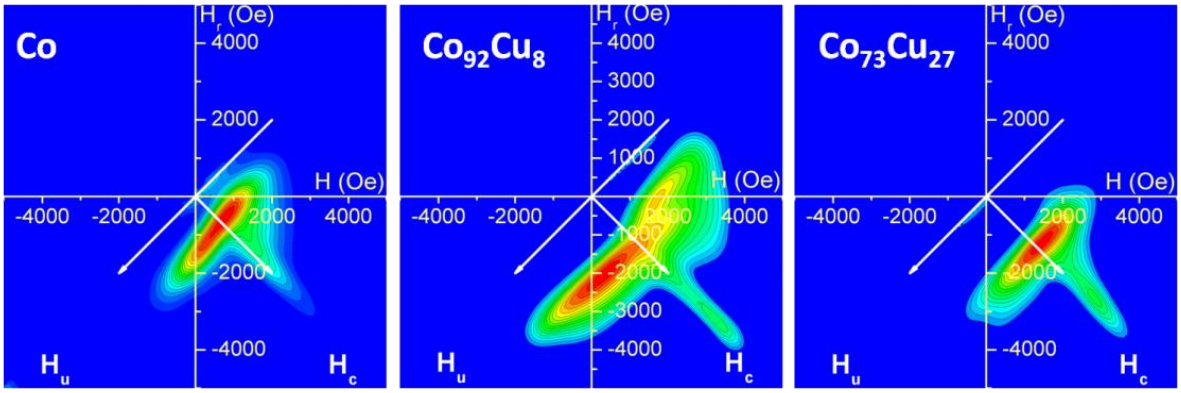

***Figure 6.10**: FORC diagrams corresponding to the parallel direction with respect to the nanowires axis for Co (left), $Co_{92}Cu_8$ (center) and $Co_{72}Cu_{27}$ (right).*

The FORC diagram for the $Co_{92}Cu_8$ sample shows a more complex behavior. Two different distributions are clearly observed both very close to each other. The main distribution shifted to negative values of Hu is centered at the same value of coercive field as the sample $Co_{73}Cu_{27}$, while the one shifted to positive values of Hu corresponds to the coercive field of the pure Co nanowire array. The fact that both distributions are shifted along the interaction field axis suggests that both distributions are submitted and contribute to the same mean field interaction. In this scenario, the softer phase should reverse its magnetization before the harder one, where the net magnetization is still positive and then the interaction field shifts the hysterons to higher magnetic fields moving the whole distribution along the positives values of Hu. In the same way, the main part of the harder distribution reverses where the magnetization is negative and then the shift of the hysterons is along the opposite direction. However, the FORC diagram

for the $Co_{92}Cu_8$ sample is not a result of the sum of the pure Co and $Co_{73}Cu_{27}$ FORC diagrams. Neither the individual FORC distributions keep their shape, i.e., they are not only shifted by the interaction field but rather the distribution shape is modified what suggest that some different magnetic effects are taking place. If the assumption in sample $Co_{92}Cu_8$ that there are two different magnetic phases into the alloy was correct, it is reasonable to think that the system is a hard magnetic phase embedded in a soft magnetic one, or vice versa, both coupled by exchange. In this case, if after magnetization saturation the applied magnetic field is decreased, the soft magnetic phase should reverse its magnetization first. However, since both phases are exchange coupled, the hard magnetic phase retains the switching of a portion of the soft one at the interface until the hard magnetic phase is reversed. Previous comments are consistent with the fact that the reduced remanence is mainly ascribed to the softer magnetic phase while the coercive field is a consequence that some part of softer magnetic phase is pinned by the hard one through the exchange coupling between both.

6.3.3. TEMPERATURE INFLUENCE ON THE MAGNETIC ANISOTROPY

The temperature dependence of hysteresis loops has been measured in a VSM-Versalab (Quantum Design) in both configurations of the applied magnetic field, parallel and perpendicular to the nanowire axis in the range of 50-400 K under a maximum applied magnetic field of ±3T. *Figure 6.11* shows the temperature dependence of longitudinal coercivity (H_c), and reduced remanence (m_R). An increase of both coercivity and remanence with increasing temperatures is observed, which leads to a higher uniaxial effective magnetic anisotropy with the easy axis along the nanowire axis. This is in principle an unexpected behavior since the thermal activation should reduce the effective magnetic anisotropy so then magnetic moments should be more stable at lower temperatures. It is important to note that the temperature variation modifies the stresses on material, since nanowires are embedded in an alumina matrix with a different thermal expansion coefficient. On cooling, the nanowires tend to contract faster than the pore of the membrane giving rise to a tensile stress perpendicular to the nanowire axis. However, the low saturation magnetostriction of polycrystalline Co ($\lambda_S \sim -62 \times 10^{-6}$) would not be sufficient to induce such strong effect with temperature, i.e., due to the tensile stresses [Srivastav 2014]. Moreover, the negative sign of the magnetostriction coefficient would result in a decrease of the magnetoelastic energy with the magnetization pointing along

the perpendicular direction with respect to the tensile stress direction. In other words, the increase of the tensile stress along the radial direction of the nanowire, as the temperature decreases, would result in a magnetization easy axis along the nanowire axis that is the opposite to what is observed in the studied samples.

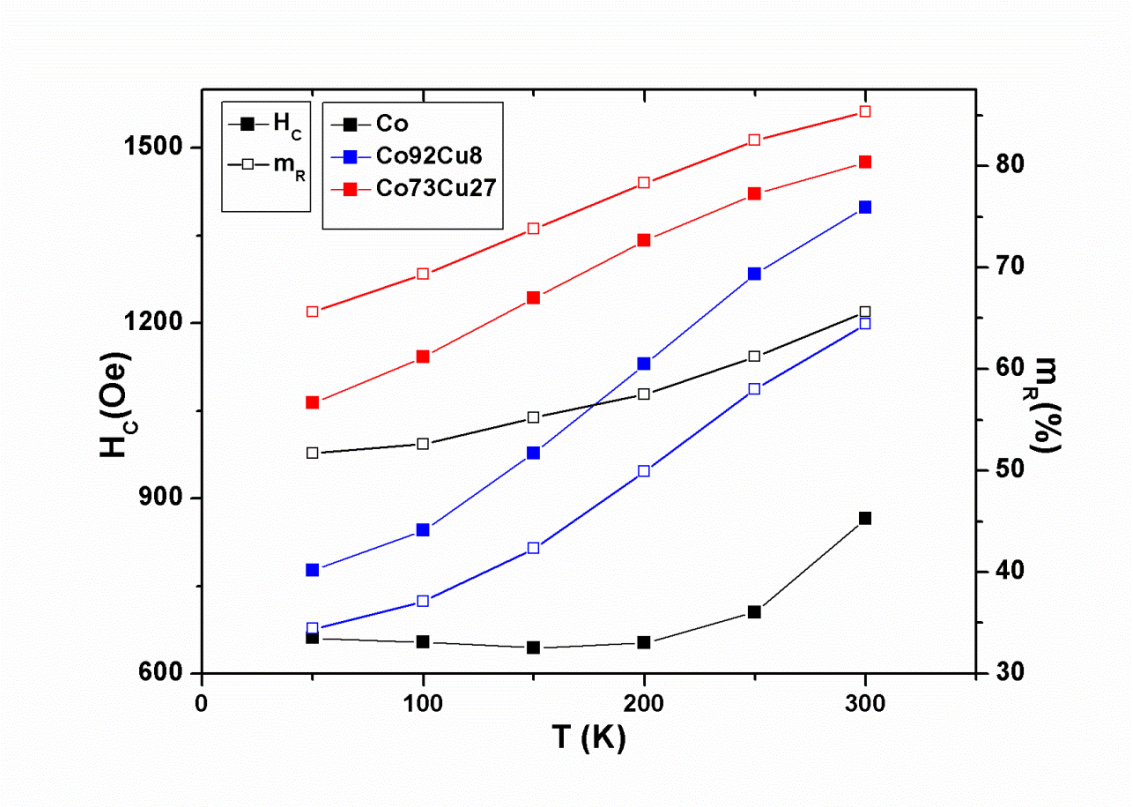

***Figure 6.11**: Temperature dependence of longitudinal H_c (close squares) and $m_R(\%)=M/Ms\cdot100$ (open squares) for Co (black), $Co_{92}Cu_8$ (blue) and $Co_{73}Cu_{27}$ (red) nanowire arrays.*

Furthermore, in some reports, the temperature dependence of the magneto-crystalline anisotropy has been proposed to be the responsible of the temperature reorientation of the effective magnetic anisotropy [Callen 1966, Silva 2006, Srivastav 2014]. In this case, the uniaxial hcp structure should have the strongest effect due to its temperature dependence. The *AFD* analysis for Co-Cu nanowires at different temperatures is shown in *Figure 6.12*. For both Co-Cu alloys, with decreasing temperature we observe a broadening of the anisotropy distribution together with a moderate reduction in the longitudinal anisotropy field. That correlates well with the observed reduction of longitudinal coercivity and remanence as the temperature decreases. In short, we should assume a competition between shape anisotropy and magneto-crystalline anisotropy.

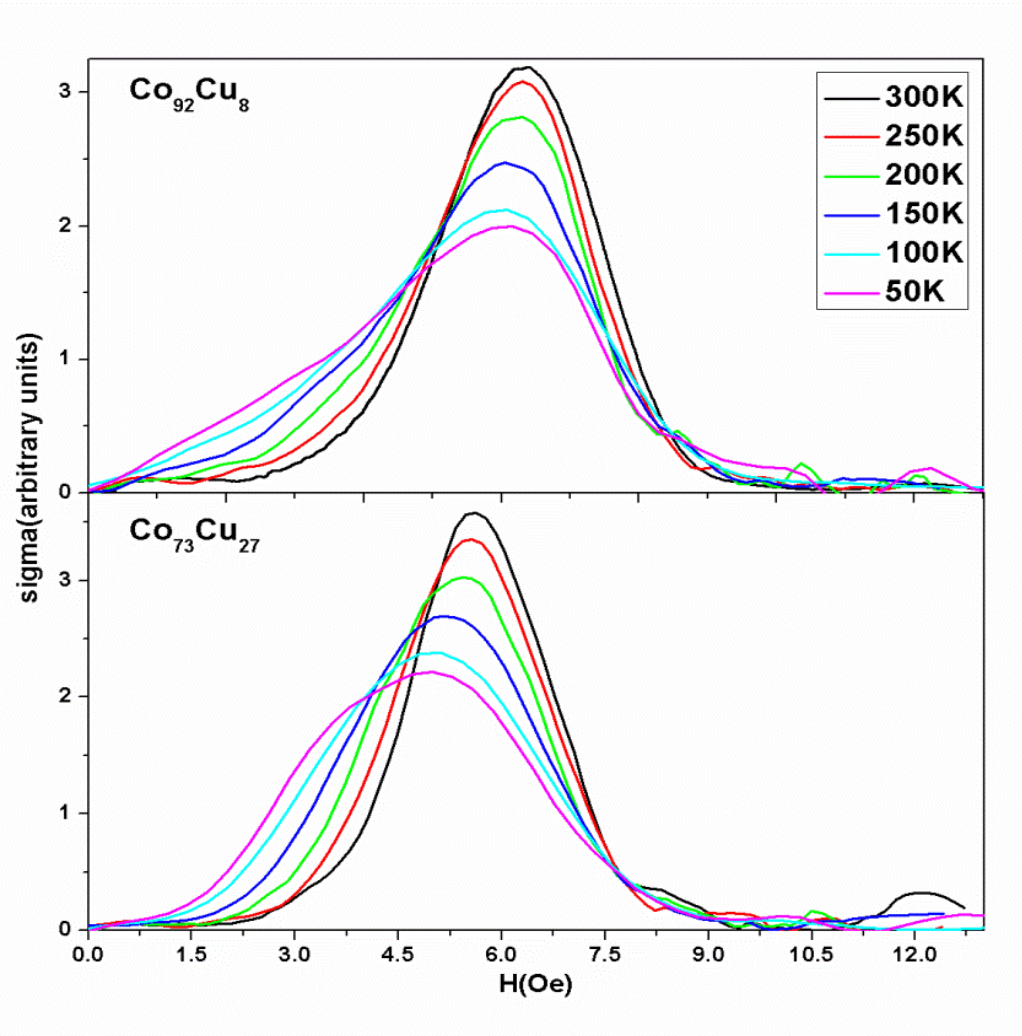

***Figure 6.12**: Temperature dependence of the anisotropy field distribution for $Co_{92}Cu_8$ (up) and $Co_{73}Cu_{27}$ (down) nanowire arrays.*

However, is important to note that the largest effects on H_C and m_R due to the temperature variation are displayed by $Co_{92}Cu_8$ nanowires where a not negligible reduction of the hcp phase exists. As it was mentioned above, the $Co_{92}Cu_8$ shows a clear two different contributions coming from a pure Co-like and $Co_{73}Cu_{27}$-like phases. The coercive field dependence on temperature for the $Co_{92}Cu_8$ sample shows that at room temperature the largest contribution comes from the harder phase $Co_{73}Cu_{27}$ whilst reducing the temperature the coercive field is more influenced by the softer phase of pure Co. In terms of the saturation field defined as the minimum field necessary to saturate a magnetic material along a given direction, *Figure 6.13* shows that, actually, the anisotropy field measured along the nanowire axis only has the expected temperature dependence, in terms of the magneto-crystalline anisotropy increasing along the perpendicular direction with increasing temperatures, in the case of pure Co nanowires. In fact, pure Co

nanowires undergo a reorientation of the effective magnetic anisotropy through an increase of the magneto-crystalline anisotropy along the perpendicular direction with respect to the nanowires axis. However, both $Co_{92}Cu_8$ and $Co_{73}Cu_{27}$ (not shown in the figure) show a constant anisotropy field over the temperature and moreover it is centered at the same value in both cases. This could be a sign that the last switching field before saturation correspond to the harder phase of Cu-rich composition present in both alloys but in different ratios with respect to the pure or rich and softer Co phase. Furthermore, this harder phase would show negligible temperature dependence what would fit with the assumption that the harder phase (high Cu content) should be correlated with the fcc crystalline structure.

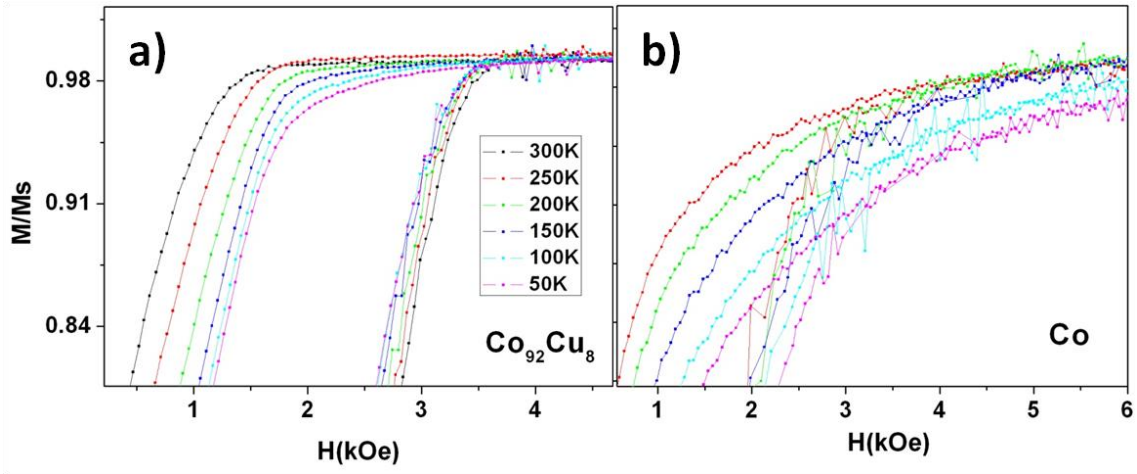

Figure 6.13: *Detail of saturation magnetization zone of hysteresis loops measured at different temperatures for the three samples, $Co_{92}Cu_8$ (left), $Co_{73}Cu_{27}$ (center) and pure Co (right) nanowire arrays.*

6.4. SUMMARY AND CONCLUSIONS

Co and Co-Cu nanowires have been electrodeposited into the pores of alumina templates anodized in oxalic acid under standard conditions. By $CuCl_2$ addition to the Co Watts-type electrolyte and varying the electrodeposition voltage, the amount of Cu into the Co-Cu nanowires has been tuned. In order to study the effect of Cu in the crystalline structure of Co deposits, XRD characterization has been performed in all samples. Pure Co nanowires present a mixture of fcc and hcp crystalline phases, being the last one the main phase with its c-axis along the perpendicular direction with respect to the nanowire axis. However, as soon as the Cu is present into the nanowire the fcc phase fraction tends to increase proportionally with the amount of added Cu. TEM/SAED and EDS

characterization have corroborate XRD results and have pointed out that Cu is homogeneously distributed along the nanowire. Moreover, some interesting SAED spectra have been obtained in richer Cu nanowires where there is a distortion of the Co lattice in a very specific that needs further studies to evaluate such a complex crystal structure and how Cu concerns this distortion.

Hysteresis loops indicate, that all the nanowire arrays present a well-defined uniaxial magnetic anisotropy with the magnetization easy axis pointing along the nanowire axis. Comparing the corresponding hysteresis loops for the different alloy nanowire arrays, the coercive field and squareness both increase as the amount of Cu increases in the alloy. Furthermore, the composition with lower amount of Cu, $Co_{92}Cu_8$, presents two clearly different irreversible magnetization reversal processes which suggest that two ferromagnetic phases are present in the sample. In addition, the magnetically softer phase would correspond to a pure-Co like nanowire array whilst the harder one could be ascribed to a Co-Cu phase. FORC measurements have also displayed two different irreversible reversal magnetization processes in the case of the $Co_{92}Cu_8$ nanowire array. In principle, the resulting FORC diagram does not correspond to two independent SFD suggesting that additional interaction effects between both ferromagnetic phases play an important role in the magnetic behavior of the sample.

The temperature dependence of magnetic hysteresis loops has been studied in all samples. The increase of both the coercive field and reduced remanence with increasing temperatures has been ascribed, according to the literature, to a reduction of the magneto-crystalline anisotropy of Co-hcp phase as the temperature is increased, promoting a higher uniaxial effective magnetic anisotropy. However, as far the hcp phase is reduced with the addition of Cu, it is in principle peculiar that the strongest effect of temperature on the effective magnetic anisotropy has been found in the $Co_{92}Cu_8$ nanowire array. Moreover, this sample presents two different ferromagnetic behaviors, suggesting that the temperature dependence of coercivity could be increased by a change in the interaction features which could be affected by the differences between switching fields associated to respective magnetization reversal process in each phase.

7. MAGNETIC NANOWIRES EMBEDDED IN CYLINDRICAL POROUS ALUMINA TEMPLATES.

Porous anodic alumina membranes (PAAMs) have been extensively used for the fabrication of magnetic nanowires with many different compositions as was reflected in previous chapters. In some cases PAAMs serve only as a template for the massive fabrication of a wide kind of nanomaterials, where after the fabrication, the PAAM is removed and does not take part on the final application. In case of nanowires, when the PAAM is removed, a solution with free standing nanowires is obtained, which has been extensively employed in electronic, photonic, energy and biological based applications [Mikkelsen 2013, Yang 2010, Hochbaum 2010]. Sometimes cases the PAAM can be required itself by a certain application due to its unique ordered nanoporous arrangement. In this sense, PAAMs are good candidates for research in new high density recording media and different devices and sensors employed on electronics [Sellmyer 2001, Pan 2005, Meng 2005]. Particularly, magnetic nanomaterials for sensors based on magneto-resistance (MR) and magneto-impedance (MI) effects are extensively studied [Phan 2008, Ren 2010]. Both effects relate the magnetic state of the material with an applied dc or ac electrical current flowing through it, respectively. In the MI effect, depending on the frequency value of the ac current, such current can be confined close to the material surface what is commonly called “skin effect” [Valenzuela 2002]. Even if the material is or not magnetic, the presence of a magnetic material near the surface can affect to the diffusion of the electrical current trough the not magnetic conductor. One possibility to prepare such materials can be found in [Zhang 2012]. The electrodeposition of magnetic nanowires into a PAAM and the subsequent deposition of a magnetic layer on top of the membrane, results in a heterogeneous material where all the nanowires are perpendicularly orientated with respect to the plane of the deposited film. However, the planar geometry of the membrane does not allow the covering of the entire surface of the film with magnetic nanowires which makes interesting to develop new PAAMs with different macroscopic geometries. All of these PAAMs have been prepared using a high pure Aluminum foil, which introduces the final planar geometry of the membrane. Recently the use of a cylindrical geometry as the starting Al substrate in the anodization

process has been found to be a valuable method for the development of new PAAMs [Sanz 2007]. The geometry of the template described in this reference, is determined by a high purity Al wire producing a cylindrical porous anodic alumina membrane (CPAAM). This kind of sample leads to 3-D spatially distributed nanowires that can be very interesting for applications based in MI among others magneto-transport effects, electromagnetic filters at microwave antennas, magnonics, etc.

In the following chapter the effective anisotropy of magnetic nanowires arrays with different compositions synthesized by pulsed electrodeposition into the CPAAM templates will be studied. Furthermore, the effect of the change in the membrane geometry on the collective magnetic behavior of the entire nanowire array will be discussed. In order to evaluate such influences, a comparison between CPAAM and PAAM nanowire arrays fabricated under the same conditions has been performed.

7.1. FABRICATION OF THE CPAAM TEMPLATES

The CPAAMs have been fabricated trough the anodization of high purity Al wires (99.999%) with 1.5 mm of diameter. Essentially, the anodization process is the same as was explained in case of planar PAAMs. First of all, the Al wire is subjected to a cleaning process consisting of a sequentially immersion of the sample substrate into isopropanol and ethanol while it is ultrasonicated. Then, the wire surface is electropolished in a bath composed by a mixture of perchloric acid and ethanol with a proportion of 1:3 in volume under an applied voltage of 20V with the Al wire set as the anode. In order to obtain a reduced surface roughness, 2 minutes of electropolishing were performed in all cases. However, the anodization set-up described in chapter 3 had to be properly modified in order to be adapted to the new geometry of the Al substrate. A schematic draw of the new set-up can be found in *Figure 7.1:*. One of the main differences with respect to the set-up presented in chapter 3 lies on the fact that now the electrolyte is cooled by a double jacket beaker where the cooling liquid from the cryostat is passed through its walls. The first and second anodization processes have been carried out in 0.3 M oxalic acid under standard conditions (20 V at 1-3 ºC). The Al wires were anodized first for 24 h and subsequently immersed in $(0.18M\ CrO_3 + 0.61M\ H_3PO_4)$ at 45ºC for 12 hours to remove the disordered aluminum oxide layer formed during the first step of anodization. The second anodization has been maintained for 1 h resulting in a CPAAM with around 2.5 μm of

thickness. Due to the geometry of the starting material, it is not possible, in this case, to remove the remaining Al wire in order to expose the bottom side of the oxide layer and open the pores of the CPAAM of that side. Fortunately, the barrier layer can be further reduced, via thinning barrier layer process during which dendrites are formed through the oxide layer until a direct contact with the conductive Al substrate is achieved. The reduction of the barrier layer can be performed by a stepwise reduction of the anodic voltage down to 4.5V. In order to better understand the magnetic behavior of the cylindrical arrangement of nanowires, planar PAAM membranes were also prepared under the same conditions as the circular ones and employed as a reference sample for each kind of composition.

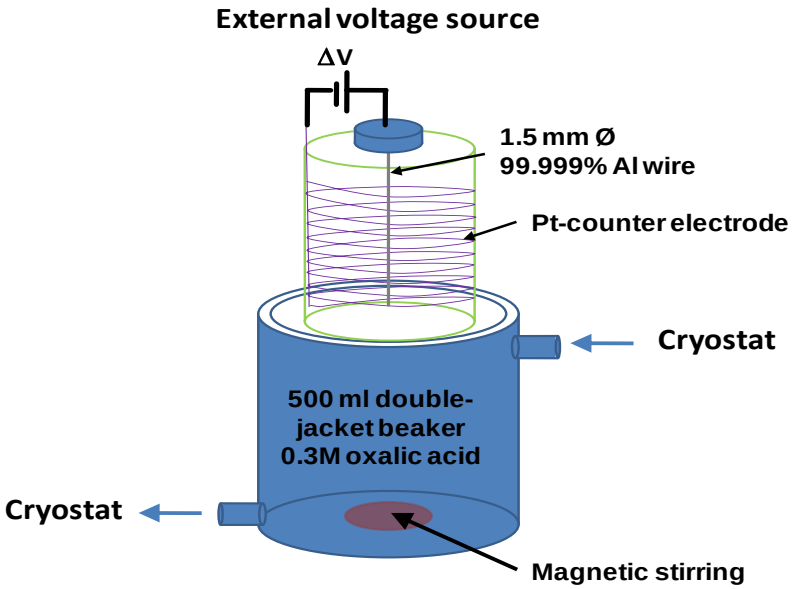

***Figure 7.1**: Schematic drawing of the experimental set-up employed in the fabrication of the CPAAM. The system consists in a double jacket beaker and a cryostat for cooling and Pt wire as the counter electrode. The electrolyte is magnetically stirred in order to homogenize its temperature during the anodization.*

7.2. MAGNETIC NANOWIRES ELECTRODEPOSITION

In this study, Co, Ni and Co-Ni nanowires have been electrodeposited using the CPAAM and the planar PAAM as templates. The electrolyte employed for the electrodeposition of each composition is shown in *Table 7.1*. The pH of the electrolyte was maintained around 4 and the temperature of the process was kept to 45ºC and 66ºC

for (Co, Ni) and Co-Ni alloy, respectively, in order to avoid the boric acid precipitation. Due to the presence of the barrier layer, it is not possible to carry out the electrodeposition process under pure potentiostatic or galvanostatic conditions. The insulating barrier layer acts as a capacitor during the process collecting charges on both sides and hindering or even interrupting the electrodeposition. For this reason it is necessary to use a pulsed electrodeposition sequence where with a deposition pulse and a period in "off" where the barrier layer is discharged to allow the deposition in the next pulse. The electrodeposition conditions were chosen to be the same in all cases. The process consisted in galvanostatic pulses corresponding to a current density of around 38 mA/cm^2 in all cases. The time duration of the process was 30 minutes which resulted in nanowires length of around 2.5 μm almost entirely filling the templates.

	Concentration in the electrolyte (g/l)		
Salt	**Co**	**Co-Ni**	**Ni**
$CoSO_4 \cdot 7H_2O$	300	150	
$NiSO_4 \cdot 6H_2O$		150	300
$CoCl_2 \cdot 6H_2O$	45	22.5	
$NiCl_2 \cdot 6H_2O$		22.5	45
H_3BO_3	45	45	45

***Table 7.1**: Summary table of the electrolyte concentration employed in the electrodeposition of different alloyed nanowires.*

In *Figure 7.2* several SEM images of the same sample are collected at different magnifications to distinguish the each part of the CPAAM nanowire arrays. In *Figure 7.2* a), the Al wire after the two step anodization process can be observed. In turn, in *Figure 7.2* b) the Al wire was a bit bended in order to break the anodic aluminum oxide layer growth on top. Finally, the top view (*Figure 7.2* c)) as well as the cross section (*Figure 7.2* d)) of the membrane reveal the presence of nanowires and the large dispersion of nanowires length where at some points a small overgrowth have been observed.

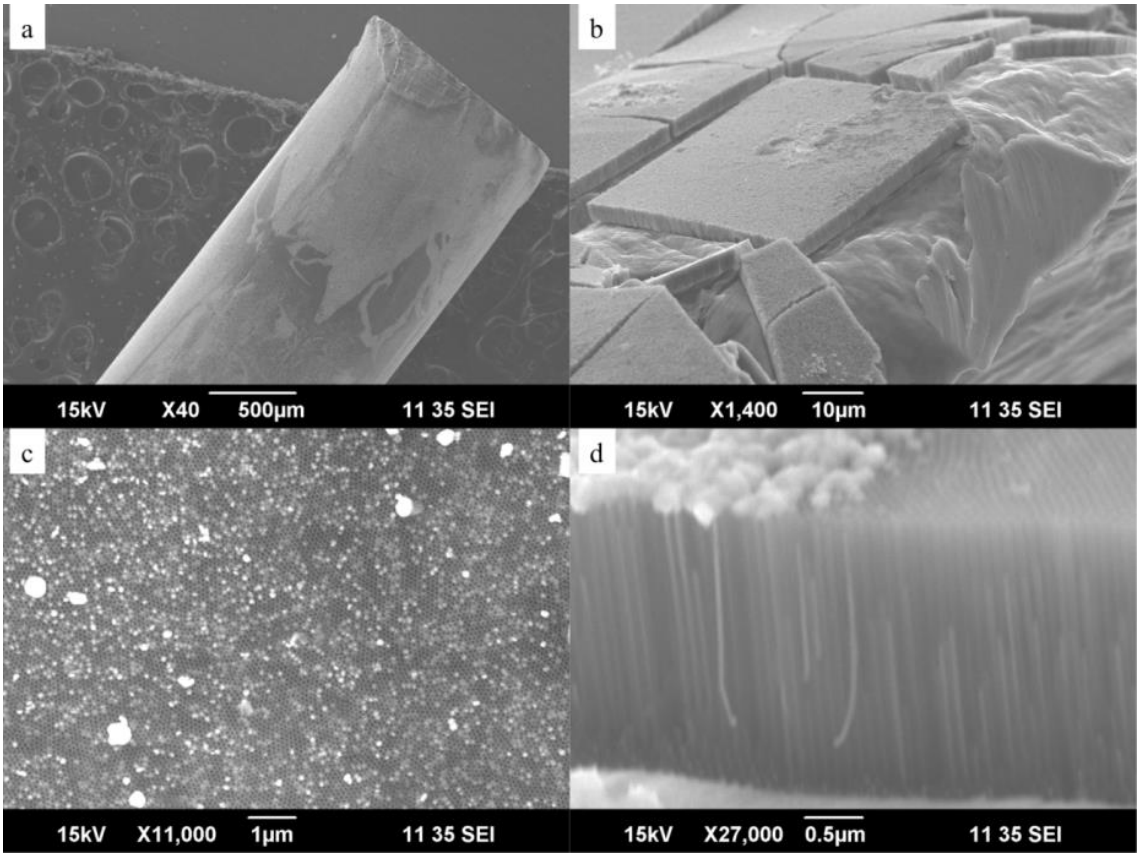

***Figure 7.2**: SEM images of a) Al wire substrate, b) Al wire substrate where the PAAM on top is clearly evidenced, c) top view and d) cross section of the CPAAM nanowire array.*

7.3. MAGNETIC PROPERTIES OF CPAAM NANOWIRE ARRAYS: COMPARISON WITH PLANAR NANOWIRE ARRAYS.

The magnetic characterization has been carried out by dc magnetometry at room temperature along two perpendicular applied magnetic field directions. However, due to the different geometry of the two kinds of samples, it is necessary to establish a common reference system for the different applied field directions of magnetization measurements for each sample. Those directions of the applied magnetic field are shown in *Figure 7.3* to facilitate the following comparison between the samples. The planar arrays are most homogeneous case, since the directions can be referred to the magnetic material, i.e. parallel or perpendicular with respect to the nanowire long axis. In contrast, the applied field directions in CPAAM nanowire arrays are better defined with respect to the Al wire substrate, where the axial direction is perpendicular to all the nanowires whilst the radial direction covers all the possible orientations between the applied magnetic field and each nanowire axis.

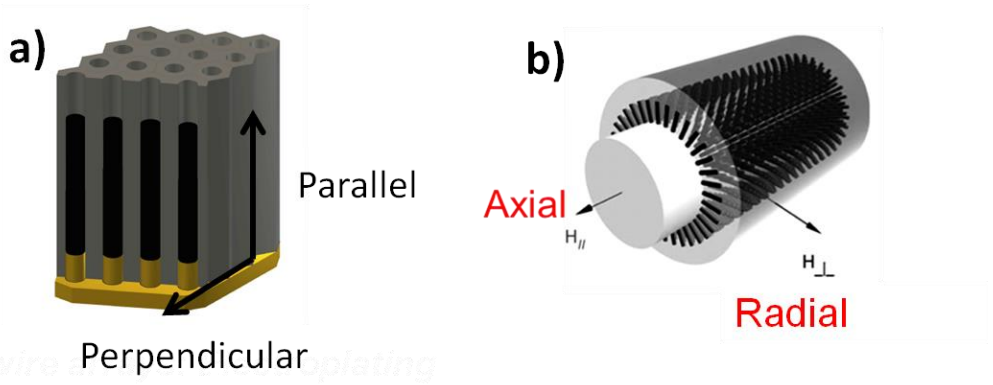

***Figure 7.3**: References for the different applied field directions for measuring the magnetization in a) planar PAAM and b) CPAAM nanowire arrays.*

First of all, let us start with the magnetic characterization of the planar PAAM nanowire arrays where the measurement orientations are referred to the magnetic nanowires. The room temperature HLs for different nanowire compositions are showed in Figure 7.4. The Ni nanowire planar array presents the most clear uniaxial magnetic anisotropy as can be concluded from the values of coercive field and reduced remanence along the two different directions collected in *Table 7.2*. Furthermore, the magnetization easy axis of such array lies along the parallel direction with respect to the nanowire long axis. However, in case of pure Co or Co-Ni nanowire arrays, the presence of an anisotropy component along the perpendicular direction is evidenced. In previous studies [Han 2009, Huang 2009] an effect of the textured growth of the Co-hcp phase with its c-axis perpendicular to the nanowire one that results in a competition between shape and magneto-crystalline anisotropies has been reported. Nevertheless, the contribution of reversible magnetization rotation is stronger along the perpendicular direction which suggests that the shape anisotropy remains dominant along the parallel direction.

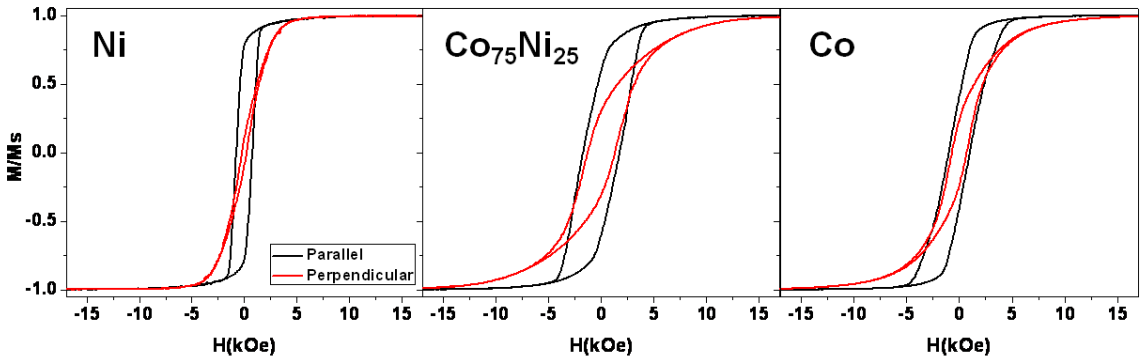

***Figure 7.4**: Room temperature hysteresis loops measured along the parallel (black) and perpendicular (red) directions with respect to the nanowires axis for Ni, $Co_{75}Ni_{25}$ and Co planar nanowire arrays.*

Sample	Hc (Oe)		M/Ms	
	Parallel	**Perpendicular**	**Parallel**	**Perpendicular**
Ni	774	220	0.78	0.1
Co75Ni25	1742	1292	0.6	0.31
Co	1000	700	0.4	0.24

***Table 7.2**: Coercive fields and reduced remanences extracted from the room temperature hysteresis loops measured along the parallel and perpendicular directions with respect the nanowires axis in planar PAAM nanowire arrays of different compositions.*

The axial direction in case of CPAAM nanowire arrays and the perpendicular in planar PAMM nanowire arrays are both equivalent with respect to the magnetic nanowires since in both cases the applied magnetic field is perpendicular to all the nanowires embedded in each array. The comparison between hysteresis loops of CPAAM and planar nanowire arrays measured with the magnetic field applied along the axial and perpendicular directions, respectively, is shown in *Figure 7.5*. In all cases, the HLs fit almost perfect between them suggesting that the array geometry does not affect the intrinsic magnetic behavior of nanowires. However, $Co_{75}Ni_{25}$ nanowires show slight differences regarding to the coercive field. As it was mentioned in chapter 5, Co-Ni alloys present a crystalline phase coexistence which can be metastable depending on the composition, and can suffer small changes during the electrodeposition acquiring a statistical character. The measurement of the HLs along the radial direction with respect to the Al wire contains all possible orientations of the nanowires with respect to the applied magnetic field, therefore differences between the HLs along the radial direction in CPAAM and parallel one in planar nanowire arrays are expected, as it can be observed in Figure 7.5 d), f) and g). The main differences lie on the remanence and the approaching to the saturation state which can be correlated to a reversible magnetization rotation of those nanowires that have a strong component of the applied magnetic field pointing along the perpendicular direction with respect to their long axis.

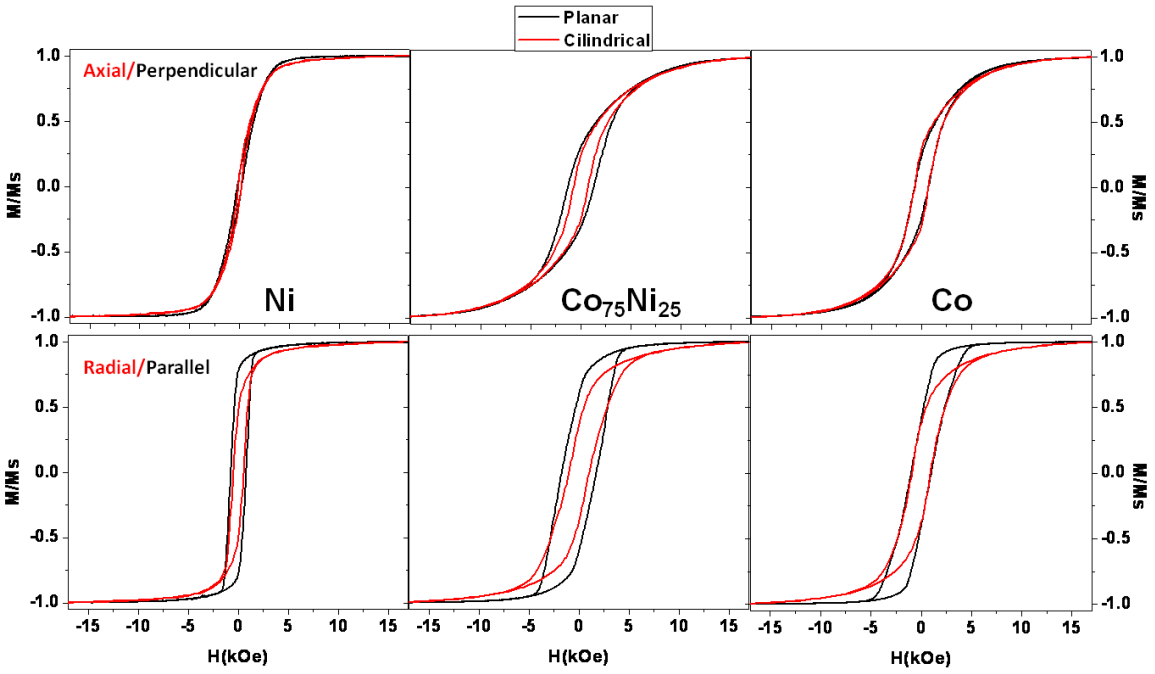

***Figure 7.5**: Comparison of room temperature hysteresis loops between planar (black) and cylindrical (red) nanowire arrays measured along the perpendicular/axial (top) and parallel/radial (bottom) of Ni, $Co_{75}Ni_{25}$ and Co nanowires arrays.*

In principle, the different orientation of the nanowires along the radial direction would result in a distribution of different coercive fields which would be related to the angular dependence of H_C with respect to the angle between the applied magnetic field direction and the nanowires axis. Furthermore, the magnetostatic interactions between nanowires also depend on the magnetization direction of the neighboring nanowires. In order to obtain such distributions, FORC analysis has been performed in all samples along the two perpendicular directions. Planar nanowire arrays offer the possibility to measure the contribution to the hysteresis of the two extremes directions, parallel and perpendicular to the nanowire axis. In Figure 7.6 the FORC diagram of these nanowire arrays are displayed. FORC distributions obtained along the perpendicular direction are elongated along the Hc axis, but much narrow along the Hu axis, indicating a weak interaction field and a broad SFD, particularly remarkable in the case of $Co_{75}Ni_{25}$. More information can be extracted from the parallel FORC diagrams where the effect of the dipolar interaction is appreciable. Particularly, in the case of Co nanowire planar arrays, the "wishbone" shape of FORC distributions is clearly evidenced in Figure 7.6 f). However, the elongated distribution along Hu shows a curvature toward larger values of Hc at negative values of the interaction field axis, which is an indicative of a log-normal or asymmetric SFD. The $Co_{75}Ni_{15}$ FORC diagram along the parallel direction shows a wide SFD that in principle may be related to the crystalline fcc and hcp phase coexistence.

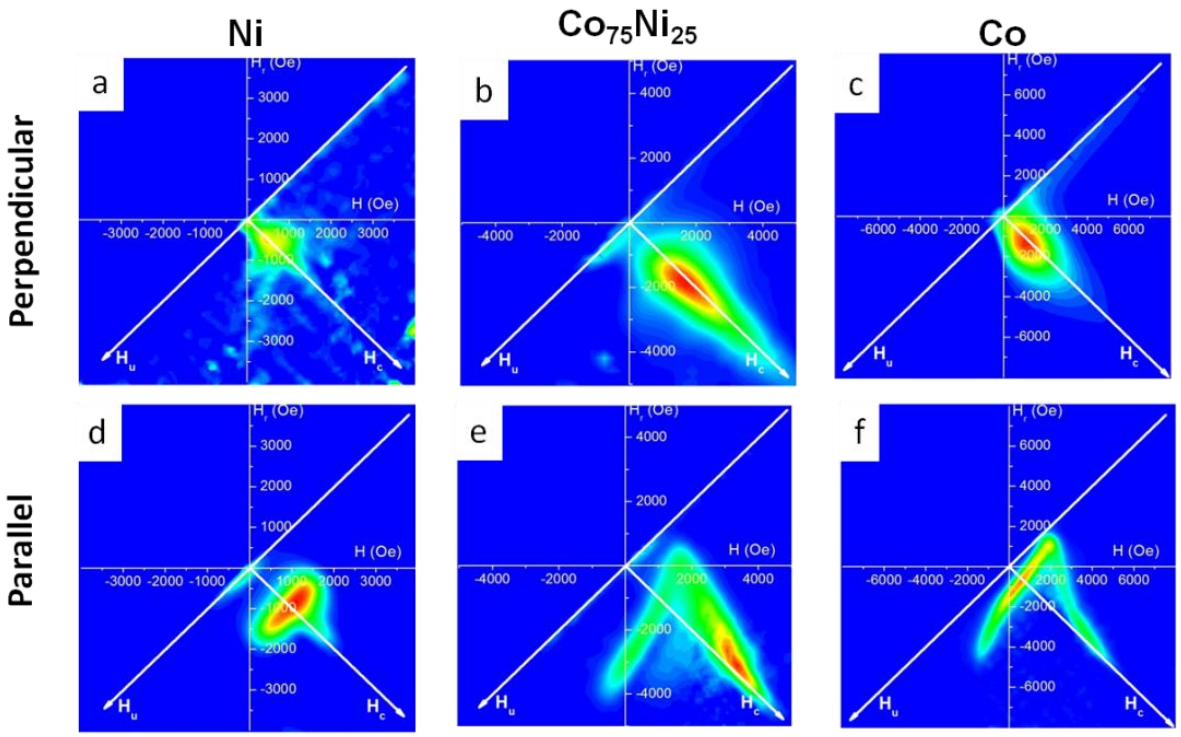

***Figure 7.6**: FORC diagrams of Ni, $Co_{75}Ni_{25}$ and Co planar nanowire arrays evaluated along the perpendicular (top) and parallel (bottom) direction with respect to the nanowires axis.*

FORC diagrams obtained along the axial direction in the CPAAM arrays show again an absence of magnetostatic interactions among nanowires as can be seen in Figure 7.7. However, the radial FORC diagrams show more complex FORC distributions, though keeping similarities with the parallel FORC distributions of planar nanowire arrays. The fact of measuring all possible orientations of nanowires with respect to the applied magnetic field could result in such a complex FORC diagrams since they would be affected by a continuous distribution coming from the angular dependence of the reversal magnetization process.

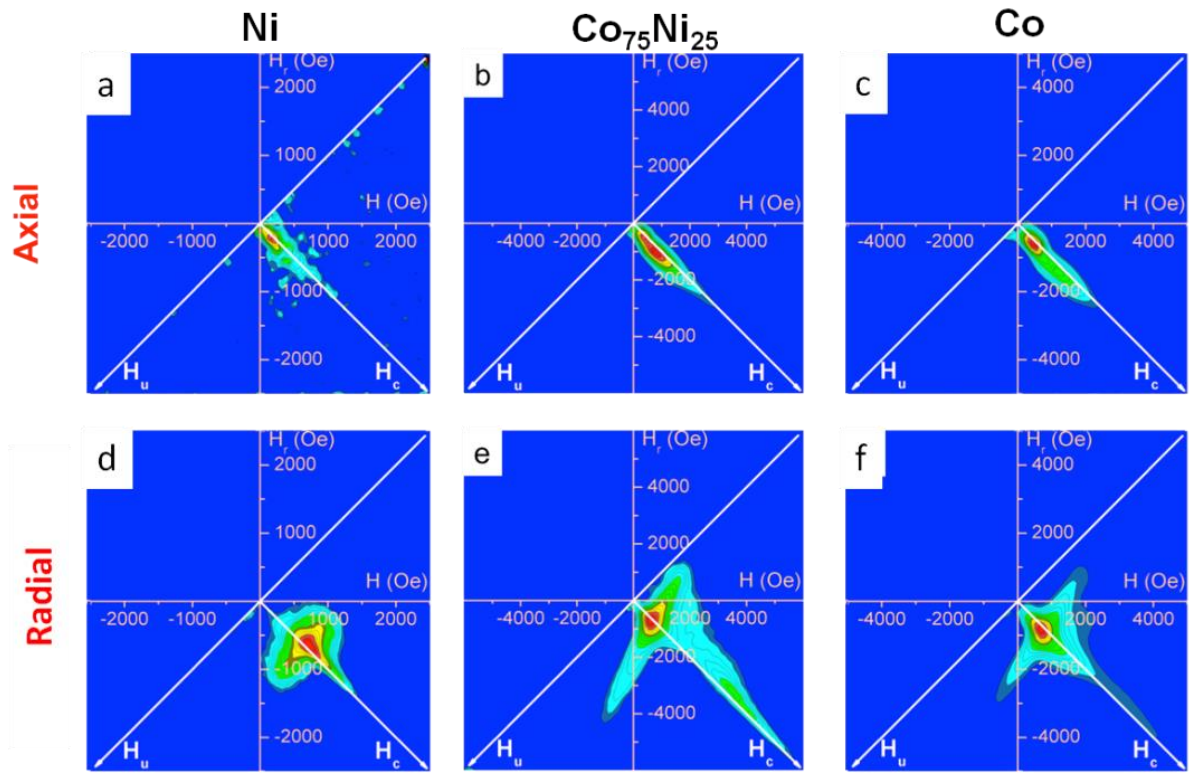

Figure 7.7: *FORC diagrams of Ni, $Co_{75}Ni_{25}$ and Co CPAAM nanowire arrays evaluated along the axial (top) and radial (bottom) direction with respect to the Al wire substrate.*

As a first approximation, the FORC distributions obtained from measurements along the parallel and perpendicular directions in planar nanowire arrays have been superposed in *Figure 7.8* for each nanowire array composition. These superposed FORC distributions display a very similar behavior to the respective radial ones of CPAAM nanowire arrays. This could be an indicative that if the radial FORC distributions are exactly the continuous and independent superposition of the angular dependence of the switching process, the correlation length of the magnetostatic interactions would be shorter than the curvature of the membrane which would means that the collective magnetic behavior of the CPAAM and planar nanowire arrays are in fact the same. In other words, a given nanowire embedded in the CPAAM template, sees the neighboring nanowires as they would be in a planar PAAM since the radius of the cylindrical membrane is several orders of magnitude larger than the length of nanowires and the distance between them.

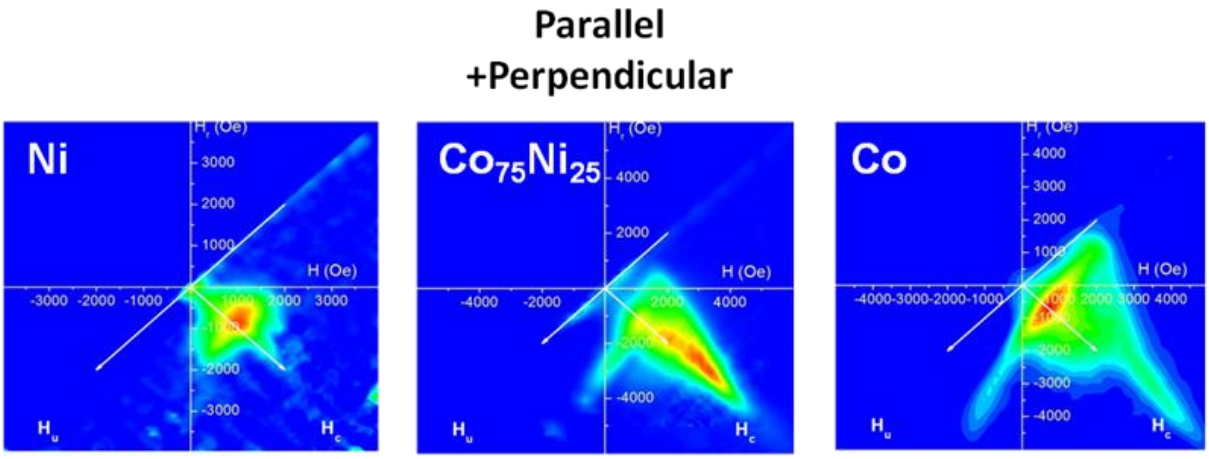

***Figure 7.8**: Superposition between parallel and perpendicular FORC distributions corresponding to Ni, $Co_{75}Ni_{25}$ and Co planar nanowire arrays.*

Making use of the computational program that was developed in chapter 4; it has been possible to simulate the FORC behavior taking into different possible orientations between the nanowires with respect to the applied magnetic field, as it is the case of CPAAM nanowires arrays measured along the radial direction with respect to the Al wire. In this case, the qualitative angular dependence of the coercive field for Co planar nanowire arrays studied in chapter 6 has been used. In addition, the angular dependence of the interaction field as well as the contribution of reversible magnetization rotation has been introduced [Proenca 2014]. In the first case, the magnetostatic interactions among nanowires are stronger when the applied magnetic field is applied parallel to the nanowire axis, thus in principle the interaction strength at saturation α would decrease as the angle between the applied field and the nanowire axis increases. Furthermore, as it was reflected by the HLs measured in planar nanowire arrays, the magnetization easy axis lies along the parallel direction with respect to the nanowires axis, and then the reversible magnetization rotation should increase as the angle increases. The FORC distribution along the magnetization easy axis is modified when the contribution of all possible orientations is introduced, as can be seen in Figure 7.9. These simulated FORC diagrams are presented in arbitrary units because the main interesting point is the shape of the resulting FORC distribution. For comparison, the equivalent experimental FORC diagrams of Co PAAM and CPAAM nanowire arrays are displayed in the same figure. As it can be observed, the simulated FORC diagrams along the magnetization easy axis, which would correspond to the parallel direction in the case of planar PAAM, shows the well known “wishbone” shape, in accordance with the experimental diagram. Moreover,

when the contribution of the angular dependence of the SFD is introduced, the effect is to distort the shape of the FORC distribution in a strongly similar way to the case of experimental FORC distribution obtained along the radial direction in Co CPAAM nanowire arrays.

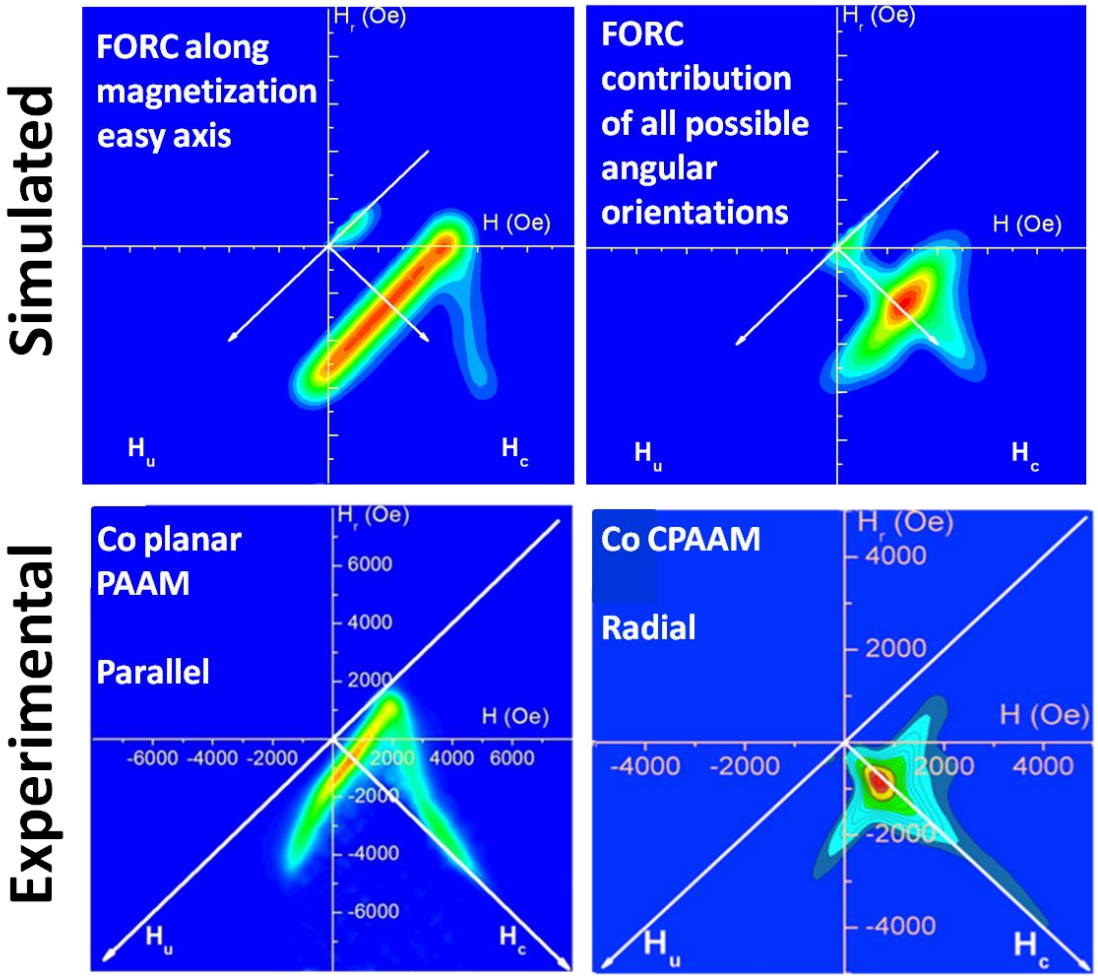

***Figure 7.9**: Simulated FORC diagrams (top) of Co planar PAAM (left) and Co radial CPAAM nanowire array; for comparison the corresponding experimental FORC diagrams are also shown (bottom).*

7.4. Summary and Conclusions

Cylindrical nanoporous alumina membranes have been performed by anodization of high purity Al wires. Those membranes were used as templates to growth magnetic nanowires by pulsed electrodeposition from a bath containing ions of the different transition metals employed in this study. Furthermore, planar nanoporous alumina membranes and thus, planar magnetic nanowire arrays have been fabricated under the

same conditions and employed as reference materials in order to evaluate the influence of the nanowire cylindrical arrangement on the magnetic properties.

Room temperature hysteresis loops have been measured and studied along two directions of the applied magnetic field. One is the Al wire axial direction, where the axis of each nanowire is perpendicular to the magnetic field, and the other one is a radial direction with respect to the Al wire covering all orientations between nanowires and the magnetic field. As a first approximation, comparing the hysteresis loops of planar and cylindrical nanowire arrays, the radial SFD for the cylindrical array has been found to be the superposition of magnetization reversal processes as a function of the angle between each nanowire and the applied field direction. Experimental and simulated FORC results confirm that the correlation length of the magnetostatic interaction among nanowires is short enough to be not modified by the array curvature.

8. GENERAL CONCLUSIONS AND FURTHER WORKS

One of the main aims in this work has been a better understanding of the different process that take part on magnetization reversal of magnetic nanowire arrays embedded in nanoporous alumina membranes. A deep study on FORC analysis has been carried out in order to demonstrate the potential applicability of such method to the mentioned above systems. The development of a computational program to simulate FORC of magnetic nanowire arrays under different physical conditions treated from a phenomenological point of view has been resulted in one of the principal key factors for the successfully understanding of the different magnetic behaviors found in the systems studied in the present work. As far as all studies have been performed supposing a Gaussian SFD, the study of how the FORC diagram can be modified by other statistical distributions and, and particularly asymmetric distributions, being this work in progress. Furthermore, the effects of not uniform magnetostatic interactions among nanowires should be explored, with the aim of knowing if the pattern given by the membranes actually affects the reversal magnetization processes and modifies or not parameters as the coercive field of the magnetic nanowire array, among others.

Nowadays, heterogeneous structures as multilayered and/or multi-segmented materials are attracting much attention. However, the resulting magnetic behavior of such ~~a~~ complex nanostructures is hardly understood due to the necessity of measuring the macroscopic magnetization reversal process in the conventional magnetometry as the VSM technique. The FORC analysis has been found to be a good candidate to solve the cooperation, through interactions, between different nanostructures. Contacting long Co and Ni nanowires at one end in the array, the resulting hysteresis loop is completely different to the case of a magnetization reversal produced by both separated Co and Ni nanowire arrays. Based on the FORC analysis, two possible magnetization reversal processes have been proposed as a consequence of the exchange coupling between the Ni/Co nanowires. Basically, depending on the relative difference between both magnetization switching, the softer phase could induce the switching of the harder one through the injection and propagation of a magnetic domain wall. On the other hand, being the switching fields values different enough, the antiparallel magnetic configuration of nanowires could be possible but energetically unfavorable, thus the switching of the softer phase would be modified in order to avoid such configuration.

These previous results have been taken into account in the study of multi-segmented nanowire arrays, where each segment corresponds to a different Co-Ni composition. The tuning of the composition, crystalline structure and thus magnetic properties of each segment by the electrodeposition potential has been demonstrated. In case of parallel hysteresis loops to the nanowire axis no evidence of two different magnetic phases existence has been detected, which in principle would suggest that the magnetization reversal process would be driven by one kind of segments and/or an average of both magnetic phases, resulting in a homogeneous behavior. However, paying more attention to the perpendicular direction with respect the nanowire axis, some different irreversible magnetization reversals can be detected. The resulting FORC diagrams have been associated to two different ferromagnetic phases interacting between them. However, further studies on multi-segmented nanowires with more pronounced differences on the magnetic properties of each segment should be carried out in order to extract more defined information about the overall magnetic properties of such complex nanostructures.

Deepening on the magnetic behavior of heterogeneous nanowires embedded in nanoporous anodic alumina membranes, Co-Cu nanowire arrays have been fabricated. From structural characterization, the addition of Cu produces an increase of the fcc phase crystallization with respect the main Co-hcp one that has been found in pure Co nanowire arrays. Moreover, the interplanar distances in the hcp crystalline structure is modified with the Cu addition provoking a deformation of the structure. As an effect of the Cu in the magnetic properties, the effective magnetic anisotropy is enhanced along the parallel direction with respect to the nanowire axis that is consistent with the reduction of the magneto-crystalline anisotropy. However, for low Cu amounts, two different ferromagnetic phases have been detected in parallel hysteresis loops. Those have been ascribed to a pure Co-like soft ferromagnetic phase and a harder Co-Cu phase. Interestingly, from FORC analysis both distributions do not behave as independent ones suggesting that both ferromagnetic phases could be magnetically coupled.

Pure Co nanowires present a reduction of magneto-crystalline anisotropy of the hcp phase with increasing temperature, however the strongest temperature effect has been found in the sample that presents the two different phases and a reduction of such hcp phase. Moreover, the previous fact points out that in this sample not only the dependence of the magneto-crystalline anisotropy with respect to the temperature, but the magnetic

interactions between nanowires, which depends on the difference between the switching fields of each phase, are also responsible of such variations on the coercive field and reduced remanence of the nanowire array. However, since the different phases could not be detected with HR-TEM characterization mainly due to the possible degradation of nanowires surfaces during the chemical etching of the membrane, a more detailed HR-TEM characterization focused with the aim of elucidate both different phases and the role of Cu atoms in specially prepared Co-Cu samples to this technique is required.

Finally, further studies focused on the effect of arrangements geometry on the magnetic properties of nanowire arrays are of special interest from both fundamental and applied point of view. The FORC method has been employed to solve technical difficulties of the magnetic measurements due to the macroscopic geometry of cylindrical nanowire arrays, extracting intrinsic properties of each nanowire and the magnetostatic interactions among them. In the specific case of CPAAM nanowire arrays, may be interesting the reduction of the Al wire diameter and the study of the curvature influence of the membrane on the magnetic interactions among nanowires.

9. CONCLUSIONES Y FUTUROS TRABAJOS

Uno de los principales objetivos de este trabajo ha sido la mejor comprensión de los diferentes procesos que intervienen en la inversión de la imanación de arreglos ordenados de nanohilos magnéticos crecidos en membranas de alúmina nanoporosa. Se ha llevado a cabo un estudio profundo del análisis FORC con el fin de demostrar la potencial aplicabilidad de tal método a los sistemas mencionados anteriormente. El desarrollo de un programa computacional para simular FORC de arreglos de nanohilos magnéticos en diferentes condiciones físicas tratadas desde un punto de vista fenomenológico, ha dado lugar a uno de los principales factores clave para el éxito de la comprensión de los diferentes comportamientos magnéticos que se encuentran en los sistemas estudiados en el trabajo actual. Aunque se hayan realizado todos los estudios suponiendo un SFD de tipo Gausiano, el estudio de cómo el diagrama FORC puede ser modificado por otras distribuciones estadísticas, y particularmente distribuciones asimétricas, sigue siendo un trabajo en progreso. Por otra parte, los efectos de las interacciones magnetostáticas no uniformes entre los nanohilos deben ser exploradas, con el objetivo de conocer si el patrón dado por las membranas afecta realmente los procesos de inversión de la imanación y si modifica o no parámetros tales como el campo coercitivo o remanencia del conjunto de nanohilos magnéticos.

Hoy en día, las estructuras heterogéneas de materiales como por ejemplo multicapas y / o multisegmentos están atrayendo mucha atención. Sin embargo, el comportamiento magnético resultante de tales nanoestructuras complejas apenas puede ser entendido debido a la necesidad de medir el proceso de inversión de la imanación macroscópica en la magnetometría convencional como es la técnica de VSM. El análisis FORC es un buen candidato para resolver la cooperación, a través de interacciones, entre las diferentes nanoestructuras. Al ponerse en contacto los extremos de nanohilos largos de Co y Ni la matriz de alúmina (muestra Ni/Co), el ciclo de histéresis resultante es completamente distinto al caso de una inversión de la imanación producida por arreglos separados de nanohilos de Co y Ni. Basándose en el análisis FORC, dos posibles procesos de inversión de la imanación han sido propuestos como consecuencia del acoplamiento de "exchange" entre los nanohilos de Ni/Co. Básicamente, en función de la diferencia relativa entre la coercitividad ambos, la fase magnéticamente más suave podría inducir a

la inversión de la más difícil a través de la inyección y la propagación de una pared de dominio magnético. Por otra parte, siendo los campos coercitivos lo suficientemente diferentes, la configuración magnética antiparalela de los nanohilos podría ser accesible pero energéticamente desfavorable, por lo tanto la inversión de la fase más suave sería modificada con el fin de evitar tal configuración.

Estos resultados se han tenido en cuenta en el estudio de arreglos de nanohilos de aleaciones Co-Ni multisegmentados, donde cada segmento corresponde a una composición de Co-Ni diferente. El cambio en la composición, debido al potencial de electrodeposición, lleva consigo un cambio en la estructura cristalina y por lo tanto en las propiedades magnéticas de cada segmento. En el caso de los ciclos de histéresis paralelos al eje de los nanohilos se han observado evidencias de dos fases magnéticas distintas, que en principio podría sugerir que el proceso de inversión de la imanación sería dominada por un tipo de segmento y / o un promedio de las dos fases magnéticas, lo que resulta en un comportamiento homogéneo. Sin embargo, al prestar más atención en la dirección perpendicular con respecto al eje de los nanohilos, se han detectado dos procesos distintos de inversión de la imanación irreversibles. Los diagramas FORC resultantes se han asociado a dos fases ferromagnéticas diferentes que interactúan entre sí. Sin embargo, estudios adicionales sobre nanohilos multisegmentados con diferencias más pronunciadas en las propiedades magnéticas de cada segmento deben llevarse a cabo con el fin de extraer información más definida sobre las propiedades magnéticas generales de dichas nanoestructuras complejas.

Para la profundización en el estudio del comportamiento magnético de nanohilos heterogéneos crecidos en membranas de alúmina anódica nanoporosa, se han fabricado arreglos ordenados de nanohilos de Co-Cu. De la caracterización estructural, se ha encontrado que la adición de Cu produce un aumento de la cristalización en la fase cristalina fcc con respecto a la fase mayoritaria de Co-hcp que se ha encontrado en los arreglos de nanohilos de Co puro. Por otra parte, las distancias interplanares en la estructura cristalina hcp también son modificadas con la adición de Cu, provocando así una deformación en dicha estructura. El efecto del Cu en las propiedades magnéticas, ha sido el incremento en la uniaxialidad de la anisotropía magnética efectiva a lo largo de la dirección paralela con respecto al eje de los nanohilos, siendo consistente con la reducción de la anisotropía magneto-cristalina de la fase hcp. Sin embargo, para cantidades bajas de Cu (8 at.%) , dos comportamientos ferromagnéticos distintos han sido

detectados en los ciclos de histéresis paralelos. Dichos comportaamientos se han atribuido a una fase magnéticamente blanda de Co puro y una fase de Co-Cu más difícil. Curiosamente, a partir del análisis FORC ambas distribuciones no se comportan como independientes, lo que sugiere que ambas fases ferromagnéticas podrían estar acopladas magnéticamente .

Los nanohilos de Co puro presentan una reducción de la anisotropía magneto-cristalina de la fase hcp al aumentar la temperatura, sin embargo, la dependencia más pronunciada con la temperatura se ha encontrado en la muestra que presenta las dos fases diferentes y una reducción de la cantidad de fase hcp. Por otra parte, el hecho anterior señala que en esta muestra no sólo muestra una dependencia de la anisotropía magneto-cristalina con respecto a la temperatura, sino que las interacciones magnéticas entre las distintas fases, que dependerían de la diferencia entre los campos de inversión de la imanación de cada fase, también son responsables de tales variaciones del campo coercitivo y la remanencia reducida del arreglo de nanohilos. Sin embargo, ya que las diferentes fases no han podido ser detectadas mediante la caracterización HR-TEM, principalmente debido a la posible degradaciónde la superficie de los nanohilos durante el ataque químico de la membrana, se requiere de una caracterización HR- TEM más detallada enfocando el estudio en la observación de las distintas fases y el papel que juegan los átomos de Cu en estas muestras.

Por último, el efecto de la geometría de las matrices en las propiedades magnéticas de los arreglos de nanohilos es de especial interés desde el punto de vista tanto fundamental como aplicado. El método FORC se ha empleado para resolver dificultades técnicas en las medidas magnéticas debido a la geometría macroscópica de las matrices de nanohilos cilíndricos, pudiendo extraer propiedades intrínsecas de cada nanohilo y las interacciones magnetoestáticas entre ellos. En el caso específico de las matrices de nanohilos CPAAM , puede ser interesante la reducción del diámetro del hilo de Al y el estudio de la influencia de la curvatura de la membrana en las interacciones magnéticas entre los nanohilos.

REFERENCES

[Alwitt 2002] R. S. Alwitt, "Anodizing" in "Electrochemistry Encyclopedia" http://electrochem.cwru.edu/encycl/) (2002)

[Bachmann 2008] J. Bachmann, R. Zierold, Y. T. Chong, R. Hauert, C. Sturm, R. Schmidt-Grund, B. Rheinländer, M. Grundmann, U. Gösele and K. Nielsch, *Angew. Chem. Int. Ed*. **47**, (2008) 6177.

[Bakkaloglu 2001] Ö. F. Bakkaloglu and I. H. Karahan, *Turk. J. Phy.* **25**, (2001) 27-33.

[Barandiaran 1989] J. M. Barandiaran, M. Vázquez, A. Hernando, J. González and C. Rivero, *IEEE Trans. Magn.* **25**, (1989) 3330.

[Berkowitz 1992] A.E. Berkowitz, J. R. Mitchell, M. J. Carey, A. P. Young, S. Zhang, F. E. Spada, F. T. Parker, A. Hutten and G. Thomas. *Phys. Rev. Lett.* **68**, (1992) 3745.

[Béron 2007] F. Béron, L. Clime, M. Ciureanu, D. Ménard, R. W. Cochrane and A. Yelon, *J. Appl. Phys*. **101**, (2007) 09J107.

[Béron 2008] F. Béron, D. Ménard and A. Yelon, *J. Appl. Phys*. **103**, (2008) 07D908.

[Béron 2010] F. Béron, L.P. Carignan, D. Ménard and A. Yelon, ISBN: 978-953-7619-88-6, "Chapter 7: Extracting Individual Properties from Global Behaviour: First-order Reversal Curve Method Applied to Magnetic Nanowire Arrays", (2010).

[Bertotti 1998] G. Bertotti, ISBN: 0-12-093270-9, "Hysteresis in Magnetism", (1998), *Academic Press, London*.

[Bottoni 1997] G. Bottoni, D. Candolfo and A. Cecchetti, *J. Appl. Phys.* **81**, (1997) 3794.

[Callen 1966] H.B. Callen, E. Callen, *J. Phys. Chem. Solids* **27**, (1966) 1271–1285.

[Camley 1993] R. E. Camley and R. L. Stamps, *J. Phys.: Condens. Matter* **5**, (1993) 3727-3786.

[Che 1992] X. D. Che and N. Bertram, J. *Magn. Magn. Mater*. 116, (1992) 121.

[Cheng 2008] S.L. Cheng, C. N. Huang, *Synthesis and Reactivity in Inorganic, Metal-Organic, and Nano-Metal Chemistry* **38**, (2008), 475-480.

[Chikazumi 1997] S. Chikazumi, ISBN: 0-19-851776-9, "Physics of Ferromagnetism", (1997) Oxford University Press.

[Chu 2005] S. C. Chu, K. Wada, S. Inoue, M. Isogai, A. Yasumori, *Adv. Mater*. **17**, (2005) 2115.

[Cullity 1972] B.D. Cullity, ISBN: 0201012189, "Introduction to Magnetic Materials" (1972), Ed. Wiley.

[Darques 2005] M. Darques, L. Piraux, A. Encinas, P. Bayle-Guillemaud, A. Popa, and U. Ebels, *Appl. Phys. Lett*. **86**, (2005), 072508.

[Della Torre 1999] E. Della Torre, ISBN: 0-7803-6041-9, "Magnetic Hysteresis", (1999), IEEE Press.

[De La Torre Medina 2009] J. De La Torre Medina, M. Darques, L. Piraux and A. Encinas, *J. Appl. Phys.* **105**, (2009) 023909.

[Dickey 2002] E.C. Dickey, O.K. Varghese, K.G. Ong, D. Gong, M. Paulose and C.A. Grimes, *Sensors* **2**, (2002) 91.

[Diggle 1969] J. W. Diggle, T. C. Downie, C.W. Goulding, *Chem. Rev*. **69,** (1969) 365.

[Dimitru 2005] I. Dimitru, F. Li, J.B. Wiley, D. Cimpoesu, A. Stancu and L. Spinu, *IEEE Trans. Mag.* **41** (2005) 3361.

[Eftekhari 2008] A. Eftekhari (Editor), ISBN: 978-3-527-31876-6, Nanostructured Materials in Electrochemistry (2008), Ed. Wiley-VCH.

[Encinas-Oropesa 2001] A. Encinas-Oropesa, M. Demand, L. Piraux, I. Huynen and U. Ebels, *Phys. Rev. B* **63**, (2001) 104415.

[García-Arribas 1992] A. García-Arribas, J.M. Barandiaran and G. Herzer, *J. Appl. Phys.* **71**, (1992) 3047.

[García-Vergara 2006] S. J. García-Vergara, P. Skeldon, G. E. Thompson, H. Habazaki, *Electrochim. Acta* **52**, (2006) 681.

[García-Vergara 2007] S. J. García-Vergara, H. Habazaki, P. Skeldon, G. E. Thompson, *Nanotechnology* **18**, (2007) 415605.

[Geshev 1997] J. Geshev and J. E. Schmidt, *IEEE Trans. Magn*. **33**, (1997) 2504.

[Ghahremaninezhad 2009] A. Ghahremaninezhad and A. Dolati, *J. Alloys Compd*. **480**, (2009) 275-278.

[Gómez 1998] E. Gómez, J. Ramirez, E. Vallés, *J. Appl. Electrochem*. **28**, (1998) 71.

[Gómez 2005] E. Gómez, S. Pané, E. Vallés, *Electrochem. Acta* **51**, (2005) 146.

[Gong 2003] D. Gong, V. Yadavalli, M. Paulose, M. Pishko and C.A. Grimes, *Biomed. Microdevices* **5**, (2003) 75.

[Grimes 2000] C.A. Grimes and D. Kouzoudis, Sens. Actuators A. 84, (2000) 205.

[Ha 2010] Y. C. Ha, D. Y. Jeong, *J. Korean Phys. Soc*. **57**, (2010) 1661.

[Han 2009] X. Han, Q. Liu, J. Wang, S. Li, Y. Ren, R. Liu and F. Li, *J. Phys. D: Appl. Phys.* **42**, (2009) 095005.

[Hansen 1958] M. Hansen, "Constitution of Binary Alloys", (1958) 2nd edition New York: McGraw-Hill.

[Hennesthal 2003] C. Hennesthal, Application Report NanoWizard, JPK Instruments AG, (2003).

[Henkel 1964] O. Henkel, *Phys. Status Solidi* **7**, (1964) 919.

[Hochbaum 2010] A.I. Hochbaum and P. Yang, *Chem. Rev*. **110**, (2010), 527.

[Huang 2009] X. H. Huang, G. H. Li, X. C. Dou and L. Li, J. Appl. Phys. **105**, (2009) 084306.

[Huerta 2012] J. M. Martinez Huerta, J. De La Torre Medina, L. Piraux and A. Encinas, *J. Appl. Phys*. **111**, (2012) 083914.

[Jeesenky 1998] O. Jeesensky, F. Müller, U. Gösele, *Appl. Phys. Lett*. **72**, (1998) 1173.

[Jiles 1998] D. Jiles, ISBN: 978-0-412-79860-3, "Introduction to Magnetism and Magnetic Materials", (1998) Ed. Taylor & Francis.

[Kang 2007] H.J. Kang, D.J. Kim, S.J. Park, J.B. Yoo and Y.S. Ryu, *Thin Solid Films* **515**, (2007) 5184.

[Karaagac 2010] O. Karaagac, M. Alper and H. Kockar, *J. Magn. Magn. Mat*. **322**, (2010), 1098-1101.

[Kashi 2011] M. A. Kashia, A. Ramazania, F. A. Najafabadia and Z. Heydarib, *Appl. Surf. Sci*. **257**, (2011) 9347-9350.

[Kelly 1989] P. E. Kelly , K. O'Grady, P.I. Mayo and R. W. Chantrell, *IEEE Trans. Magn.* **25**, (1989) 3881.

[Knaack 2004] S.A. Knaack, M. Redden and M. Onellion, *Am. J. Phys*. **72**, (2004) 856.

[Lee 2006] W. Lee, R. Ji, U. Gösele, K. Nielsch, *Nature Materials* **5**, (2006) 741.

[Levy 1994] P. M. Levy, *Solid State Physics* **47** (1994), p. 367, Academic Press, New York.

[Lupu 2010] N. Lupu (Editor) ISBN: 978-953-7619-88-6, "Electrodeposited Nanowires and their applications" (2010), Ed. InTech.

[Martín 2003] J.I. Martín, J. Nogués, K. Liu, J.L. Vicent and I.K. Schuller, *J. Magn. Magn. Mater*. **256**, (2003) 449.

[Martínez-Huerta 2012] J. M. Martínez Huerta, J. de la Torre Medina, L. Piraux and A. Encinas, *J. Appl. Phys*. **111**, (2012) 083914.

[Masuda 1995] H. Masuda, K. Fukuda, *Science* **268**, (1995) 1466.

[Mayergoyz 1991] I. D. Mayergoyz, *Phys. Rev. Lett.* **56**, (1986) pp. 1518-1521.

[Mayergoyz 1991] I. D. Mayergoyz, "Mathematical Models of Hysteresis", (1991), Springuer-Verlag: New York.

[Meng 2005] G. W. Meng, A. Y. Cao, J. Y. Cheng, A. Vijayaraghavan, Y. J. Jung, M. Shima and P. M. Ajayan, *J. Appl. Phys*. **97**, (2005) 064303.

[Mikkelsen 2013] A. Mikkelsen, E. Lundgren, *Surface Science* **607**, (2013) 97–105.

[Nalwa 2011] H.S. Nalwa (Editor) ISBN: 1-58883-001-2, "Encyclopedia of Nanoscience and Nanotechnology" (2011), Ed. American Scientific Publishers.

[Navas 2007] D. Navas, "Fabricación y Caracterización de Arreglos de Nanohilos Magnéticos en Películas Nanoporosas de Alúmina Anódica" Tesis Doctoral, (2007) Universidad Autónoma de Madrid-Instituto de Ciencia de Materiales de Madrid.

[Navas 2012] D. Navas, J. Torrejon, F. Béron, C. Redondo, F. Batallan, B. P. Toperverg, A. Devishvili, B. Sierra, F. Castaño, K. R. Pirota and C. A. Ross, *New J. Phys.* **14**, (2012) 113001.

[Nielsch 2000] K. Nielsch, F. Müller, A. P. Li, U. Gösele, *Adv. Mater*. **12**, (2000) 582.

[Nielsch 2002] K. Nielsch, J. Choi, K. Schwirn, R. B. Wehrspohn, U. Gösele, *Nano Lett.* **2,** (2002) 677.

[Oh 2011] J. Oh, C. V. Thompson, *Electrochim. Acta* **56**, (2011) 4044.

[O'Handley 1999] R.C. O'Handley, ISBN: 0-471-15566-7, "Modern Magnetic Materials: Principles and Applications", (1999) John Wiley & Sons, Inc.

[Oldham 1994] H. B. Oldham and J. C. Myland, "Fundamentals of Electrochemical Science", (1994), Academic press, INC., San Diego (USA).

[Pan 2005] H. Pan, H. Sun, C. Poh, Y. P. Feng and J. Y. Lin, *Nanotechnology* **16**, (2005), 1559.

[Patermarakis 2009] G. Patermarakis, *J. Electroanal. Chem*. **635**, (2009) 39.

[Patermarakis 2011] G. Patermarakis, K. Moussoutzanis, *J. Electroanal. Chem*. **659**, (2011) 176.

[Paunovic 1998] M. Paunovic and M. Schlesinger, ISBN: 0471712213, "Fundamentals of Electrochemical Deposition", (2006), Wiley-Interscience.

[Phan 2008] M. H. Phan and H. X. Peng, *Prog. Mater. Sci*. **53**, (2008) 323–420.

[Pike 1999] C. Pike and A. Fernandez, *J. Appl. Phys*. **85**, (1999) 6668.

[Pike 2003] C. R. Pike, *Phys. Rev. B* **68**, (2003) 104424.

[Pike 2005] C. R. Pike, C. A. Ross, R. T. Scalettar and G. Zimanyi, *Phys. Rev. B* **71**, (2005) 134407.

[Pirota 2011] K. R. Pirota, F. Béron, D. Zanchet, T. C. R. Rocha, D. Navas, J. Torrejón, M. Vázquez and M. Knobel, *J. Appl. Phys*. **109**, (2011), 083919.

[Preisach 1935] F. Preisach, *Z. Phys*. **94**, (1935) pp. 277-302.

[Prida 2007] V.M. Prida, K. R. Pirota, D. Navas, A. Asenjo, M. Hernández-Vélez, M. Vázquez, *J. Nanosci. Nanotechnol*. **7**, (2007) 272.

[Prida 2013] V.M. Prida, J. García, L. Iglesias, V. Vega, D. Görlitz, K. Nielsch, E. Diaz Barriga-Castro, R. Mendoza-Reséndez, A. Ponce and C. Luna, *Nanoscale Res. Lett.* **8**, (2013) 263.

[Proenca 2012] M.P. Proenca, C.T. Sousa, J. Ventura, M. Vázquez and J. P. Araujo, *Electrochim. Acta* **72**, (2012) 215–221.

[Proenca 2014] M P Proenca, K J Merazzo, L G Vivas, D C Leitao, C T Sousa, J Ventura, J P Araujo and M Vázquez, *Nanotechnology* **24** (2013) 475703.

[Ren 2010] Y. Ren, Y.Y. Dai, B. Zhang, Q. F. Liu, D. S. Xue, J. B. Wang, *Nanoscale Res. Lett.* **5**, (2010), 853–858.

[Richter 2007] H. J. Richter, *J. Phys. D: Appl. Phys*. **40**, (2007) R149.

[Romero 2012] V. Romero, V. Vega, J. García, V. M. Prida, B Hernando and J.Benavente, *J. Colloid Interface Sci.* **376**, (2012) 40-6.

[Santos 2011] A. Santos, J.M. Montero-Moreno, J. Bachmann, K. Nielsch, P. Formentín, J. Ferré-Borrull, J. Pallarés, L.F. Marsal, *ACS Appl. Mater. Interfaces* **3**, (2011) 1925.

[Sanz 2007] R. Sanz, M. Hernández-Vélez, K. R. Pirota, J. L. Baldonedo and M. Vázquez, *Small* **3**, (2007) 434-437.

[Schmuki 2009] P. Schmuki, S. Virtanen, "Electrochemistry at the nanoscale", Springer, New York (USA) (2009) ISBN: p78-0-387-73581-8

[Silva 2006] E.L. Silva, W.C. Nunes, M. Knobel, J.C. Denardin, D. Zanchet, K. Pirota, D. Navas and M. Vázquez, *Physica B* **384**, (2006), 22–24.

[Srivastav 2014] A. K. Srivastav and R. Shekhar, *J. Magn. Magn. Mat*. **349**, (2014) 21-26.

[Srivastava 2006] M. Srivastava, V.E. Selvi, V.K.W. Grips and K.S. Rajam, *Surf. Coat. Tech*. **201**, (2006) 3051–3060.

[Sellmyer 2001] D. J. Sellmyer, M. Zheng and R. Skomski, *J. Phys.: Condens. Matter* **13**, (2001), 433.

[Tian 2011] L. Tian, J. Ramirez and E. Vallés, *J. Appl. Electrochem*. **28**, (2011) 71.

[Valenzuela 2002] R. Valenzuela, I. Betancourt, *IEEE Trans. Mag* **38**, No. 5, (2002).

[Varghese 2003] O.K. Varghese, D. Gong, W.R. Dreschel, K.G. Ong and C.A. Grimes, *Sens Actuators B* **94**, (2003) 27.

[Vázquez 2004] M. Vázquez, M. Hernández-Velez, K. Pirota, A. Asenjo, D. Navas, J. Velázquez, P. Vargas and C. Ramos, *European Physical Journal B* **40**, (2004) 489.

[Vázquez 2005] M. Vázquez, K. Pirota, J. Torrejón, D. Navas and M. Hernández-Vélez, *J. Magn. Magn. Mater*. **294**, (2005) 174.

[Vega 2006] V. Vega, "Implementación de un equipo de anodizado para la fabricación de películas de alúmina nanoporosa", Tesina de licenciatura (2006), Universidad de Oviedo.

[Vega 2008] V. Vega, "Nanomateriales funcionales basados en óxidos porosos de aluminio o titanio obtenidos por anodización electroquímica", Trabajo de investigación, (2008) Universidad de Oviedo.

[Vega 2010] V. Vega, V.M. Prida, J.A. García and M. Vázquez, *Phys. Status Solidi A.* **208**, (2010) 553.

[Vega 2012] V. Vega, T. Böhnert, S. Martens, M. Walwczek, J.M. Montero-Moreno, D. Görlitz, V.M. Prida and K. Nielsch, *Nanotechnology* 23, (2012), 465709.

[Vega 2012b] V. Vega, "Fabricación y Caracterización de Materiales Nanoestructurados Obtenidos Mediante Técnicas Electroquímicas" Tesis Doctoral, (2012) Universidad de Oviedo.

[Vivas 2012] L. G. Vivas, J. Escrig, D. G. Trabada, G. A. Badini-Confalonieri, and M. Vázquez, *App. Phys. Lett.* **100**, (2012), 252405.

[Vivas 2012 b] L.G. Vivas, "On the magnetic and structural properties of Co and Co-based nanowire arrays" Tesis Doctoral, (2012) Universidad Autónoma de Madrid, Instituto de Ciencia de Materiales de Madrid (CSIC).

[Vivas 2012 c] L. G. Vivas, M. Vazquez, J. Escrig, S. Allende, D. Altbir, D. C. Leitao and J. P. Araujo, *Phys. Rev. B.* **85**, (2012) 035439.

[Wehrspohn 2000] R.B. Wehrspohn, A.P. Li, K. Nielsch, F. Müller, W. Erfurth and U. Gösele, "Oxide Films", *Electrochemical Society Proceedings* **271**, (2000).

[Wohlfarth 1958] E. P. Wohlfarth, *J. Appl. Phys*. **29**, (1958) 595.

[Xiao 1992] J. Q. Xiao, J. S. Jiang and C. L. Chien, *Phys. Rev. Lett*. **68**, (1992), 3749.

[Yang 2010] P. Yang, R. Yan and M. Fardy, *Nano Lett*. **10**, (2010), 1529.

[Yang 2011] Z.H. Yang, Z. W. Li, L. Liu and L. B. Kong, *J. Magn. Magn. Mat*. **323**, (2011) 2674-2677.

[Yoon 2010] J. Yoon, S. Jo, I. S. Chun, I. Jung, H. S. Kim, M. Meitl, E. Menard, X. Li, J. J. Coleman, U. Paik & J. A. Rogers, *Nature Lett*. **465**, (2010) 329.

[Zaman 1998] H. Zaman, A. Yamada, H. Fukuda and Y. Ueda, *J. Electrochem. Soc*.**145**, (1998) 565-568.

[Zuo 2004] J. M. Zuo and J. C. Mabon, "Web-based Electron Microscopy Application Software: Web-EMAPS", Microsc. Microanal. **10,** Suppl 2, (2004) URL: http://emaps.mrl.uiuc.edu/.

LIST OF PUBLICATIONS

Related to this work:

1. **J. García**, V. Vega, L. Iglesias, Victor M. Prida, B. Hernando, E. D. Barriga-Castro, R. Mendoza-Reséndez, C. Luna, D. Görlitz, K. Nielsch. "Template-assisted Co–Ni alloys and multisegmented nanowires with tuned magnetic anisotropy" *Phys. Status Solidi A* (2014), DOI: 10.1002/pssa.201300731. (Published online)

2. V. Romero, M. I. Vázquez, S. Cañete, V. Vega, **J. García**, V. M. Prida, B. Hernando, J. Benavente. "Frictional and Electrical Effects Involved in the Diffusive Transport through a Nanoporous Alumina Membrane" *J. Phys. Chem. C.* Vol. **117**(48), 25513 (2013).

3. C. Bran, Yu. P. Ivanov, **J. García**, R. P. del Real, V. M. Prida, O. Chubykalo-Fesenko, M. Vazquez. "Tuning the magnetization reversal process of FeCoCu nanowire arrays by thermal annealing" *J. Appl. Phys*. Vol. **114**(4), 043908 (2013)

4. V.M. Prida, **J. García**, L. Iglesias, V. Vega, D. Görlitz, K. Nielsch, E.D. Barriga-Castro, R. Mendoza-Reséndez, A. Ponce, C. Luna. "Electroplating and magnetostructural characterization of multisegmented $Co_{54}Ni_{46}/Co_{85}Ni_{15}$ nanowires from single electrochemical bath in anodic alumina templates" *Nanoscale Res Lett.* Vol. **8**, 263 (2013).

5. V. Romero, V. Vega, **J. García**, R. Zierold, K. Nielsch, V.M. Prida, B. Hernando, J. Benavente. "Changes in morphology and ionic transport induced by ALD SiO_2 coating of nanoporous alumina membranes" *ACS Appl. Mater. Inter*. Vol **5**, 3556-64, (2013).

6. V Romero, V. Vega, **J. García**, V. M. Prida, B Hernando, J Benavente. "Ionic transport across tailored nanoporous anodic alumina membranes" *J. Colloid Interface Sci.* Vol. **376**, 40-6(2012).

7. V. M. Prida, V. Vega, **J. García**, L. González, W. Oliveira, B. Hernando, "Functional Fe–Pd nanomaterials synthesized by template-assisted methods". *J. Magn. Magn. Mater.* Vol. **324**, 3508–3511 (2012).

8. V. Vega, W.O. Rosa, **J. García**, T. Sánchez, J.D. Santos, F. Béron, K.R. Pirota, V.M. Prida, B. Hernando. "Template-assisted CoPd nanowire arrays: magnetic properties and FORC analysis" *J. Nanosci. Nanotechnol*. Vol. **12**, 4736-43 (2012).

9. L. G. Vivas, M. Vázquez, V. Vega, **J. García**, W. O. Rosa, R. P. del Real, V. M. Prida. "Temperature dependent magnetization in Co-base nanowire arrays: Role of crystalline anisotropy". *J. Appl. Phys.* Vol. **111**, 07A325 (2012).

10. **J. García**, V. Vega, L. González, W.O. Rosa, V.M. Prida, B. Hernando, "Comparative Study on the Electrochemical Synthesis and Magnetic Properties of Ferromagnetic Transition Metals-Palladium Nanowire Arrays". *Journal of Spintronics and Magnetic Nanomaterials*, Vol. **1**, 1–5, 2012

11. V. Vega, **J. García**, W. O. Rosa, L. G. Vivas, V. M. Prida, B. Hernando, M. Vázquez. "Magnetic Properties of (Fe, Co)-Pd Nanowire Arrays" *J. Nanosci.Nanotechno.,* Vol. **12**, Number 9, pp. 7501-7504(4), (2012).

Other contributions:

12. L. González-Legarreta, W.O. Rosa, **J. García**, M. Ipatov, M. Nazmunnahar, L. Escoda, J.J. Suñol, V.M. Prida, R.L. Sommer, J. González, M. Leoni, B. "Annealing effect on the crystal structure and Exchange bias in Heusler $Ni_{45.5}Mn_{43.0}In_{11.5}$ alloy ribbons" *J. Alloy Compd.* Vol. **582**, 588 (2013).

13. M. Ipatov, L. González-Legarreta, **J. Garcia**, A. Chizhik, L. Domínguez, V. Zhukova, A. Zhukov, B. Hernando and J. González, "Induced Giant Magnetoimpedance Effect by Current Annealing in Ultra Thin Co-based Amorphous Ribbons", *IEEE Trans. Magn.* Vol. **49,** 1009-1012 (2013).

14. R. Caballero-Flores, T. Sánchez, W.O. Rosa, **J. García**, L. González-Legarreta, D. Serantes, V.M. Prida, Ll. Escoda, J.J. Suñol, B. Hernando. "On tuning the magnetocaloric effect in Ni–Mn–In Heusler alloy ribbons with thermal treatment" *J. Alloys Compd.* Vol. **545,** 216–221, (2012).

15. L. González-Legarreta, T. Sánchez, W.O. Rosa, **J. García**, D. Serantes, R. Caballero-Flores, V.M. Prida, L. Escoda, J.J. Suñol, V. Koledov, B. Hernando. **"**Annealing Influence on the Microstructure and Magnetic Properties of Ni–Mn–In Alloys Ribbons**"** *J Supercond. Nov. Magn.* Vol. **25**, 2431–2436, (2012):

16. L. González, **J. García**, M. Nazmunnahar, W.O. Rosa, Ll. Escoda, J.J. Suñol, V.M. Prida, V.V. Koledov, V.G. Shavrov, B. Hernando. "Annealing and magnetic field influence on the martensitic transition in Ni45.8Mn42.6In11.6 shape memory alloy ribbons" *Trans. Tech. Periodicals* Vol. **190**, 307-310, (2012).

17. W. Rosa, L. Gonzalez, **J. Garcia**, T. Sanchez,M. L. Escoda, J.J. Suñol, J. Santos, V. Prida and B. Hernando. "Tailoring magnetocaloric effect in Ni45.5Mn43In11.5 Metamagnetic shape memory alloy", in *Phy. Res. International*, *Hindawi Publishing Corp*. Vol. 2012, Article ID 794171.

18. V. Vega, L. González, **J. García**, W. O. Rosa, D. Serantes, V. M. Prida, G. Badini, R. Varga, J. J. Suñol, B. Hernando. "Ni59.0Mn23.5In17.5 Heusler alloy as the core of glass-coated microwires: Magnetic properties and magnetocaloric effect", *J.Appl. Phys.*Vol.**112**, 033905 (2012).

19. M.L. Sánchez, V.M. Prida, J.D.Santos, J. Olivera, T.Sánchez, **J.García**, M.J.Pérez, B.Hernando. "Magnetoimpedance in softmagneticamorphous and nanostructuredwires" *Appl. Phys. A* Vol. **104**, 443-445, (2011).

20. T. Sanchez, **J. García**, J.D. Santos, Ll. Escoda, V.M. Prida, M.L. Sánchez, J.J. Suñol, B. Hernando. *"*Off-diagonal magnetoimpedance dependence of magnetostriction and anisotropy in Co-based and Fe-based amorphous ribbons*"* *Acta Physica Polonica A* Vol. **118**, (2010).

21. A.M. Aliev, A.B. Batdalov, I.K. Kamilov, V.V. Koledov, V.G. Shavrov, V.D. Buchelnikov**, J. García**, V.M. Prida, B. Hernando. "Magnetocaloric effect in ribbon samples of Heusler alloys Ni - Mn - M (M = In, Sn)" *Appl. Phys. Lett.* Vol. **97**, 212505-13, (2010).